# Applications of Strongly Coupled Electrostatic NEMS

by

Hamza Mouharrar

A thesis
presented to the University of Waterloo
in fulfillment of the
thesis requirement for the degree of
Master of Applied Science
in
Systems Design Engineering

Waterloo, Ontario, Canada, 2024

© Hamza Mouharrar 2024

## Author's Declaration

This thesis consists of material all of which I authored or co-authored: see Statement of Contributions included in the thesis. This is a true copy of the thesis, including any required final revisions, as accepted by my examiners. I understand that my thesis may be made electronically available to the public

## Statement of Contributions

This thesis contains material from several published and submitted journal and conference papers that I authored. Some of these resulted from collaboration with my colleagues in the same and in other reserach groups at the University of Waterloo.

1. The content of Section 2.2 has been published in:

   **H. Mouharrar**, M. Akbari, K. Musselman, D. Muñoz-Rojas, M. Yavuz and E. Abdel-Rahman, "Noise-Driven MOF-Coated NEMS Sensors," 2023 IEEE 22nd International Conference on Micro and Nanotechnology for Power Generation and Energy Conversion Applications (PowerMEMS), Abu Dhabi, United Arab Emirates, 2023, pp. 187-190, doi: 10.1109/PowerMEMS59329.2023.10417191.

   **Hamza Mouharrar** conducted the experiments including device characterization, gas testing, and data processing and drafted the manuscript. All other authors analyzed and discussed the results and provided intellectual input on manuscript drafts. Eihab Abdel Rahman provided guidance during research and provided feedback on manuscript drafts.

2. The content of Section 2.1 is submitted for publication as:

   Masoud Akbari, **Hamza Mouharrar**, Chiara Crivello, Martial Defoort, Eihab Abdel-Rahman, Skandar Basrour, Kevin P Musselman and David Muñoz-Rojas, "Gas Phase Growth of Metal-Organic Frameworks on Microcantilevers for Highly Sensitive Detection of Volatile Organic Compounds," APL Materials, 2024.

   **Hamza Mouharrar** conducted the experiments including experimental setup, device characterization, gas testing and drafted a part of the manuscript. Eihab Abdel Rahman provided guidance during the research and feedback on the part I contributed in the draft manuscript.

3. The content of Chapter 3 is submitted for publication as:

   **Hamza Mouharrar**, Sasan Rahmanian, Masoud Akbari, Yasser S. Shama and Eihab Abdel Rahman, "NEMS Electromechanical Modal Interaction Induced FC," Nature, microsystems and nanoengineering, 2023.

   **Hamza Mouharrar** conducted the experiments including idea conceptualization, device characterization and testing, and drafted the manuscript. Masoud Akbari fabricated the NEMS device. All other authors analyzed and discussed the results and provided intellectual input on manuscript drafts. Eihab Abdel Rahman provided guidance during research and feedback on manuscript drafts.

4. The content of Chapter 4 is submitted for publication as:

   **Hamza Mouharrar**, Sasan Rahmanian, Rana Abdelrahman. Masoud Akbari, and Eihab Abdel Rahman, "Generation of Mechanical Soliton Frequency Combs in NEMS," ACS Nano Lett, 2024.

   **Hamza Mouharrar** conducted the experiments including the idea conceptualization, device characterization and testing and drafted thw manuscript. Sasan Rahmanian developed the mathematical model. Masoud Akbari fabricated the NEMS device. All other authors analyzed and discussed the results and provided intellectual input on manuscript drafts. Eihab Abdel Rahman provided guidance during research and feedback on manuscript drafts.

## Abstract

This work explores potential applications of electrostatic nanoelectromechanical systems (NEMS) in inertial sensing and Frequency Comb (FC) generation. NEMS inertial sensors exhibit exceptional sensitivity with low power consumption, making them ideal for portable gas sensors. We equip a novel ZnO NEMS with Metal-Organic Frameworks (MOFs) to ensure selectivity to volatile organic compounds (VOCs), resulting in sensor with sensitivity ranging from 0.33 to 0.71 Hz/ppm and limits of detection from 4 to 9 ppb. This high sensitivity is attributed to the high porosity and large surface area of MAF-6. These findings pave the way for the development of MOF-coated NEMS sensors, promising advances in the field of gas sensing.

We also present a novel low-power generation technique for frequency combs (FC) developed using modal interactions in electrostatic NEMS. Experimental results show a broadband FCs spectrum with a coherent phase. The proposed technique is flexible, enabling the generation of multiple frequency combs and fine-tuning of their Free Spectral Range (FSR). Additionally, we show an innovative approach that leverages internal resonances within a NEMS-phononic cavity to generate soliton frequency combs with over 3000 spectral lines, offering a breakthrough for quantum computing and metrology. The soliton generator can seamlessly be integrated into portable devices, aligning with contemporary miniaturized technology.

## Acknowledgments

I would like to thank all the little people who made this thesis possible.

## Dedication

This work is dedicated to my parents and my soulmate.

# Table of Contents

**List of Figures** xi

**List of Tables** xv

**List of Abbreviations** xvi

**1 Introduction** 1

1.1 MEMS & NEMS . . . 1

1.2 Electrostatic MEMS & NEMS . . . 2

1.3 Inertial MEMS & NEMS sensors . . . 3

1.3.1 Metal Oxide (ZnO) material . . . 4

1.4 Frequency comb generators . . . 5

1.5 Research objectives . . . 6

1.6 Thesis outline . . . 6

**2 MEMS and NEMS Gas Sensors** 8

2.1 MOFs on MEMS for Detection of VOCs . . . 8

2.1.1 Microcantilever sensors . . . 9

2.1.2 Deposition of ZnO and synthesis of MOF . . . 9

2.1.3 Experimental setup . . . 10

2.1.4 Results and discussion . . . 12

2.2 Noise-Driven MOF-Coated NEMS Sensors . . . 16
2.2.1 Fabrication of NEMS Sensors . . . 16
2.2.2 Experimental Setup . . . 19
2.2.3 Thermomechanical excitation of the NEMS . . . 19
2.2.4 Characterization . . . 21
2.2.5 Sensor comparison . . . 21
2.3 Electrostatic ZnO NEMS SENSORS . . . 23
2.3.1 Fabrication Process . . . 25
2.3.2 Experimental setup . . . 26
2.3.3 Characterization . . . 27
2.3.4 Humidity sensing . . . 27
2.3.5 VOCs sensing . . . 29
2.4 Conclusions . . . 31

**3 NEMS Electromechanical Modal Interaction Induced FC 32**
3.1 Introduction . . . 32
3.2 Mathematical model . . . 34
3.3 Experimental Setup . . . 39
3.3.1 Electrical measurement . . . 40
3.3.2 Optical measurement . . . 40
3.4 Results and discussion . . . 40
3.4.1 Device and characterization . . . 40
3.4.2 Frequency Combs . . . 43
3.4.3 Stability of the frequency combs . . . 48
3.5 Conclusion . . . 51

**4 Generation of Soliton Frequency Combs in NEMS** **53**

4.1 Introduction . . . . . 54

4.2 Fabrication process for the NEMS . . . . . 56

4.3 Comparison between the DUTs . . . . . 58

4.4 Optical Experimental Setup . . . . . 58

4.5 Results and discussion . . . . . 60

4.6 Conclusion . . . . . 68

**5 Conclusions and Future Work** **69**

5.1 Summary of Contributions . . . . . 69

5.2 Future Work . . . . . 70

**Letter of Copyright Permission** **71**

**References** **72**

# List of Figures


2.1 An SEM image of the OCTOSENSIS cantilever chip. . . . . 9

2.2 Schematic representation of sensitization of cantilevers with Zn(EtIm)2 through MOF-CVD process. (a) A silicon cantilever (b) is coated with 30 nm of ZnO by AP-SALD. (c) Then the cantilever is placed in a bottle with 2-ethylimidazole and $H_2O$. The reaction takes place at 140 °C for 90 min, and (d) ZnO converts to MOF on the surface of the cantilever. . . . . 10

2.3 Schematic representation of the experimental setup. . . . . 11

2.4 SEM images of (a) 10 nm, (b) 20 nm, and (c) 30 nm thick ZnO (left) transformed to MOF (right). The reaction duration and temperature are 90 min and 140 °C. . . . . 12

2.5 SEM images of (a) an uncoated silicon microcantilever, and the edge of the microcantilever (b) coated with 30 nm of ZnO and (c) transformed to MOF. 13

2.6 The frequency response, amplitude and phase, of (a) the ZnO-coated and (b) the MOF-coated cantilevers in the vicinity of the second bending mode. 13

2.7 Frequency shift over time of the ZnO and MOF sensors in response to cyclic injection of (a) acetone, (b) ethanol, (c) isopropanol, and (d) humidity in nitrogen followed by a purge with nitrogen only. . . . . 14

2.8 The frequency shifts of the (a) ZnO and (b) MOF sensors as functions of analyte concentration. . . . . 15

2.9 The resonant frequency measurement while exposed to nitrogen for 1 hour. 16

2.10 (a) SEM Image and (b) schematic of the NEMS sensor. . . . . 17

2.11 Fabrication process of the NEMS . . . . . 18

2.12 Experimental setup. . . . . 19

2.13 FFTs of the NEMS tip velocity under different laser intensity levels. . . . . 20
2.14 The frequency response of the (a) MOF-coated and (b) ZnO-coated MEMS sensors around the 2nd bending mode. . . . . 21
2.15 The frequency-response curves a NEMS sensor under thermal noise excitation in air and vacuum . . . . . 22
2.16 The measured frequency shifts of MEMS sensors coated with ZnO and MOF due to exposure to acetone. . . . . 22
2.17 Response of the noise-driven NEMS sensor to acetone. . . . . 23
2.18 (a) An SEM image and (b) a schematic cross-section of the NEMS the beam and its anchor. . . . . 24
2.19 Fabrication process . . . . . 25
2.20 Experimental setup employed for characterization and testing of the NEMS sensors . . . . . 27
2.21 (a) Schematic of the optical measurement system used to characterize the DUT. (b) FFT of the cantilever tip velocity under thermal noise excitation. 28
2.22 Noise-driven sensing of the NEMS sensor to acetone. . . . . 29
2.23 Noise-driven sensing of NEMS acetone. . . . . 30

3.1 Fabrication process . . . . . 38
3.2 The NEMS cantilever; (a) an SEM image showing the beam and its anchor and (b) a schematic cross-section of the beam. . . . . 39
3.3 The experimental setups used for (b) electrical characterization of the DUT and (b) optical characterization of the DUT as well as observation of the generated frequency combs. . . . . 41
3.4 Schematics of the (a) optical and (b) electrical measurement systems used to characterize the DUT. (c) FFT of the cantilever tip velocity under thermal noise excitation. (d) The measured magnitude and phase of the returned electrical power $S_{11}$ of the DUT. . . . . 42
3.5 Schematic of the electrical measurement system used to characterize the DUT, (b) The measured magnitude and phase of the returned electrical power $S_{11}$ of the DUT for the 1:1 modal interaction case . . . . . 43

3.6 (a) A schematic illustrating the 2:1 electro-mechanical modal interaction employed in this study. (b) The optically measured DUT frequency-response curves below ($V_{\mathrm{DC}} = 0.6V$, $V_{\mathrm{AC}} = 0.7V$) and above ($V_{\mathrm{DC}} = V_{\mathrm{AC}} = 0.9V$) the activation level. . . . . 44

3.7 (a) A schematic of the experimental setup. (b) The measured frequency-response curves, for four levels of excitation. The measured FFT of the cantilever's tip velocity in air (c) below, (d) just above, and beyond activation level. (f) The complex FFT of the cantilever's tip velocity in air. . . . 45

3.8 The measured FFT of the cantilever's tip velocity in air under an excitation of $\mathrm{V_{DC}}$=1 V, $\mathrm{V_{AC}}$=2.3 V, and $f = 206\,\mathrm{kHz}$ . . . . . 48

3.9 (a) The measured frequency-response curves, for three excitation levels as the frequency is swept from 90 kHz to 110 kHz. (b) The measured FFT of the cantilever's tip velocity in air demonstrating the frequency comb generated under an excitation of $\mathrm{V_{DC}}$=1 V, $\mathrm{V_{AC}}$=2.3 V, and $f = 101.95\,\mathrm{kHz}$ . . . . . 48

3.10 The measured time-histories of the beam tip displacement and velocity under electrical excitation with the waveform ($V_{DC} = 1\,\mathrm{V}$, $V_{AC} = 2.3\,\mathrm{V}$), and $f = 202.2\,\mathrm{kHz}$ and (e) the corresponding phase portrait. . . . . 50

3.11 The frequency-domain, the time-domain, and the phase portrait of the analog signal presented in Eq. (S11) are demonstrated, respectively, for $\phi_i = 0$ in (a), (c), (e) and (g), and for $\phi_i \neq 0$ ($i = 1, 2, ..., 150$) in (b), (d), (f) and (h). 51

4.1 Graphical abstract . . . . . 54

4.2 Fabrication process . . . . . 57

4.3 The NEMS bracket-supported cantilever; (a) an SEM image showing the beam and its anchor and (b) a schematic cross-section of the beam. . . . . 58

4.4 The NEMS simple-supported cantilever; (a) an SEM image showing the beam and its anchor and (b) a schematic cross-section of the beam. . . . . 58

4.5 The experimental setups used for optical characterization of the DUT as well as observation of the generated frequency combs. . . . . 59

4.6 (a) Schematic of the optical measurement system used to characterize the DUT. (b) FFT of the cantilever tip velocity under thermal noise excitation. 61

4.7 (a) Schematic of the used experimental setup and FFT response for difference waveform voltages (b) $V_{\mathrm{DC}} = 5V$, $V_{\mathrm{AC}} = 7V$ (c) $V_{\mathrm{DC}} = V_{\mathrm{AC}} = 8V$ (d) $V_{\mathrm{DC}} = 10V$ and $V_{\mathrm{AC}} = 15V$ and (e) $V_{\mathrm{DC}} = 15V$ and $V_{\mathrm{AC}} = 30V$ . . . . . 63

4.8 Complex FFT for the DUT velocity response for state II soliton (a), (c) and (e) and Soliton state I (b), (d) and (f) . . . . . 65

4.9 FFT showing multi soliton response for states I and II from (a) and (c) Experimental results and (b) and (d)Numerical simulation . . . . . 66

4.10 Time domain response for different waveforms and same excitation frequency. 67

4.11 Time domain response for same voltage waveforms and different excitation frequency (a,b,c and d) Experimental results and (e) numerical simulation. 68

# List of Tables


2.1 Vapor pressures and saturated concentrations of tested analytes . . . . . 12
2.2 Responsivity ($R$) and LOD for the MOF and ZnO sensors. . . . . 17
2.3 Summary of the cantilever's dimensions. . . . . 24
2.4 NEMS sensor responsivity and LOD to VOCs . . . . . 31

3.1 Comparison of FCs in NEMS/MEMS . . . . . 47

4.1 Comparison of pull in voltage between the two devices under test . . . . . 59
4.2 Comparison of FCs in NEMS/MEMS . . . . . 66

## List of Abbreviations

| | |
|---|---|
| **AFM** | atomic force microscopy |
| **ALD** | atomic layer deposition |
| **AP-SALD** | atmospheric pressure spatial atomic layer deposition |
| **CVD** | chemical vapor deposition |
| **FFT** | fast Fourier transform |
| **ZnO** | zinc oxide |
| **Si** | silicon |
| **IoT** | internet of things |
| **LOD** | limit of detection |
| **MEMS** | micro-electromechanical systems |
| **NEMS** | nano-electromechanical systems |
| **MFC** | mass flow controller |
| **MOF** | metal-organic framework |
| **MOF-CVD** | chemical vapor deposition of metal-organic framework |
| **ppb** | parts per billion |
| **ppm** | parts per million |
| **VOC** | volatile organic compound |
| **ZIF** | zeolite imidazole frameworks |
| **SOI** | silicon on insulator |
| **OFDM** | orthogonal frequency division multiplexing |
| **WDM** | wavelength division multiplexing |

| | |
|---|---|
| **RF** | radio frequency |
| **SEM** | scanning electron microscope |
| **FWM** | four wave mixing |
| **GVD** | group velocity dispersion |
| **MLLs** | model locked lasers |
| **PLL** | phase locked loop |
| **SNR** | signal-to-noise ratio |

# Chapter 1

# Introduction

This chapter addresses MEMS, NEMS, and their applications. The first section provides background on MEMS & NEMS technology. The next three section describe important applications of MEMS & NEMS relevant to this work. The last two sections conclude with the research objectives and thesis outline.

## 1.1 MEMS & NEMS

In essence, MEMS & NEMS are micro & nano-scale devices integrating electrical, mechanical, and system functionalities. The terms "micro / nano" emphasize that the respective class of devices possess at least one dimension within the micrometer / nanometer range. "Electro" underscores their reliance on electrical actuation, detection, or both. The descriptor "Mechanical" highlights the inherent mechanical motion of these devices, distinguishing them from their purely electronic counterparts. Finally, the term "systems" underscores their role as integrated entities, operating harmoniously as complete a system rather than disparate components [1].

Various microfabrication techniques cater to the production of MEMS devices, primarly surface micromachining, bulk micromachining, and lithography [1]. Widely available commercial fabrication processes include SOIMUMPs [2] and PolyMUMPs [3], among others.

MEMS & NEMS devices predominantly function as sensors or actuators. Sensors detect a physical stimulus, whereas actuators control or manipulate micro / nano-objects. Functioning as transducers, these devices facilitate the transfer of energy between at least two physical domains [1]. M/NEMS sensors includes pressure sensors [4], temperature

sensors [5], gas sensors [6, 7], humidity sensors [8], force sensors [9], and inertia sensors [10, 11]. Common applications of MEMS actuators encompass scanning micro-mirrors [12], adaptive micro-mirrors, as well as RF switches [13, 14], and micro-tweezers [15].

M/NEMS devices are superior to alternative technologies in the market due to their diminutive size, lightweight, high precision, portability, low power consumption, cost effectiveness, and, significantly, their capacity for high-functionality in real-time applications [16]. These attributes collectively position M/NEMS devices as integral components in the contemporary technological landscape.

## 1.2 Electrostatic MEMS & NEMS

Given their role as transducers, MEMS & NEMS devices employ various transduction methods to convert energy between the electrical and mechanical domains. Sensing or detection methods, such as electrostatic [17], piezoresistive [18], and piezoelectric [19], facilitate the conversion of physical changes, like humidity or pressure, into electric signals for measurement purposes. Conversely, actuation methods convert input energy into microstructure motion, utilizing electrostatic [20], piezoelectric [21], electromagnetic [22], and electrothermal [23] methods.

Among the transduction methods, electrostatic transduction stands out as the most widely employed for both actuation and detection in MEMS & NEMS devices. Its prevalence is attributed to its simplicity, high efficiency, low power consumption, and rapid response times. Devices utilizing electrostatic transduction are commonly referred to as electrostatic M/NEMS [1].

In electrostatic MEMS & NEMS, the fundamental principle involves two electrodes separated by a capacitive gap and connected to an electric potential difference. This potential difference generates an electric field, leading to an attractive electrostatic force between the electrodes. Consequently, the electrodes are drawn towards each other, causing a displacement change in the movable electrode [1].

Electrostatic actuators control the potential difference between its electrodes to generate a force or displacement. On the other hand, in electrostatic sensing, changes in the surrounding environment, such as humidity or temperature, alter the total capacitance between sensor electrodes. An electronic circuit can then correlate these capacitance changes to the measured physical quantities.

In order to fabricate competitive MEMS/NEMS devices, it is imperative to be able to model and simulate them accurately. An important challenge in this regard is the fact

that nonlinearities in MEMS devices can be significant, even dominant, unlike macro-scale systems. Common sources of nonlinearity in electrostatic M/NEMS include capillary forces, displacement-dependent electrostatic force, van der Waals forces, system geometry, system inertia, and squeeze film damping. These nonlinearities can lead to various phenomena, including chaos, and static and dynamic bifurcations, which emphasize the need for careful analysis of electrostatic M/NEMS.

## 1.3 Inertial MEMS & NEMS sensors

Sensors are indispensable components in contemporary technology, especially with the burgeoning IoT landscape. Their primary function lies in detecting and quantifying changes in physical or environmental parameters, transforming these observations into actionable data. The global sensor market, projected to grow from $156.6 billion in 2021 to $249.6 billion by 2026, underscores their pervasive influence across various industries [24, 25].

Within the diverse array of sensing technologies, gas sensors have emerged as vital tools, capable of detecting and monitoring the presence and concentration of gases in the environment. This capability addresses pressing concerns related to air quality, workplace safety, and agricultural optimization. In urban settings, gas sensors play a pivotal role in monitoring and mitigating air pollution levels, identifying harmful emissions from industries, vehicles, and other pollution sources. Furthermore, gas sensors are instrumental in ensuring workplace safety, particularly in industries where hazardous gases or VOCs pose potential risks. Additionally, gas sensors find application in the agricultural sector, where they aid in monitoring and controlling greenhouse gases to optimize crop growth and resource consumption [26, 27].

Inertial gas sensors traditionally employ resonant micro-mass sensors as foundational platforms in various applications, spanning biological, chemical, and automotive domains [28, 29, 30]. These sensors leverage a highly selective coating to capture and sorb target gas particles from the environment. The resulting change in total mass induces a shift in the sensor's resonant frequency [31, 32]. Their sensitivity is superior to that of static sensors. Detection methods encompass optical [30, 32, 33, 34, 35], capacitive [36, 37, 38], and piezoresistive [39, 40, 41] approaches.

While optical gas sensing offers has the advantage of superior precision, MEMS & NEMS sensors have the advantages of compact size, lightweight, portability, low power consumption, and cost-effectiveness [16]. At the turn of the century, Datskos et al. [32], Lang et al. [42], and others demonstrated that microcantilevers equipped with detector

polymers can serve as sensitive gas sensor. However, ensuring their long-term reliability and selectivity remain challenging.

While Lang et al. [42] found that thicker polymer layers were more sensitive, Sampath et al.[43] highlighted the trade-off between increased sensitivity and plasticization-induced frequency drop with thicker layers. Dufour et al. [44] suggested the use of uncoated MEMS sensors for gas and liquid detection based on density variations but acknowledged their intrinsic lack of selectivity.

The sensitivity of inertial gas sensors can be enhanced by exciting higher structural modes, thereby reducing their effective mass. Dohn et al. [33] showed a 300-fold sensitivity improvement by operating a cantilever MEMS mass sensor at its fourth bending resonant frequency. Xie et al. [35] achieved enhanced mass sensitivity by utilizing a torsional mode compared to the first two flexural modes. Others have also reported similar results [34, 35, 45, 46, 47, 48, 49].

Younis and Alsaleem [50] proposed mass sensing techniques employing nonlinearity in electrostatic MEMS, reporting increased detection signal near subharmonic resonances. Bouchaala et al. [51] employed a sudden amplitude change caused by a cyclic-fold bifurcation in an electrostatic microbeam to detect water vapor. Alghamdi et al. [52] developed a binary inertial gas sensor using a PolyMUMPs fabricated MEMS resonators, employing the dynamic pull-in phenomenon for ethanol vapor detection. They results indicated a detection limit of 100 ppb.

### 1.3.1 Metal Oxide (ZnO) material

Metal oxides frequently serve as a sensing layer in chemiresistive gas sensors, where the sensing mechanism relies on detecting alterations in the electrical conductivity or resistance of the material when exposed to a target gas. The widely accepted gas sensing mechanism involves adsorption of oxygen molecules on the metal oxide's surface [53, 54, 55, 56].

Chemisorption-induced mass changes contribute to gravimetric sensing mechanisms. If chemisorption adds mass to the sensor, it induces a negative shift in resonance frequency. Conversely, the release of surface species leads to mass reduction and a positive shift in resonance frequency. Physisorption, a process where gas molecules are attracted to the material's surface through intermolecular forces, also contributes to gravimetric sensing mechanism by causing mass changes [57, 58].

While metal oxide receptors in chemiresistive gas sensors have been extensively studied, their application as sensing materials in gravimetric and inertial detection is relatively

less explored. This may be attributed to the simpler fabrication process of chemiresistive sensors and the well-established understanding of sensing mechanisms in that case. Nevertheless, recent advances highlight the utilization of metal oxides as receptor layers in gravimetric sensors [57, 58].

Kilinc et al. [59] utilized ZnO nanorods and nanotubes on nickel cantilevers to detect various volatile organic compounds (VOCs), showing a notable response to ammonia. Xu et al. [60] fabricated ZnO nanorods functionalized with a chitosan coating on Si cantilevers. Their sensors exhibited enhanced sensitivity to changes in relative humidity. Other researchers [61] created ZnO-based freestanding resonant cantilever sensors with ultrahigh sensitivity to humidity.

The literature suggests that metal oxides hold significant potential as sensing layers in gravimetric and inertial sensors. Various strategies, such as nanostructuring, combining with other materials, and doping, can further enhance their sensing properties. Additionally, sensor miniaturization promises increased sensitivity.

## 1.4 Frequency comb generators

Silicon photonics is an emerging micro-scale technology that has garnered significant attention. It allows the implementation of photonic systems within a small footprint. Those systems can process information in optical form by generating, modulating, transmitting, switching, amplifying, and detecting light. Silicon proves a practical choice due to its intrinsic bandgap of 1.1 eV, rendering it transparent within the optical communication transmission wavelengths (1270 nm to 1625 nm) [62, 63].

Over the last 25 years, OFCs have made a resounding impact, shaping fields from metrology to astronomy [64, 65, 66, 67, 68, 69, 70]. Their frequency coherence established them as essential metrology tools in labs worldwide [67, 71, 72]. Recent strides in nonlinear optical resonators, especially ring resonator systems, have harnessed the power of optical solitons, by balancing nonlinearity and dispersion to enhance the stability of the spectral lines and FCs. This advancement has far-reaching implications across disciplines, benefiting applications in timing, sensing, resonance stabilization, spectroscopy, and quantum information processing. OFCs realized via silicon photonics within micro-scale nonlinear optical resonators [62] show promise in reducing both the footprint and power consumption compared to traditional FC generators.

The combination of high structural quality and reduced effective mass empowers MEMS & NEMS resonators to operate at high resonant frequencies and achieve high quality (Q)

factors at ultra-low power consumption. Electrostatic MEMS & NEMS hold particular promise as FC generators due to their strong nonlinearity. Diverse methods have been employed to generate mechanical FCs in MEMS & NEMS, including parametric excitation, modal interactions within one or more structures, and external excitation of self-excited systems.

## 1.5 Research objectives

This research centers on the study and development of an electrostatic NEMS resonators for gas sensing and frequency comb generation, aiming to surpass the performance of existing technologies. It encompasses the device design, characterization, and the exploration of innovative techniques never explored before to address those purposes. The specific objectives of this research are summarized as follows:

- Investigate and demonstrate the efficacy of MEMS sensors coated with MOF, as well as noise-driven nd electrostatic NEMS sensors coated with MOF-ZnO, for the detection of VOCs and humidity.
- Introduce an efficient and cost-effective approach for FC generation by leveraging electro-mechanical modal interaction within an NEMS resonator. This method aims to achieve enhanced spacing resolution compared to existing complex techniques.
- Present a novel methodology for generating wide band mechanical soliton FCs by leveraging internal resonance within NEMS resonators to facilitate energy transfer between low and high frequency modes.

## 1.6 Thesis outline

This thesis comprises 5 chapters, organized as follows:

- Chapter 1: Provides a background on MEMS & NEMS, their applications, and the thesis organization.
- Chapter 2: Focuses on the development, characterization, and testing of MOF equipped MEMS gas sensors and MOF-ZnO NEMS gas sensors.

- Chapter 3: Introduces a novel approach for FC generation through electro-mechanical modal interaction within an electrostatic NEMS.
- Chapter 4: Presents another novel approach for mechanical soliton FC generation through combination internal resonances within an electrostatic NEMS platform.
- Chapter 5: Summarizes the findings of this work, discusses the limitations of the proposed techniques, and outlines the next steps to further develop them.

# Chapter 2

# MEMS and NEMS Gas Sensors

This chapter is comprised of three distinct sections. The initial part delves into the fabrication, characterization and performance evaluation of the MOF material. The subsequent sections elucidate the performance metrics of the ZnO-MOFs NEMS sensors, offering a comprehensive exploration of their capabilities.

## 2.1 MOFs on MEMS for Detection of VOCs

VOCs are organic pollutants hazardous to the environment and human health. Monitoring and reducing VOC levels can improve indoor air quality and prevent negative health effects. Therefore, developing VOC sensors with high sensitivity, selectivity, low power consumption, and low-cost is crucial.

MOFs are hybrid nanoporous crystalline materials. ZIF are MOFs where metals with tetrahedral coordination (i.e., Zn, Co, Fe, Cu) occupy the central node and the ligands are imidazolate-based organic molecules. ZIFs are promising for gas-sensing applications as they have a large surface area, high porosity, adjustable pore size, and excellent selective adsorption capability for various gasses [73]. However, since ZIFs generally exhibit poor electrical conductivity, their application as the gas-sensing layer in conventional chemiresistive sensors is challenging. Therefore, these materials should be combined with conductive materials to form heterostructures and improve sensing performance [74, 75]. However, this process can be complicated and challenging [76].

We employed the MOF-CVD technique to sensitize a silicon cantilever with a compact and uniform zinc 2-ethylimidazolate (Zn(EtIm)2) thin film for VOC sensing. To assess its

performance, we conducted a comparative analysis with a cantilever sensitized with a ZnO thin film, considering widespread use of ZnO as a gas sensing material [77].

### 2.1.1 Microcantilever sensors

OCTOSENSIS dynamic-mode silicon cantilevers containing eight cantilevers per chip, Figure 2.1(a), were purchased from Micromotive MIKROTECHNIK[78]. The cantilever lengtg, width, and thickness are L = 500 ± 4 µm, W = 90 ± 2 µm, and H = 5 ± 0.3 µm, respectively. The natural frequencies of the cantilever's first three bending modes are $f_1 = 24.34\,\text{kHz}$, $f_2 = 162.04\,\text{kHz}$, and $f_1 = 449.66\,\text{kHz}$. [78].

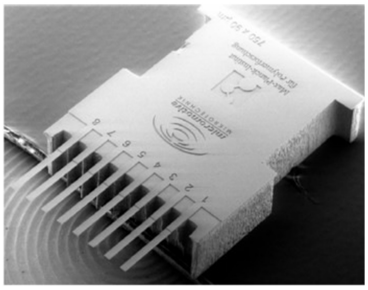


Figure 2.1: An SEM image of the OCTOSENSIS cantilever chip.

### 2.1.2 Deposition of ZnO and synthesis of MOF

ZnO was deposited using a custom-made AP-SALD system equipped with a close-proximity gas injection head. Diethyl zinc and deionized water were used as the metal and oxygen precursors, respectively, and nitrogen as the carrier gas. The substrate temperature was maintained at 200 °C during film deposition [79, 80].

Zn(EtIm)2 was synthesized through a MOF-CVD approach. The ZnO-coated substrates and cantilevers were positioned in a Pyrex bottle as the reaction system, Figure 2.2. The organic linker was placed at the bottom of the bottle. A small vessel containing 10 ml of water as the template was placed inside the bottle, separated from the linker. The reaction system was closed and placed inside an oven at 140 °C for 90 min to convert ZnO to MOF.

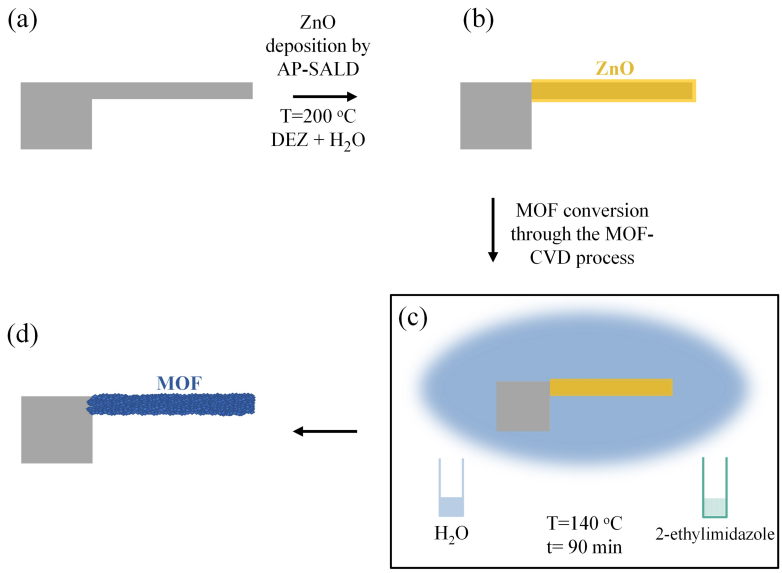



Figure 2.2: Schematic representation of sensitization of cantilevers with Zn(EtIm)2 through MOF-CVD process. (a) A silicon cantilever (b) is coated with 30 nm of ZnO by AP-SALD. (c) Then the cantilever is placed in a bottle with 2-ethylimidazole and $H_2O$. The reaction takes place at 140 °C for 90 min, and (d) ZnO converts to MOF on the surface of the cantilever.

### 2.1.3 Experimental setup

The chip was clamped to a piezoelectric actuator (Bruker DCHNM probe holder) excited by AC voltage. The vibrations of the cantilever were measured by optical vibrometry (Polytec OFV 3001), whereby a laser beam was focused on the cantilever tip through a microscope with a 20x objective lens. The drive voltage and detection signal, output voltage of the photodetector, were supplied and measured by a lock-in amplifier (Zurich Instruments HF2LI). The phase between the input and output signals was locked at the resonance of the second out-of-plane flexural mode and its frequency shift was monitored in real-time through the built-in PLL circuit of the lock-in amplifier. A schematic representation of the experimental setup is shown in Figure 2.3.

The chip was placed in a custom-made test chamber equipped with an optical window, a gas inlet and a gas outlet. The analyte vapor was generated by passing a carrier gas (nitrogen) through a bubbler containing a sample of the analyte in liquid form to evaporate it. A second MFC was used to introduce a dilution flow of the carrier gas into the test

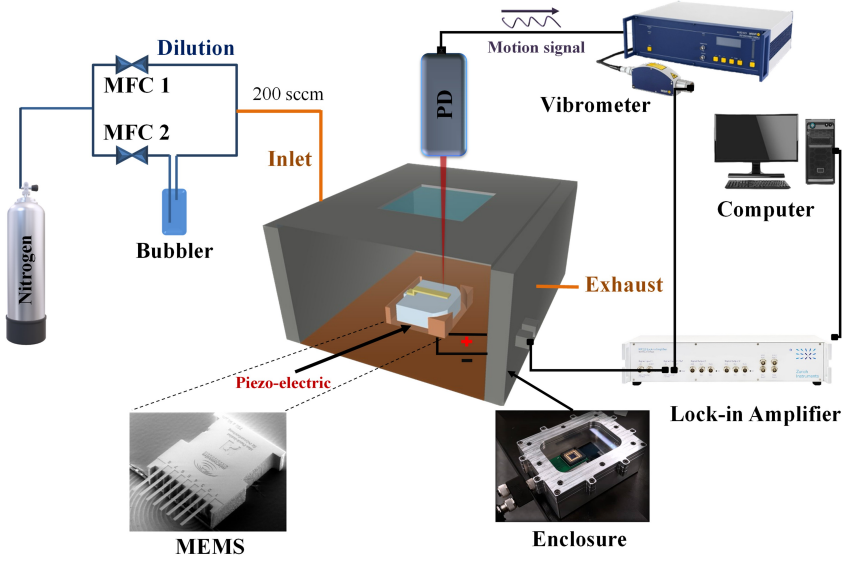



Figure 2.3: Schematic representation of the experimental setup.

chamber. The concentration of the analyte in the chamber was controlled by adjusting the ratio between the bubbler (MFC2) and a dilution gas (MFC1) flow rates. The total flow rate into the test chamber was maintained at a constant value of 200 sccm throughout the experiment.

As a result, the analyte concentration in the chamber was a fraction of the saturated concentration contained in the flow of MFC2. Assuming that flow to saturate with the analyte vapor pressure, the saturated concentration can be calculated as:

$$\text{Saturated concentration (ppm)} = \frac{\text{component vapor pressure [mmHg]}}{\text{atmospheric pressure [mmHg]}} \times 10^6$$

Component vapor pressures and saturated concentrations of the test analytes under study are listed in Table 2.1. The analyte concentration was estimated by multiplying the saturated concentration by the ratio of bubbler flow to total flow. For instance, at a total flow rate of 20 sccm, an ethanol flow rate of 0.2 sccm and a nitrogen flow rate of 199.8sccm, the ethanol concentration in ppm would be $\frac{0.2}{200} \times 70825 \approx 70$ppm.

Table 2.1: Vapor pressures and saturated concentrations of tested analytes

| Analyte | Vapor Pressure @ 23.5° C (mmHg) | Saturation Concentr. (ppm) |
|---|---|---|
| Water | 21.6472 | 28483 |
| Ethanol | 53.8272 | 70825 |
| Acetone | 215.06 | 282973 |
| Isopropanol | 39.75 | 52302 |

### 2.1.4 Results and discussion

To identify the thinnest ZnO layer that could lead to uniform MOF formation, different thicknesses of ZnO were deposited on silicon substrates and converted to MOF. Figure 2.5 presents the surface morphology of ZnO sacrificial layers ranging from 10 to 30 nm and their corresponding MOF structures. The deposition of 10 nm of ZnO leads to scattered MOF crystals on the substrate, while thicker oxide films provide more Zn species for the chemical reaction, causing the crystals to combine and form a uniform and compact MOF film. The results indicate that a 30 nm ZnO layer is suitable for cantilever functionalization.

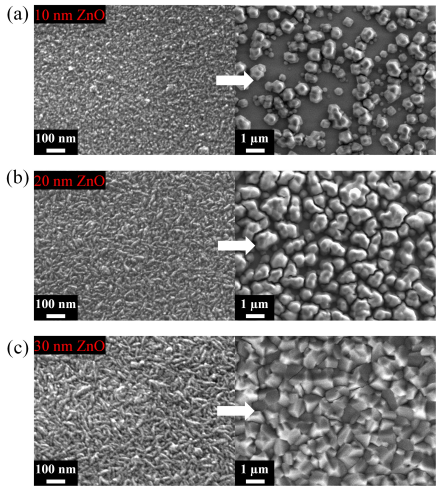



Figure 2.4: SEM images of (a) 10 nm, (b) 20 nm, and (c) 30 nm thick ZnO (left) transformed to MOF (right). The reaction duration and temperature are 90 min and 140 °C.

The GI-XRD pattern of the MOF grown from a 30 nm thick ZnO coating on a silicon

substrate characterized the MOF as MAF-6, which is composed of tetrahedrally coordinated zinc cation centers, bridged by 2-ethylimidazole linker [81, 82].

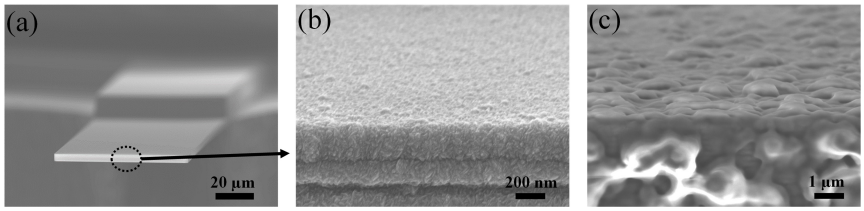



Figure 2.5: SEM images of (a) an uncoated silicon microcantilever, and the edge of the microcantilever (b) coated with 30 nm of ZnO and (c) transformed to MOF.

The fabrication process flow is illustrated in Figure 2.5; silicon cantilevers, Figure 2.5(a), are coated with 30 nm of ZnO, Figure 2.5(b), which is subsequently converted to MOF, Figure 2.5(c). AP-SALD exposes all surfaces of the cantilevers to precursors, resulting in a conformal growth of ZnO. Likewise, the gas-phase nature of the MOF-CVD process coats all surfaces of the cantilever with MOF which provides more surface area for gas adsorption.

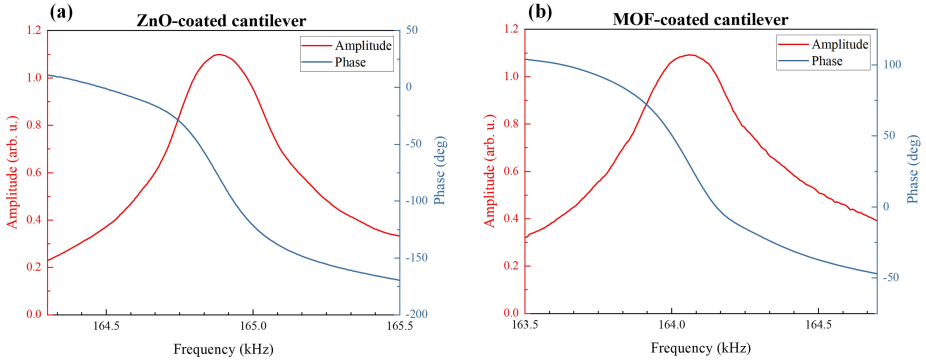



Figure 2.6: The frequency response, amplitude and phase, of (a) the ZnO-coated and (b) the MOF-coated cantilevers in the vicinity of the second bending mode.

We compared the performance of the ZnO-coated microcantilevers, fabricated in step 2, and the MOF-coated microcantilevers, fabricated using the full process described above, as gas sensors. In order to achieve higher mass sensitivity, the sensors were set to exploit the frequency shift of the second bending mode [33, 83]. We identified the resonant frequency of that mode by sweeping the excitation frequency up in the vicinity of the bare silicon microcantilever's reported natural frequency while holding the amplitude constant at 0.5

V. The amplitude and phase of the measured photodetector voltage, proportional to the cantilever tip velocity, are depicted in Figure 2.6. They show that the resonant frequencies in air were $f_\circ = 164.89$ kHz for the ZnO sensor and $f_\circ = 164.06$ kHz for the MOF sensor.

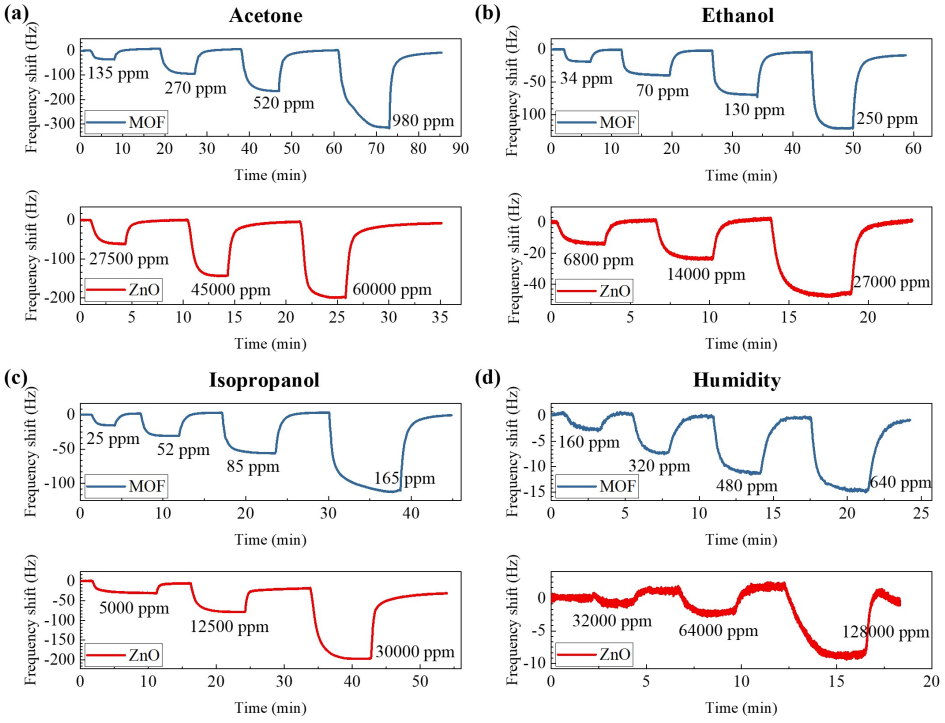



Figure 2.7: Frequency shift over time of the ZnO and MOF sensors in response to cyclic injection of (a) acetone, (b) ethanol, (c) isopropanol, and (d) humidity in nitrogen followed by a purge with nitrogen only.

The PLL of the lock-in amplifier was used to lock the sensor response at the resonant phase corresponding to $f_\circ$. The lock-in amplifier was then used to measure the frequency shift of that phase angle for both sensors as they were exposed to various gaseous environments. Figure 2.7 displays the real-time frequency shift when the sensors were exposed to acetone, ethanol, isopropanol, and humidity. In each case, the frequency shifted to lower values as the sensor came into equilibrium with the gases environment. The equilibrium frequency shift was measured once that shift was observed to settle down (over time) with respect to the baseline (reference) resonant frequency measured after the test chamber was purged with nitrogen and the sensor allowed to come to equilibrium with the nitrogen environment. Each test cycle was composed of an exposure phase to a given analyte at a

known concentration in nitorgen followed by a purge phase with nitrogen only. All measurements were repeated across three sensors to validate the observed trends and ensure reproducibility.

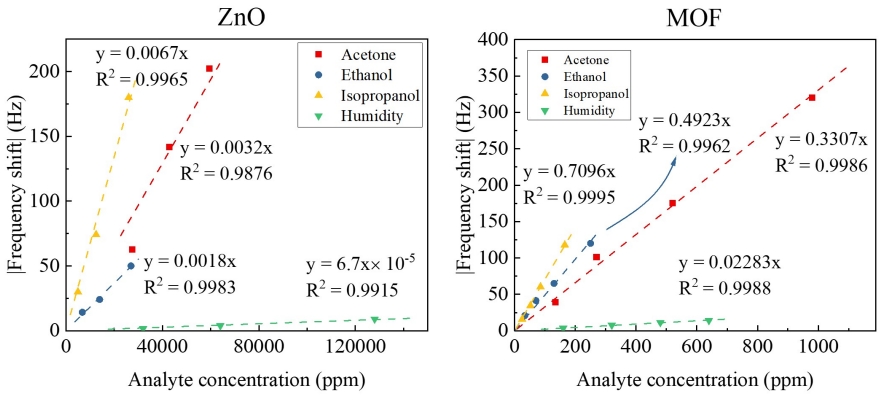



Figure 2.8: The frequency shifts of the (a) ZnO and (b) MOF sensors as functions of analyte concentration.

Figure 2.8 plots the measured frequency shift versus analyte concentration of the ZnO and MOF sensors. The responsivity of the sensors to each analyte were determined by evaluating the slope of a least-square fit line through each set of measurements as listed in Table 2.2. The MOF sensors displayed high sensitivity to VOCs with responsivities in the range of 0.33-0.71 Hz/ppm and low sensitivity to humidity with a responsivity of 0.02 Hz/ppm. But they exhibited no clear selectivity among the VOCs. Comparing these values with those for the ZnO sensors highlights a remarkable improvement in sensitivity (by 80 to 250 times) due to the transformation of ZnO to MAF-6.

The LOD, the lowest detectable concentration of an analyte, is a function of the sensor's responsivity to background noise. For a frequency shift sensor, this represents the frequency instability under background noise $f_{\text{noise}}$. We evaluated it by measuring shifts in the locked resonant frequency while the sensor was excited with the same signal (0.5V) and exposed to nitrogen for one hour, Figure 2.9. Based on this measurement, was estimated the frequency instability as $f_{\text{noise}} = 0.01\,\text{Hz}$.

Within this study, we define the LOD as

$$\text{LOD} = \frac{3f_{\text{noise}}}{R}$$

Using this formula, we calculated the LOD of the sensors as listed in Table 2.2. The

LODs of the MOF sensors to VOCs were found to be in the ppb range, which is three orders-of-magnitude better than those of the ZnO sensors.

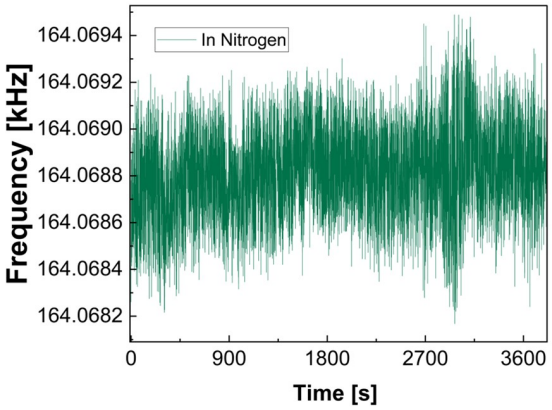



Figure 2.9: The resonant frequency measurement while exposed to nitrogen for 1 hour.

## 2.2 Noise-Driven MOF-Coated NEMS Sensors

The quest for minimal power consumption is a common aspiration for gas sensors. However, most inertial sensors need some form of input power for piezoelectric or electrostatic actuation. Noise-driven NEMS sensors appear to be a promising solution, offering an exceptional combination of sensitivity and low power consumption [84, 85, 86].

In this section, a noise-driven NEMS sensor was fabricated from a 200 nm ZnO thin film, serving both as the structural layer and gas-sensing receptor. The NEMS sensor will be compared to the MEMS ZnO and MEMS MOFs sensors, developed in the previous section, as detectors of acetone, a representative VOC.

### 2.2.1 Fabrication of NEMS Sensors

The NEMS sensors are made of a 200 nm-thick doped ZnO layer that serves as the structural and functional material. Capacitive readout is provided by a 50 nm-thick Aluminum (Al) layer deposited on top of the ZnO layer, 2.10(b), and coupled to a substrate Al electrode. Figure 2.10(a) shows a SEM image of a NEMS measuring 50 µm long and 10 µm wide.

Table 2.2: Responsivity ($R$) and LOD for the MOF and ZnO sensors.

| Analyte \ Sensor | MOF | | ZnO | |
|---|---|---|---|---|
| | $R$ (Hz/ppm) | LOD (ppm) | $R$ (Hz/ppm) | LOD (ppm) |
| Acetone (4.6 Å, 58.08 g/mol) | 0.33 | 0.0091 | $3.2 \times 10^{-3}$ | 1.3 |
| Ethanol (4.5 Å, 46.07 g/mol) | 0.49 | 0.0051 | $1.8 \times 10^{-3}$ | 1.6 |
| Isopropanol (4.7 Å, 60.1 g/mol) | 0.71 | 0.0042 | $6.7 \times 10^{-3}$ | 0.5 |
| Humidity (2.75 Å, 18.01 g/mol) | 0.02 | 0.15 | $6.7 \times 10^{-5}$ | - |

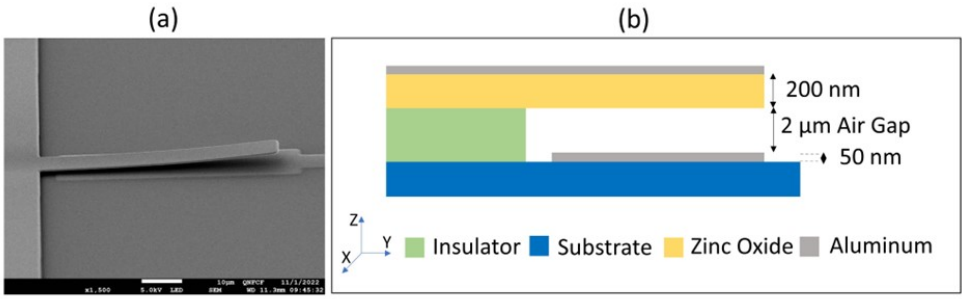



Figure 2.10: (a) SEM Image and (b) schematic of the NEMS sensor.

The steps of the fabrication process are shown schematically in Figure 2.11. The process uses a 3-inch silicon wafer featuring a 300 nm thick thermal oxide layer. The wafer undergoes an initial cleaning with acetone and isopropanol. Employing a standard lift-off technique, the bottom electrode and bonding pads are created, Figure 2.11(a). This process entails application of negative-tone photoresist UV lithography, and deposition of a 50 nm-thick aluminum (Al) layer through sputter deposition. The wafer is then spin-coated with a 1 µm -thick sacrificial positive-tone photoresist layer and patterned using UV lithography, Figure 2.11(b).

A specialized AP-SALD system is employed to deposit the ZnO layer. Diethylzinc and water are used as zinc and oxygen precursors, delivered by nitrogen as a carrier gas, Figure 2.11(c). The silicon wafer, heated to 200°C, oscillates in-plane to expose its full surface to

the precursor flow channels, allowing for the deposition of a 200 nm thick ZnO film in 180 oscillations. The resulting film conforms to the substrate surface, including the sides of the sacrificial photoresist layer, ensuring secure attachment of the structural layer to the anchors.

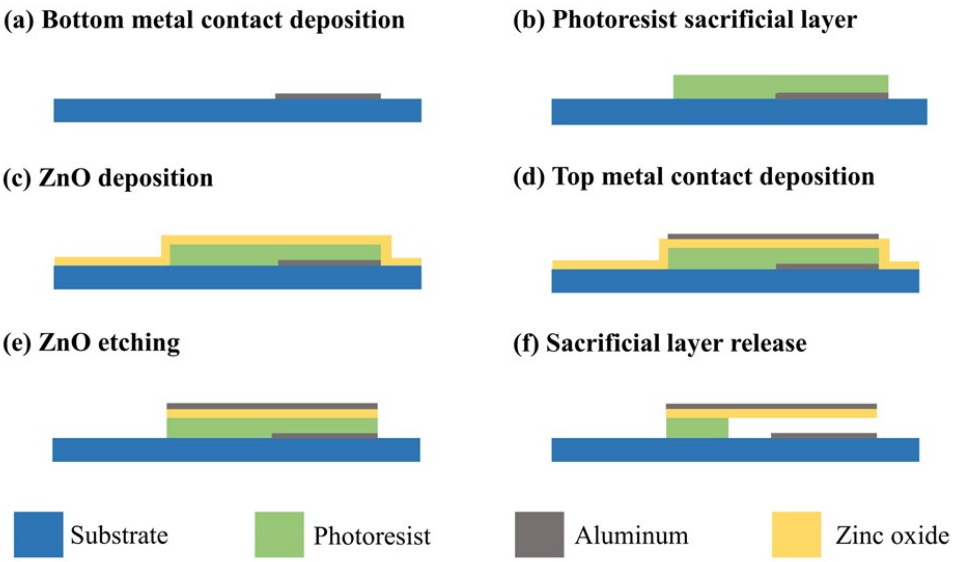



Figure 2.11: Fabrication process of the NEMS

A second lift-off process is employed, Figure 2.11(d), to deposit and pattern 50 nm-thick Al layer, deposited via sputter deposition to serve as the top metal electrode. The metal electrode also enables optical readouts via a laser Doppler vibrometer. Further, it functions as an etch mask for reactive ion etching (RIE) of the ZnO layer, Figure 2.11(e), to define the cantilever. It also reveals the sacrificial layer underneath it for subsequent release, Figure 2.11(f). Anisotropic oxygen plasma ashing is employed to remove a part of the sacrificial photoresist layer. The process continues until the 50 $\mu$m photoresist under the beam is completely removed, as verified visually through SEM. The fabrication process results in the creation of a nanocantilever beam approximately 250 nm thick, 50 µm long, and 10 µm wide. Despite its substantial aspect ratio, the cantilever remains free-standing, Figure 2.10(a), a feat attributed to the conformal ZnO layer and covalent bonds generated during the AP-SALD process, ensuring robust adhesion to the substrate.

### 2.2.2 Experimental Setup

To test the NEMS sensor, we employed a high-frequency laser Doppler vibrometer (Polytech UHF-120) to measure the velocity of the cantilever tip oscillations. The sensor was wire-bonded to a chip carrier and placed in the test chamber described above. In this setup, the cantilever was thermally actuated using the vibrometer's laser. The laser beam was focused onto the corner of the cantilever tip through a 50x objective lens to track oscillations of the first torsional mode before and after exposure to acetone, Figure 2.12. The measured velocity-time signal was post processed to obtain its FFT and derive the frequency response of the cantilever motions.

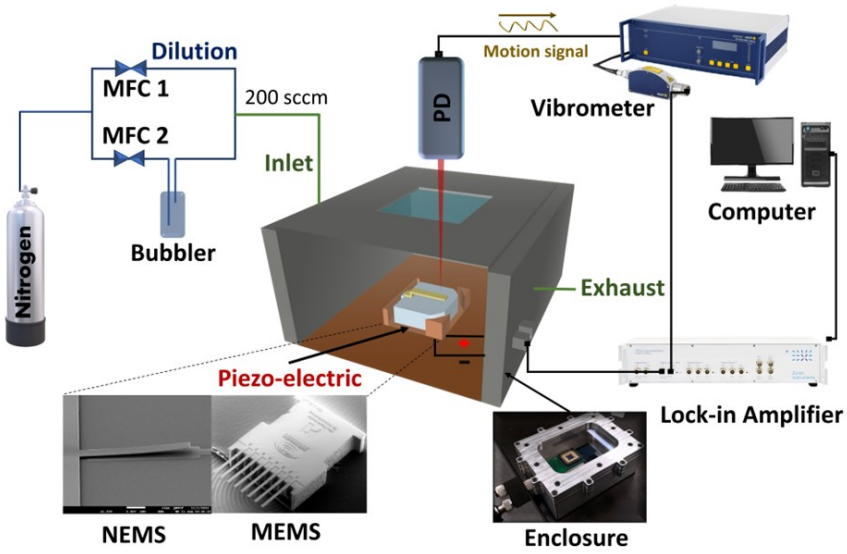



Figure 2.12: Experimental setup.

For characterization and testing of the the MEMS sensors, we employed the same experimental setup described in the previous section.

### 2.2.3 Thermomechanical excitation of the NEMS

Noise-driven sensors rely on thermomechanical excitation, eliminating the need for actuation. This unique characteristic stems from the high compliance of the beam, due to its low thickness of ( $\sim 250$ nm ), making it responsive to Brownian motions, the random

movement of particles driven by their inherent thermal energy. These particles collide with the cantilever structure, causing it to vibrate at its natural frequencies. Those vibrations $w_n(x,t)$ are proportional to the absolute temperature $T$ and counter proportional to the stiffness $k$ and damping per unit mass μ[87]:

$$w_n \propto \sqrt{\frac{T}{k\mu}}$$

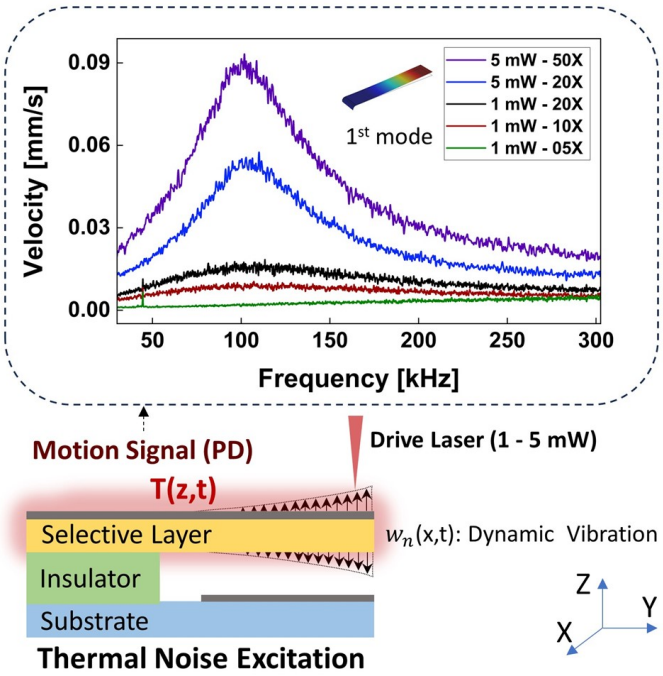



Figure 2.13: FFTs of the NEMS tip velocity under different laser intensity levels.

Consequently, the ZnO cantilever harnesses thermomechanical noise as an actuation source. In this study, two laser sources with rated output power of 1mW and 5 mW and a nominal wavelength of 650 nm and 532 nm, respectively, were employed for optical readout. By changing the laser spot size, we were able to further adjust the intensity of the incident laser on the beam tip and thus change the level of thermal noise. Figure 2.13 shows the FFTs of the tip velocity for three spot sizes of the 1mW laser and two spot sizes of the 5 mW laser obtained using four objective lenses (x5, x10, x20, and x50). Increasing the laser power density was found to increase the level of thermal excitation and the tip velocity.

### 2.2.4 Characterization

The piezoelectric actuator was driven with an unbiased peak-to-peak voltage of 5 V, while its frequency was swept up to obtain the frequency response of the MEMS beam tip velocity in ambient air. The results reveal that the first three modes of both ZnO-coated and MOF-coated sensors were out-of-plane bending modes. Figure 2.14 shows the photodetector voltage amplitude and phase in the vicinity of the second bending mode for a ZnO sensor and a MOF sensor. The corresponding resonant frequencies were found to be $f_2^Z = 163.65\,\text{kHz}$ and $f_2^M = 164.04\,\text{kHz}$.

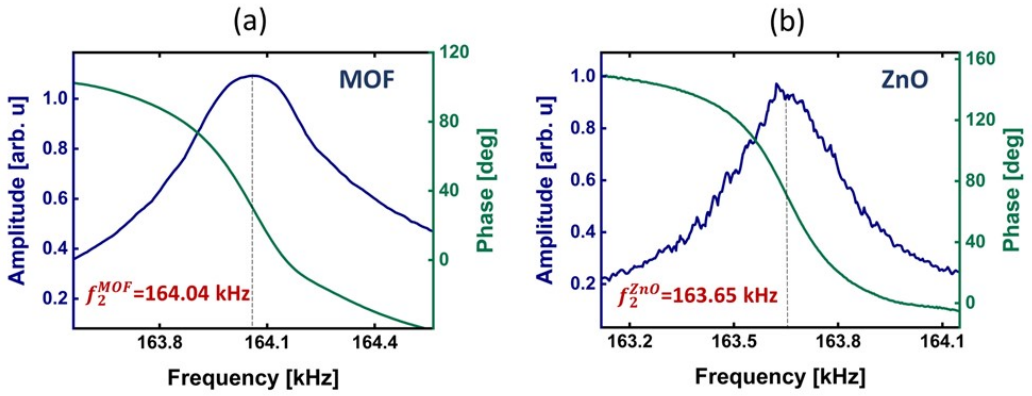



Figure 2.14: The frequency response of the (a) MOF-coated and (b) ZnO-coated MEMS sensors around the 2nd bending mode.

Modal analysis of the NEMS sensors was conducted by optically measuring their tip velocity under thermal noise excitation in ambient air and vacuum (P=1 µTorr). The FFT of the measured velocity shows two out-of-plane bending modes followed by a torsional mode, Figure 2.15 . The natural frequencies of those modes shift from ($f_1^{vac} = 65.62$kHz, $f_2^{vac} = 432.03$ kHz, and $f_3^{\text{vac}} = 625.31$kHz) in vacuum to $\left(f_1^{\text{air}} = 51.87\ \text{kHz}, f_2^{\text{air}} = 311.87\text{kHz}, \text{and } f_3^{\text{air}} = 529.02\text{kHz}\right)$ in air. This drop in natural frequencies is due to the increased mass of the beam as the structural ZnO layer absorbs humidity and oxygen and possibly due to changes in its material properties resulting in a lower stiffness.

### 2.2.5 Sensor comparison

The PLL of the Lock-in Amplifier was used to measure shifts in the natural frequency of the MEMS sensors' second bending mode as they were exposed to different concentrations

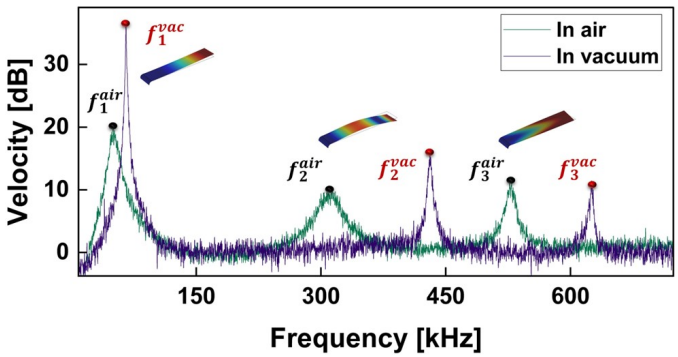



Figure 2.15: The frequency-response curves a NEMS sensor under thermal noise excitation in air and vacuum

of acetone. The shift was measured relative to a baseline resonant frequency, recorded after the test chamber was purged with nitrogen and the sensor reached equilibrium with the nitrogen environment.

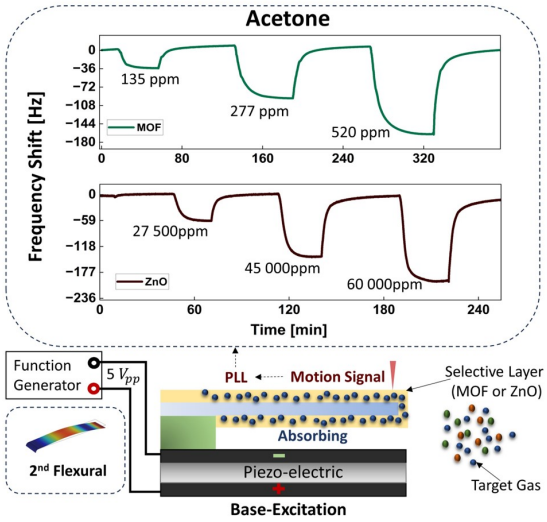



Figure 2.16: The measured frequency shifts of MEMS sensors coated with ZnO and MOF due to exposure to acetone.

Figure 2.16 compares the measured frequency shifts as functions of acetone concentration of a MOF-coated MEMS sensor to a ZnO-coated MEMS sensor. The MOF sensors demonstrate an exceptional responsivity of R = 0.3 Hz/ppm compared to a responsivity

of R = 0.0032 Hz/ppm for the ZnO sensors. This substantial difference underscores the outstanding sensitivity of the MOFs to acetone. The LOD of MOF sensors was calculated as 9 ppb.

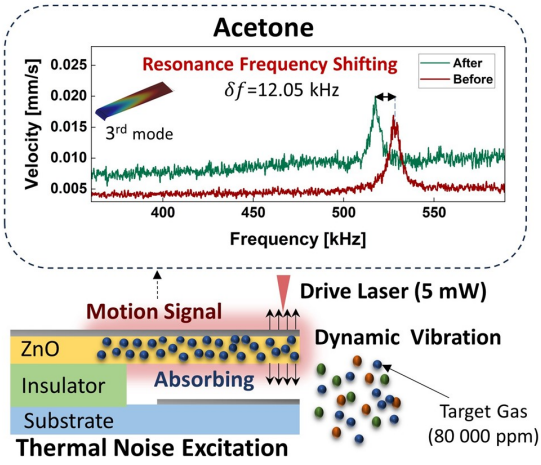



Figure 2.17: Response of the noise-driven NEMS sensor to acetone.

Similarly, we employed the shift in the first torsional mode of the NEMS sensors'as a detector of acetone concentration. Figure 2.17 compares the frequency response curve of the sensor in Nitrogen to that in a Nitrogen environment with acetone concentration of 80,000 ppm. We observed a frequency shift of $\delta f_3 = 12.05\,\text{kHz}$, corresponding to a responsivity of $R = 0.15\,\text{Hz/ppm}$. Comparing MEMS to NEMS ZnO sensors reveals a remarkable 45 -fold increase in sensitivity underscoring the exceptional performance of noise-driven NEMS sensors.

## 2.3 Electrostatic ZnO NEMS SENSORS

In this section, we introduce an electrostatic ZnO NEMS sensor, characterized by a distinct design from that of the sensor utilized in the preceding section. It incorporates an electrostatic field to augment the sensor response by adding capacitive detection to gravimetric detection [88].

The sensor design is inspired by the pioneering work of Mistry et al. [61], incorporating the following key design elements:

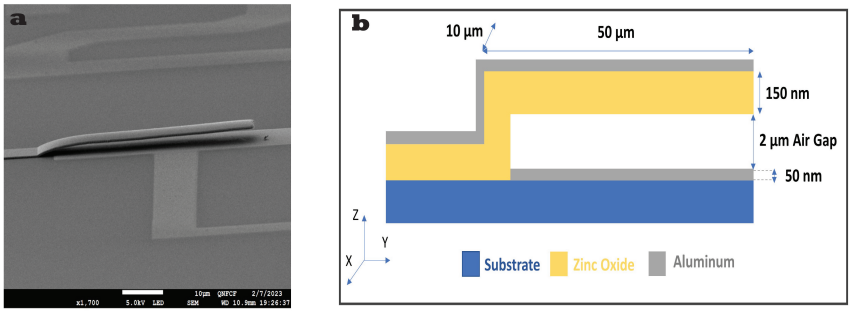



Figure 2.18: (a) An SEM image and (b) a schematic cross-section of the NEMS the beam and its anchor.

- Electrostatic actuation via a parallel plate capacitor configuration: A metal contact deposited on the substrate and a metal layer deposited on top of the structural layer act as the capacitor plates.
- Optical readout: Laser vibrometer is used to measure the sensor frequency response. The top metal electrode serves as a reflective surface.
- Air gap: An air gap of 1.5–2.0 µm is created beneath the structural layer by depositing a sacrificial layer, which is subsequently removed during the release etching step.

The senor structure is depicted in Figure 2.18. Its design dimensions are listed in Table 2.3.

Table 2.3: Summary of the cantilever's dimensions.

| Symbol | Parameter | Value |
|---|---|---|
| $L$ | Length | 50 µm |
| $w$ | Width | 10 µm |
| $t_Z$ | ZnO thickness | 200 nm |
| $t_T$ | Top electrode thickness | 50 nm |
| $t_B$ | Bottom electrode thickness | 50 nm |
| $g$ | Air gap | 1.5–2 µm |

### 2.3.1 Fabrication Process

The steps of the fabrication process are shown schematically in Figure 2.19. The process uses a 3-inch silicon wafer featuring a 300 nm thick thermal oxide layer. This wafer undergoes an initial step of cleaning with acetone and isopropanol. Employing a standard lift-off technique, the bottom electrode and bonding pads are created, Figure 2.19(a). This process entails application of negative-tone resist, UV lithography, and deposition of a 50 nm-thick aluminum (Al) layer through sputter deposition. The wafer is then spin-coated with a 1 µm-thick sacrificial positive-tone photoresist layer and patterned using UV lithography, Figure 2.19(b).

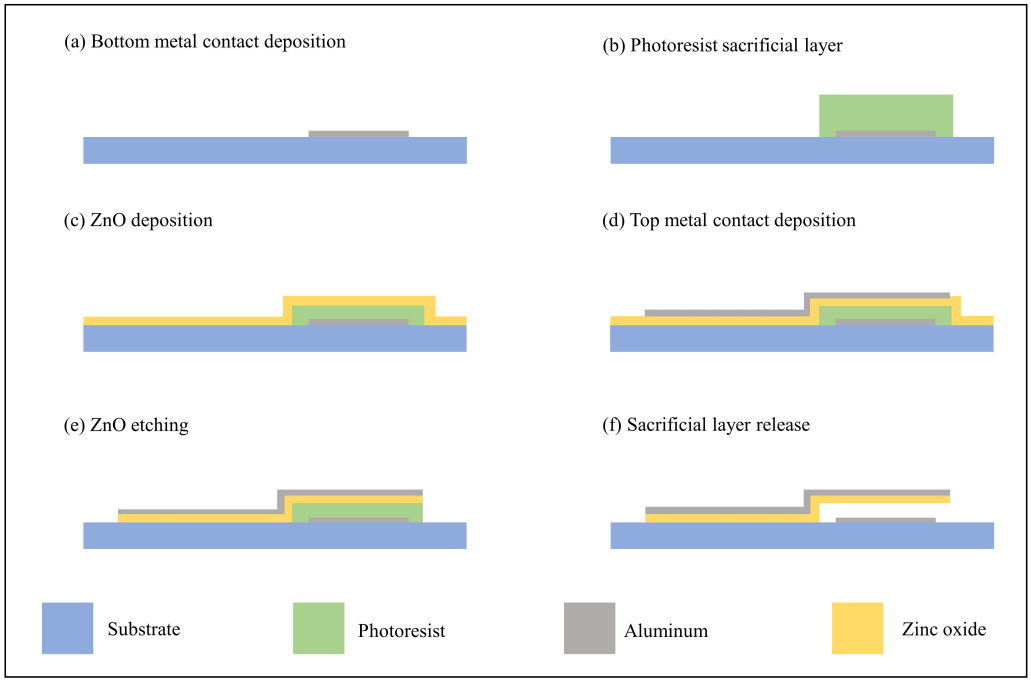



Figure 2.19: Fabrication process

A specialized AP-SALD system is employed to deposit the ZnO layer. Diethylzinc and water are used as zinc and oxygen precursors, delivered by nitrogen as a carrier gas, Figure 2.19(c). The silicon wafer, heated to 200°C, oscillates in-plane to expose its full surface to the precursor flow channels, allowing for the deposition of a 150 nm thick ZnO film in 150 oscillations. The resulting film conforms to the substrate surface, including the sides of the sacrificial photoresist layer, ensuring secure attachment of the structural layer to the

anchors.

A second lift-off process is employed, Figure 2.19(d), to deposit and pattern the top metal electrode. This 50 nm-thick Al layer, deposited via sputter deposition, defines the cantilever's length (50 µm) and width (10 µm). The aluminum top electrode also functions as an etch mask for reactive ion etching (RIE) of the ZnO layer, Figure 2.19(e). RIE of the ZnO layer defines the cantilever and reveals the sacrificial layer underneath it for subsequent release, Figure 2.19(f). Anisotropic oxygen plasma ashing is employed to remove the sacrificial photoresist layer. Unlike the previous NEMS sensor, the process in this case continues until the photoresist is completely removed, as visually verified through SEM. The fabrication process results in the creation of a nano cantilever beam approximately 200 nm thick (composed of 150 nm ZnO and 50 nm Al layers) with a length of 50 µm and a width of 10 µm.

Comparing the resulting beam, Figure 2.18, to that fabricated previously, Figure 2.9, we note that both cantilever are free-standing. However, the latter beam has a bracket-shaped support made completely out of the structural ZnO layer while the former has a flat-shaped support resting on a photoresist anchor.

### 2.3.2 Experimental setup

We employed a high-frequency laser Doppler vibrometer (Polytech UHF-120) to measure the velocity of the cantilever tip oscillations, Figure 2.19. The sensor was wire-bonded to a chip carrier and placed in a custom-made test chamber equipped with an optical port, a gas inlet and a gas outlet. Test gases were generated by passing a carrier gas (nitrogen) through a bubbler containing a liquid analyte. The passage of nitrogen helped to evaporate the liquid.

The total flow entering the test chamber was maintained at a constant value of 200 sccm throughout the experiment. The flow rates of the stream through the bubbler and a nitrogen dilution stream were controlled by two MFCs. The laser beam was focused onto the corner of the cantilever tip through a 50x objective lens to track oscillations of the second bending mode before and after exposure to VOCs, Figure 2.20. The measured velocity-time signal was post-processed to obtain its FFT and derive the frequency response of the sensors. In addition, the sensor was excited with a pulse waveform with an amplitude of V=10 V, a frequency of 156 Hz, and duty cycle of 0.1% during gas sensor testing.

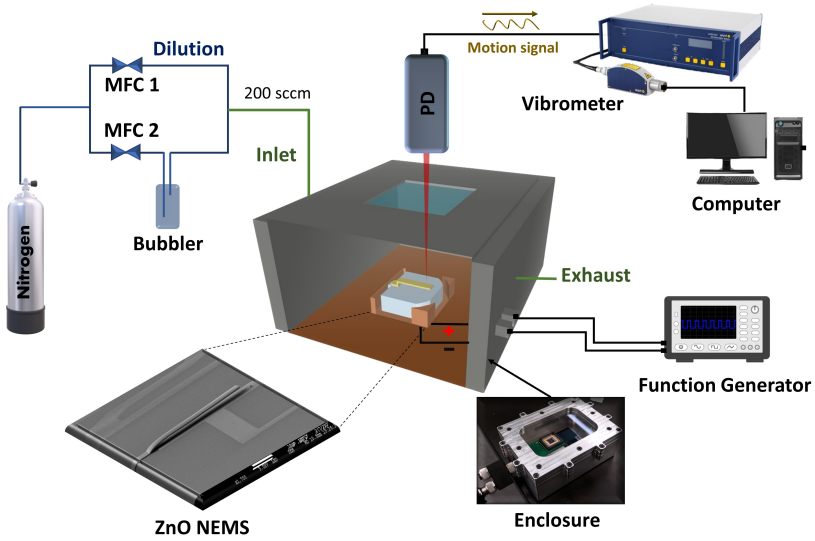



Figure 2.20: Experimental setup employed for characterization and testing of the NEMS sensors

### 2.3.3 Characterization

We employed optical measurement techniques described above to characterize NEMS sensors. Modal analysis was carried out by measuring the tip velocity, a node-free region, in ambient air under thermomechanical noise excitation enhanced by the measurement laser beam ($\lambda = 532\,\text{nm}$), Figure 2.21(a).

The FFT of the measured velocity unveiled three out-of-plane bending modes and two torsional modes, Figure 2.21(b). The bending modes were observed at $f_1 = 100.02\,\text{kHz}$, $f_2 = 704.19\,\text{kH}$ and $f_5 = 2002.02\,\text{kHz}$. The torsional modes were observed at $f_3 = 898.72\,\text{kHz}$ and $f_4 = 1387.06\,\text{kHz}$. The quality factors of the modes in air were evaluated using the half-power bandwidth method as $Q_1 = 8.5$, $Q_2 = 18.5$, $Q_3 = 39.5$, $Q_4 = 52.2$ and $Q_5 = 73.2$.

### 2.3.4 Humidity sensing

First, the NEMS sensor was deployed for humidity sensing. The experimental technique described above was used to obtain the frequency response of the sensors around the second bending mode at four different levels of relative humidity (RH), as depicted in Figure

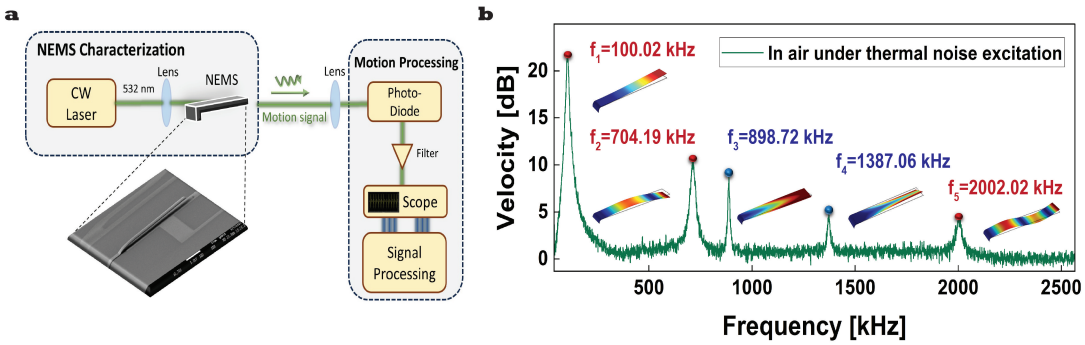



Figure 2.21: (a) Schematic of the optical measurement system used to characterize the DUT. (b) FFT of the cantilever tip velocity under thermal noise excitation.

2.22(a). The relationship between the resonance frequency and RH is illustrated in Figure 2.22(b). It reveals a non-linear trend with a coefficient of determination $R^2 = 0.9908$. It is apparent that an increase in RH levels causes a shift in resonance frequency towards lower values, attributed to the adsorption of water molecules on the cantilever's surface.

The sensor responsivity was calculated as:

$$R = \frac{\partial f}{\partial \mathrm{RH}} \times \frac{1}{f_\circ} \times 10^6 \tag{2.1}$$

where the first term on the right hand-side is derivative of the fit function and $f_\circ$ is the base resonance frequency measured at RH level of 31.5%. The calculated responsivity is plotted as a function of RH in Figure 2.22 (c), illustrating the dependence of sensitivity on the RH level. The LOD is determined by considering the frequency stability of the sensor $f_{\mathrm{noise}} \approx 20\,\mathrm{Hz}$, significantly higher than those encountered where a lock-in amplifier was used in measurements.

To enable a meaningful comparison with Mistry et al.'s work [61], the responsivity in this study was measured in the same humidity range of their work. The calculated responsivity for the NEMS sensor at 5.8% and 28% RH were found to be $R = 22261$ and 3727 ppm/%RH, respectively. In the 30-60% RH range, it was almost linear with an average responsivity of $R \approx 1207\,\mathrm{ppm/\%RH}$. Similar to their case, responsivity was higher at lower RH levels and decreased as the RH level increases. This behavior can be attributed to the occupation of more adsorption sites as the RH level rises, limiting the availability of sites for further molecule adsorption on the cantilever's surface.

Our maximum achieved responsivity at 5.8% RH was found comparable but slightly

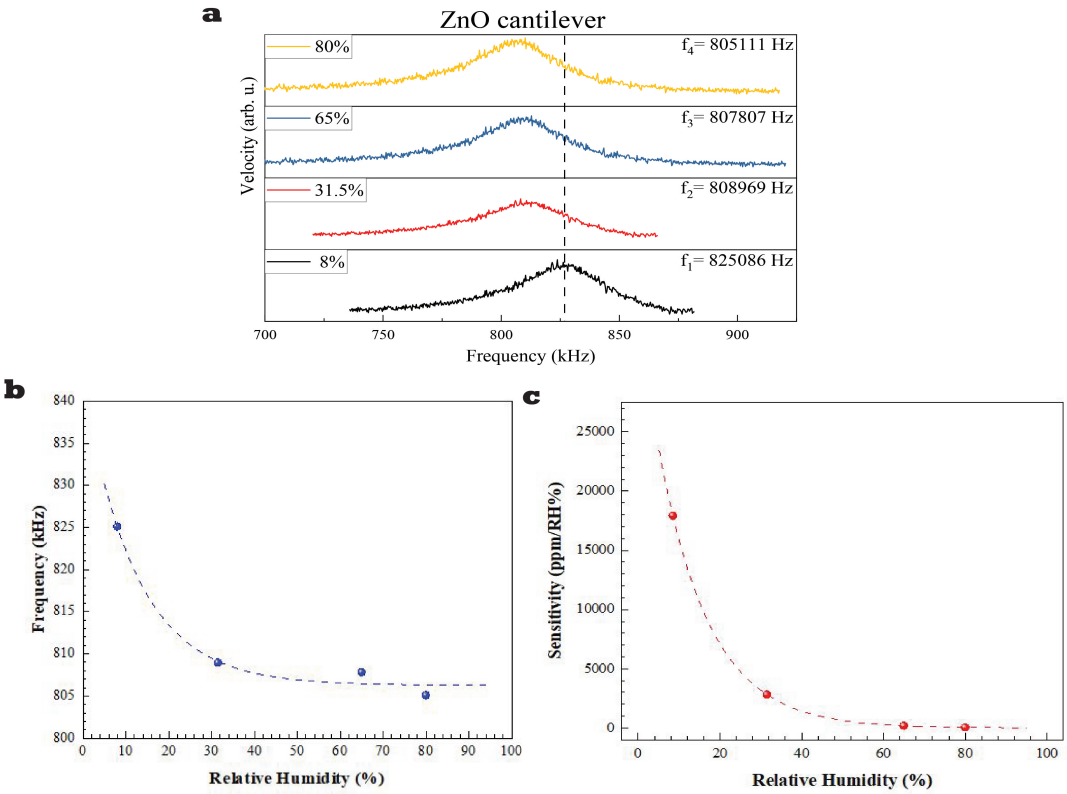



Figure 2.22: Noise-driven sensing of the NEMS sensor to acetone.

lower than that reported by Mistry et al. [61]. This difference is probably due to the higher mass of our sensors featuring a thicker top electrode. Our calculated LOD at 0.034% RH was also lower than that of Mistry et al. due to our improved Q factor resulting in better frequency stability.

### 2.3.5 VOCs sensing

The NEMS sensor was exposed to various concentrations of acetone, ethanol, and isopropanol as per the experimental procedure described above. The frequency response in the vicinity of the second bending mode of the sensor was measured in each case and are shown in Figure 2.23. The concentrations were adjusted by controlling the flow rates through the MFCs to achieve 10%, 25%, 50%, and 75% of the saturation pressure for each gas, corresponding to the gas concentrations listed in Table 2.1. Responsivity to each gas

was calculated by applying a linear fit to the relationship between the measured frequency shift and gas concentration, Figure 2.23(d), then measuring the slope of the fit line.

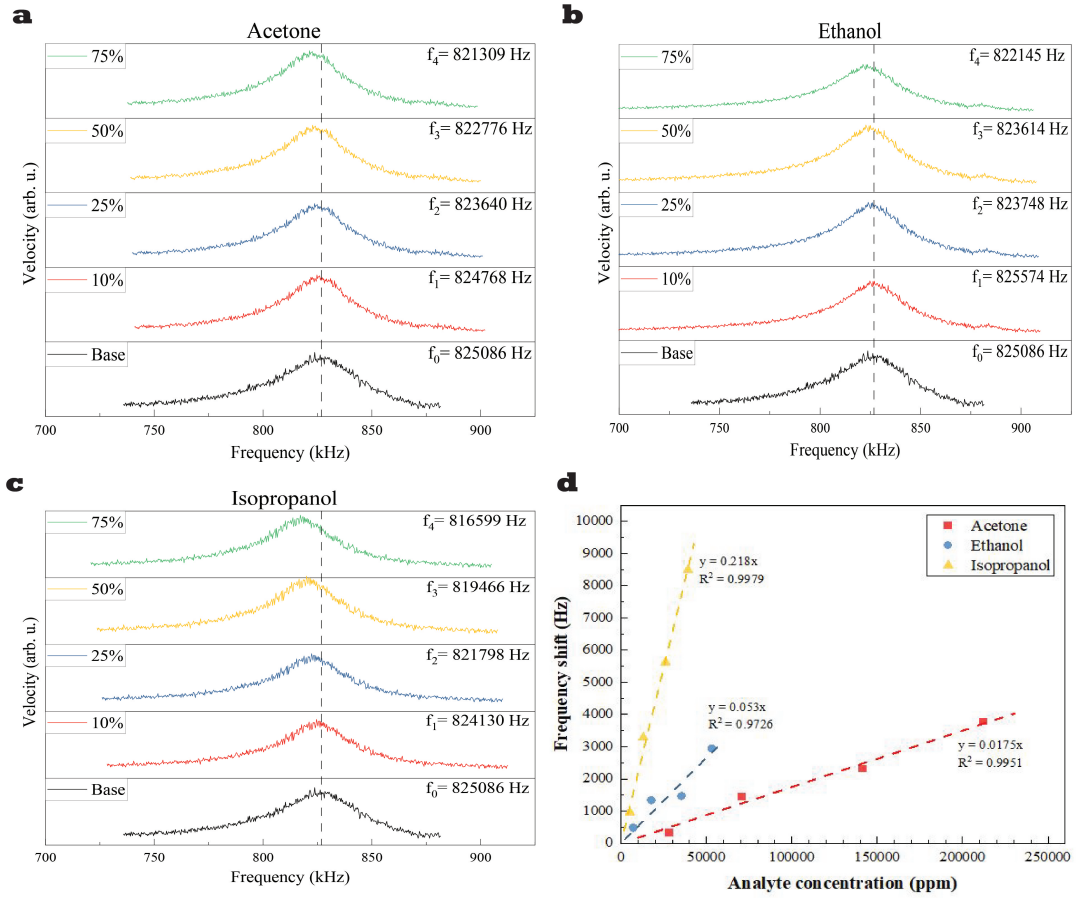



Figure 2.23: Noise-driven sensing of NEMS acetone.

The NEMS sensors responsivity and LOD are listed in Table 2.4 for each of the tested gases. Responsivity was highest to isopropanol. A sensor is considered selective to an analyte, if its responsivity to the analyte proves to be twice or more than that to an interferent [59]. The bare ZnO NEMS sensors' responsivity to isopropanol is four times that to ethanol and twelve times that to acetone. However, confirming its selectivity to isopropanol would require testing with a wider selection of VOCs in order to draw firmer conclusions.

Table 2.4: NEMS sensor responsivity and LOD to VOCs

| Analyte | R (Hz/ppm) | LOD (ppm) |
|---|---|---|
| Ethanol | 0.053 | 1132 |
| Acetone | 0.0175 | 3428 |
| Isopropanol | 0.218 | 275 |

## 2.4 Conclusions

In conclusion, the MOF-CVD approach was utilized to sensitize silicon MEMS with a MOF as a sensing layer for detection of VOCs. Its performance in sensing was compared to that of MEMS cantilevers sensitized with ZnO thin films. The MOF-coated MEMS sensors exhibited superior sensitivity to VOCs, with LODs in the range of ppb, thanks to the high porosity and large surface area of MAF-6. Responsivity can be further improved by reducing the dimensions of the microcantilevers and enhancing the actuation and read-out mechanisms. This technique is solvent-free and compatible with conventional microfabrication processes, making it a promising candidate for the fabrication of highly sensitive gas sensors.

Novel noise-driven ZnO NEMS sensors were shown to achieve similar sensitivity to MOF-coated MEMS sensors by virtue of their high inertial sensitivity. They have the added advantages of autonomy and low power consumption. Future work aims to combine those advantages by transforming a part of the structural ZnO of the NEMS sensor into MOFs via a similar CVD process. The microfabrication process of freestanding metal oxide cantilevers serves dual purposes as a structural layer and a gas-sensitive receptor layer, minimizing potential interlayer damping effects by reducing the number of layers on the cantilever.

ZnO NEMS sensors were also fabricated with a superior design allowing them to withstand significant electrostatic fields. They were driven externally via electrostatic actuation. Frequency response measurements were obtained optically to test their performance as gas sensors. They were found to exhibit remarkable sensitivity to both humidity and VOCs. The ultra-high sensitivity of the ZnO cantilever at low RH levels is particularly advantageous for applications where measurements of low humidity levels are critical.

# Chapter 3

# NEMS Electromechanical Modal Interaction Induced FC

This chapter presents a novel technique for low-power generation of frequency combs (FC) over a wide frequency range. It leverages modal interactions between electrical and mechanical resonators in electrostatic NEMS operating in air to provide a simple architecture for FC generators. A biased voltage signal drives the electrical resonator at resonance which is set to match an integer submutiple of twice the mechanical resonator's resonance. Experimental results demonstrate that the NEMS displacement and output current exhibit more than 150 equidistant peaks in the case of a 2:1 modal interaction and more than 60 equidistant peaks in the case of a 1:1 modal interaction. In both cases, the FSR was equal to the drive frequency. Comparison between the FCs generated by the 2-1 and 1-1 modal interactions demonstrate the superiority of the former in terms of bandwidth and stability. The superior phase coherence of the FC generated via the 2-1 modal interaction was demonstrated via time-domain analysis. Our technique has the flexibility to generate multiple frequency combs and to fine-tune their FSR depending on the number of mechanical modes accessible to and the order of the activated modal interaction. It can be integrated into portable devices and is well aligned with modern miniaturization technology.

## 3.1 Introduction

OFCs are indispensable tools with a wide range of applications in metrology, astronomy, cosmology, and atomic clocks [64, 65, 66, 67, 68, 69, 70], and they have driven significant

progress in these fields [67, 71, 72]. OFCs are generated through various mechanisms, each offering unique advantages and limitations. Notably, a new frontier has emerged with the advent of mechanical frequency combs (FCs), generated through coupled mechanical oscillators, resulting in side-bands with fixed phase relationships [64, 89]. Experimental evidence confirms the presence of mechanical FCs in various systems, establishing connections with established nonlinear dynamics concepts. The consistent frequency and phase relationships within these mechanical comb teeth enable the application of frequency conversion and optical comb techniques.

Mode-locked lasers (MLLs) stand out as the predominant method for generating OFCs [65, 90, 91, 92, 93, 94, 66]. MLLs produce sequences of ultrashort optical pulses at a consistent repetition rate $f_r$ with the pulse width matching comb tooth spacing. These MLLs offer remarkable stability and precision, generating high-resolution combs in the THz range. Accurate control of laser repetition rate $f_r$ and offset frequency $f_\circ$ is critical for effective comb generation [65]. The methodology has evolved to include carrier-envelope phase stabilization through closed-loop feedback [90, 92], as well as the use of continuous-wave laser-pumped resonators to facilitate comb emission via cascaded third-order parametric processes ($X^{(3)}$) [95]. Recent advancements have demonstrated direct generation of optical FCs in continuous-wave-pumped quadratic nonlinear resonators, involving quadratic $X^{(2)}$ processes.

Microresonators offer an alternative route for comb generation, with their compact, high-Q optical cavities supporting whispering gallery modes, resulting in comb-like spectra [70, 66, 96, 97, 98]. They excel in terms of size, efficiency, and stability [96, 97, 98]. Electro-optic modulation, although allowing adjustable comb characteristics, faces challenges related to stability due to microwave source phase noise and component fluctuations [71, 99, 100, 95, 101]. In contrast, optomechanical FCs have emerged as an innovative approach, combining mechanical oscillators and optical cavities to modulate cavity resonance [64, 102, 69, 103, 67, 104, 105, 101]. This method offers advantages such as energy efficiency, reliability, and the potential for on-chip integration. Mechanical motion, driven by lasers and amplified through resonators, facilitates optical comb generation [103, 102]. Adjustable comb tooth spacing has been demonstrated through amplitude modulation [102], and modal expansion has been employed to investigate optical FCs with whispering gallery mode resonators [101].

Phononic FCs emerge by coupling acoustic waves to optical resonators, modulating optical material refractive index, and producing optical FCs [89, 106, 107]. These combs offer high precision and sensitivity to external mechanical forces. Elongated microresonators with nanoscale parabolic effective radius variations, as studied by Sumetsky [101], reveal closely spaced and dense optical eigenfrequencies linked to axially symmetric acous-

tic mode eigenfrequencies. De Cao et al. [89] introduced cubic nonlinearities to generate fast and slow clocks, resulting in FCs around each eigenmode. Maksymov et al. [106] proposed an acoustic-based mechanism for creating equidistant frequency spectra in scenarios where light-based methods are impractical.

Recent years have seen a growing interest in creating FCs by harnessing inherent nonlinearities in the dynamics of mechanical resonators [108, 109]. This pursuit focuses on generating FCs by orchestrating modal interactions between distinct mechanical modes, utilizing embedded nonlinearities. These combs center around a mechanical natural frequency, produced through quasi-periodic responses. Both empirical and theoretical evidence indicates that this regime results from secondary Hopf bifurcations on the large-amplitude branch of M-shaped frequency-response curves [109]. This nonlinear behavior facilitates energy transfer between mechanical modes and an external driving signal. Previous research showcased the generation of mechanical frequency combs using electrostatic MEMS/NEMS resonators, relying on energy-intensive two-to-one modal interactions.

In this work, we introduce an efficient and cost-effective paradigm for FC generation. Leveraging electromechanical modal interaction in an NEMS resonator, we achieved enhanced spacing resolution compared to complex methods. This approach ensures uniform and equally spaced combs, essential for various applications, with minimal power consumption and a compact footprint. 2:1 modal interaction outperforms the 1-1 modal interaction in terms of comb bandwidth and stability. The NEMS-based architecture seamlessly integrates into portable devices and aligns with modern miniaturization trends. This pioneering contribution caters to the growing demands of simplified, modern technology in the FC generation field.

## 3.2 Mathematical model

This section presents a mathematical model capturing the nonlinear dynamics of the NEMS. It couples a mechanical resonator to an electrical resonator. The equation of motion describing the transverse displacement of a point along the neutral axis at a distance of $x$ from the left support of the nanobeam $w(x;t)$ can be written as follows [110, 111]:

$$\rho A\frac{\partial^2 w}{\partial t^2}+c_v\frac{\partial w}{\partial t}+EI\frac{\partial^4 w}{\partial x^4}=\frac{\epsilon b}{2}(\frac{q}{c_m})^2\frac{1}{(g_0-w)^2} \tag{3.1}$$

subject to the boundary conditions:

$$\begin{aligned} w(0) = w'(0) = 0 \qquad & \text{at} x = 0 \\ \frac{\partial^2 w}{\partial x^2} = \frac{\partial^3 w}{\partial x^3} = 0 \qquad & \text{at} x = L \end{aligned} \tag{3.2}$$

where $L, b$, and $h$ denote the beam's length, width, and thickness, respectively, $g_0$ is the initial gap between the beam and the stationary electrode, and $\epsilon$ is air permittivity. The Young's modulus and density of the beam are denoted $E$ and $\rho$, respectively. Its second moment of area can be found as $I = \frac{1}{12} b h^3$. Energy losses due to interactions between the beam and its support and the surrounding air are represented by linear viscous damping with a damping coefficient of $c_v$. The geometrical nonlinearity of inextensibility has been ignored in Eq.(3.1) because of the small ratio of the air gap to the beam length ($\frac{g_0}{L}$). The total NEMS capacitance $C_m$ is displacement-dependent and can be evaluated as:

$$C_m = \int_0^L \frac{\varepsilon b}{(g_0 - w)} dx \tag{3.3}$$

The nanobeam is coupled to an electrical resonator that can be represented by an RLC circuit. The ordinary differential equation describing the flow of electrical charge $q(t)$ through it can be written as

$$L_e \ddot{q} + R_e \dot{q} + \frac{1}{C_m} q = V_{in}(t) = V_{DC} + V_{AC} \cos(\Omega t) \tag{3.4}$$

where $L_e$ and $R_e$ represent the inductance and resistance of the electrical circuit, respectively. A signal generator drives the circuit with a waveform that has a bias of $V_{DC}$, an amplitudes of $V_{AC}$, and a frequency of $\Omega$. Inspecting the system equations, Eqs. (3.1) and (3.4), it can be seen that the mechanical resonator is coupled to the electrical resonator via a quadratic nonlinear term, $q^2$ whereas the electrical resonator is coupled to the mechanical resonator via the displacement-dependent hard nonlinearity $\frac{1}{C_m}$.

The static equilibrium of the corresponding nonlinear system $(w_s, q_s)$ should be obtained via dropping the non-autonomous term in Eq. (3.4), and setting the time-derivative terms equal to zero to obtain the algebraic system:

$$\begin{aligned} EI \frac{d^4 w_s}{dx^4} &= \frac{\epsilon b}{2} \Big( \frac{q_s}{C_s} \Big)^2 \frac{1}{(g_0 - w_s)^2} \\ q_s &= V_{\mathrm{DC}} C_s \end{aligned} \tag{3.5}$$

where

$$C_s = \int_0^L \frac{\epsilon b}{(g_0 - w_s)} dx$$

is the beam capacitance at equilibrium. The system is solved numerically for by applying Galerkin's decomposition method [110, 111]. The NEMS dynamics are Then truncated around the static equilibrium (operating point) by decomposing the displacement and charge into static and dynamic components, as follows:

$$\begin{aligned} w(x;t) &= w_s(x) + w_d(x;t) \\ q(t) &= q_s + q_d(t) \end{aligned} \tag{3.6}$$

Substituting with Eq. (3.6) into Eq. (3.5), we obtain:

$$\begin{aligned} &\rho A \frac{\partial^2 w_d}{\partial t^2} + c_v \frac{\partial w_d}{\partial t} + EI\Big(\frac{d^4 w_s}{dx^4} + \frac{\partial^4 w_d}{\partial x^4}\Big) = \\ &\underbrace{\frac{\epsilon b}{2}\Big(\frac{q_s + q_d}{\int_0^L \frac{\epsilon b}{(g_0 - w_s + w_d)} dx}\Big)^2 \frac{1}{(g_0 - w_s - w_d)^2}}_{I_1} \end{aligned} \tag{3.7}$$

$$L_e \ddot{q}_d + R_e \dot{q}_d + \underbrace{\frac{1}{\int_0^L \frac{\epsilon b}{(g_0 - w_s - w_d)} dx}(q_s + q_d)}_{I_2} = V_{DC} + V_{AC}\cos(\Omega t)$$

Expanding the two fractional nonlinear terms, $I_1$ and $I_2$, in terms of nonlinear polynomials,

we obtain:

$$
\begin{aligned}
I_1 =& \frac{q_s^2}{C_s^2(g_0-w_s)^2} + \frac{2q_s^2}{C_s^2(g_0-w_s)^3}w_d \\
&- \frac{2q_s^2\int_0^L \frac{1}{(g_0-w_s)^2}dx}{C_s^3(g_0-w_s)^2}w_d + \frac{2q_s}{C_s^2(g_0-w_s)^2}q_d \\
&+ \frac{q_d^2}{C_s^2(g_0-w_s)^2} - \frac{4q_s\int_0^L \frac{1}{(g_0-w_s)^2}dx}{C_s^2(g_0-w_s)^2}w_d q_d \\
&+ \frac{4q_s}{C_s^2(g_0-w_s)^3}w_d q_d + \frac{3q_s^2}{C_s^2(g_0-w_s)^4}w_d^2 \\
&+ \frac{3q^{*2}\int_0^L \frac{1}{(g_0-w_s)^2}dx}{C_s^4(g_0-w_s)^2}w_d^2 \frac{q_s^2\int_0^L \frac{2}{(g_0-w_s)^3}dx}{C_s^3(g_0-w_s)^2}w_d^2
\end{aligned}
\tag{3.8}
$$

$$
\begin{aligned}
I_2 =& \frac{q_s}{C_s} + \frac{q_d}{C_s} - \frac{\int_0^L \frac{1}{(g-w_s)^2}dx}{C_s^2}q_s w_d \\
&+ \left(\frac{(\int_0^L \frac{1}{(g-w_s)^2}dx)^2}{C_s^3} - \frac{\int_0^L \frac{2}{(g-w_s)^3}dx}{2C_s^2}\right)q_s w_d^2 \\
&- \frac{\int_0^L \frac{1}{(g-w_s)^2}dx}{C_s^2}q_d w_d
\end{aligned}
\tag{3.9}
$$

The quadratic coupling terms in the NEMS electrical and mechanical resonators are highlighted in red. This analysis shows that electrostatic NEMS dynamics have built-in quadratic nonlinear coupling that can trigger 2:1 modal interaction between their electrical and mechanical resonators.

# Fabrication process for the NEMS

The steps of the fabrication process are shown schematically in Figure 3.1. The process uses a 3-inch silicon wafer featuring a 300 nm thick thermal oxide layer. This wafer undergoes cleaning with acetone and isopropanol before fabrication. Employing a standard lift-off technique, we create the bottom electrode and bonding pads, Figure 3.1(a). This process entails negative-tone resist application, UV lithography, and deposition of a 50 nm-thick aluminum (Al) layer through sputter deposition. The electrode, including a top

metal electrode in Figure 3.1(d), enables both electrical (capacitive) and optical readouts via laser Doppler vibrometer. The wafer is then spin-coated with a 1 µm-thick sacrificial positive-tone photoresist layer and patterned using UV lithography, Figure 3.1(b).

A specialized Atmospheric-Pressure Spatial Atomic Layer Deposition (AP-SALD) system is employed to deposit the ZnO layer. Diethylzinc and water are used as zinc and oxygen precursors, delivered by nitrogen as a carrier gas. The reactor head distributes these precursors via separate outlets, ensuring precise layer formation, Figure 3.1(c). The silicon wafer, heated to 200°C, oscillates in-plane to expose its full surface to the precursor flow channels, allowing for the deposition of a 150 nm thick ZnO film in 150 oscillations. The resulting film conforms to the substrate surface, including the sides of the sacrificial photoresist layer, ensuring secure attachment of the structural layer to the anchors. AP-SALD's rapid deposition rate makes it advantageous for high-volume fabrication. Similarly, using UV lithography allows for low-cost patterning of micron-scale features.

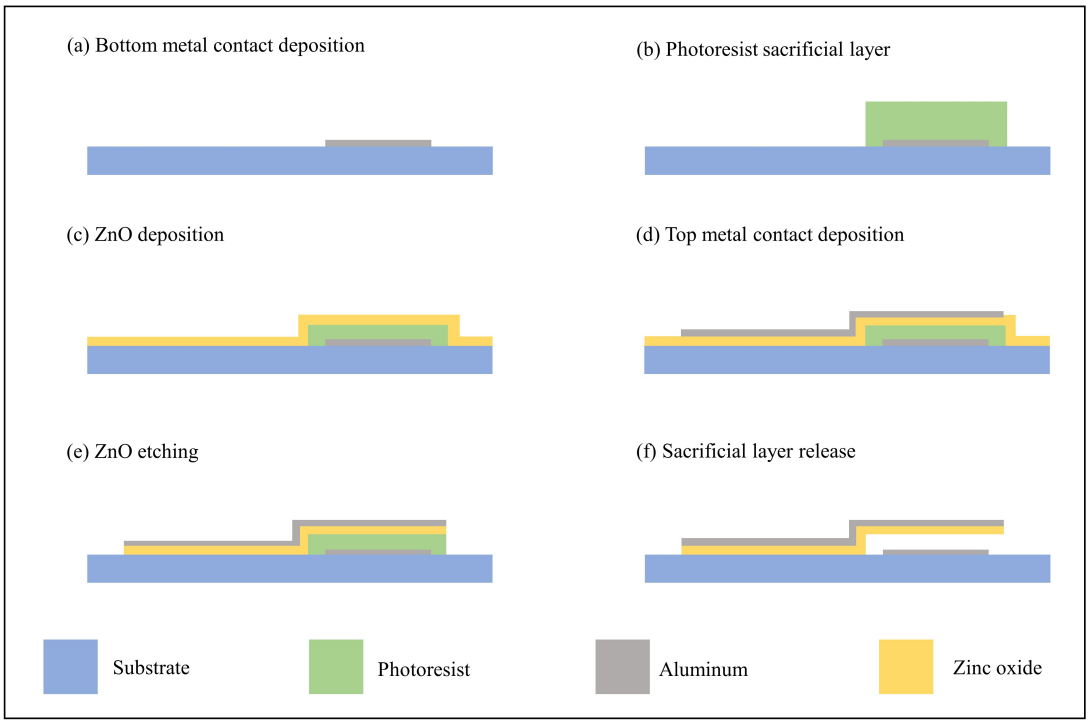



Figure 3.1: Fabrication process

A second lift-off process is employed, Figure 3.1(d), to deposit and pattern the top metal electrode. This 50 nm-thick Al layer, deposited via sputter deposition, defines the

cantilever s length (50 µm) and width (10 µm). The aluminum top electrode also functions as an etch mask for reactive ion etching (RIE) of the ZnO layer, Figure 3.1(e). RIE of the ZnO layer defines the cantilever and reveals the sacrificial layer underneath it for subsequent release, Figure 3.1(f). We employ anisotropic oxygen plasma ashing to remove the sacrificial photoresist layer. The process continues until the photoresist is completely removed, as confirmed visually verified through scanning electron microscopy (SEM). The fabrication process results in the creation of a nano cantilever beam approximately 200 nm thick (composed of 150 nm ZnO and 50 nm Al layers) with a length of 50 µm and a width of 10 µm. A NEMS specimen is shown in Figure 3.2. Despite its substantial aspect ratio, the cantilever remains free-standing, a feat attributed to the conformal ZnO layer and covalent bonds generated during the AP-SALD process, ensuring robust adhesion to the substrate.

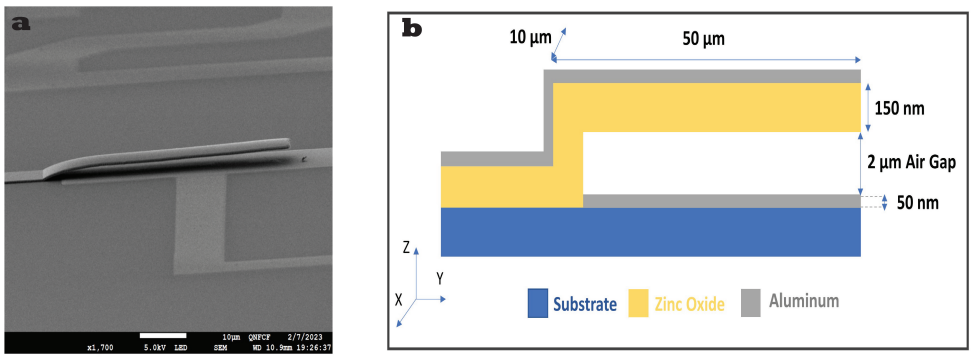



Figure 3.2: The NEMS cantilever; (a) an SEM image showing the beam and its anchor and (b) a schematic cross-section of the beam.

## 3.3 Experimental Setup

Two experimental techniques are employed to measure the electro-mechanical response of the NEMS, electrically and optically. Figure 3.3(a) illustrates the NEMS under study: a pair of coupled electrical, RLC circuit, and mechanical, beam, resonators. The coupling element is the capacitance $C$ in the RLC circuit which is provided by the beam.

### 3.3.1 Electrical measurement

A Vector Network Analyzer (VNA) was employed to characterize the resonant frequency of the RLC circuit $f_e$. The circuit configuration is shown in Figure 3.3(a). The VNA supplied the input power into the NEMS and measured the returned power to evaluate the circuit's ($S_{11}$ parameter) during a frequency sweep. The results were post-processed using a LabView software interface. This experimental setup was used for precise measurement and tuning of $f_e$.

### 3.3.2 Optical measurement

The displacement and velocity of the beam were measured optically using a Laser Doppler Vibrometer (LDV), Figure 3.3(b). In this case, the drive electrical potential difference was supplied to the NEMS via a voltage source (function generator). The laser spot was focused on the beam tip. The measured response was post-processed in the time and frequency domains to obtain the FFT and frequency response of the NEMS. This setup enables precise real-time analysis and visualization of the NEMS response. Frequency-response curves were constructed from the time-domain measurements following the procedure described by Elhady et al. [112]. The FFT plots depicting frequency combs, we have removed the noise floor to provide a clearer view of the well-defined and discernible overall frequency comb pattern. It is worth noting that transitioning from the electrical measurement setup to the optical setup is accompanied by a decrease in the inductance of the RLC circuit. This results in a minor increase in the electrical resonant frequency.

## 3.4 Results and discussion

### 3.4.1 Device and characterization

The device-under-test (DUT) is a nano cantilever beam made of a 150 nm-thick doped Zinc Oxide (ZnO) layer that serves as both a structural and a functional material, unlike the case for conventional sensors. The capacitive readout is provided by a 50 nm-thick Aluminum (Al) layer, on top of the ZnO layer, coupled to a substrate Al electrode, Figure 3.2(b). Figure 3.2(a) shows a scanning electron microscope (SEM) image of a DUT measuring 50 µm long and 10 µm wide.

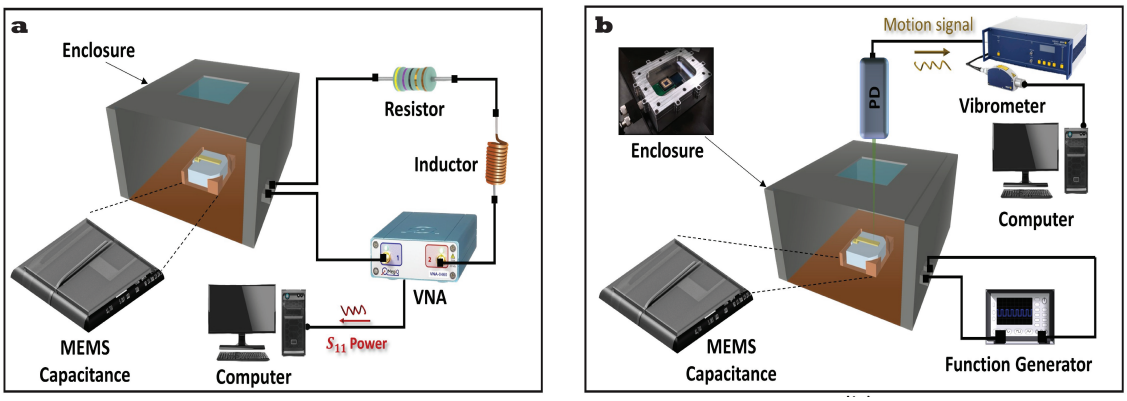



Figure 3.3: The experimental setups used for (b) electrical characterization of the DUT and (b) optical characterization of the DUT as well as observation of the generated frequency combs.

A biased harmonic potential difference:

$$v(t) = V_{\mathrm{DC}} + V_{\mathrm{AC}} \cos(2\pi f t)$$

is applied between the top and the substrate Al electrodes. It creates an electrostatic field within the air gap and results in an attractive force between the electrodes. The magnitude of this force is proportional to $v^2(t)$. It is composed of a DC component and two time-varying components with frequencies of $f$ and $2f$. The aim of this work is to harness the out-of-plane oscillations of the beam under this force as a FC generator by incorporating it into a NEMS composed of an electrical resonator, RLC circuit, coupled to a mechanical resonator, the beam. A schematic of the NEMS is shown in Figure 3.3(a). We employ resonance matching [113] to drive the NEMS. Therefore, the natural frequency of the electrical resonator $f_e$ is tuned, by adjusting the circuit inductance $L$, to match either the natural frequency of the first out-of-plane bending mode ($f_m$) or twice that value ($2f_m$), thereby establishing a commensurate one-to-one ($f_e \approx f_m$) or two-to-one ($f_e \approx 2f_m$) ratio between an electrical and a mechanical modes, resulting in driving the 1:1 or 2:1 electromechanical modal interactions (akin to the fundamental parametric resonance or principal parametric resonance of the mechanical resonator, respectively.). In the vicinity of $f_e$, the amplitude of the voltage signal supplied to the electrical resonator is amplified by approximately its quality factor [113].

We employ electrical and optical measurement techniques, Figure 3.4, to investigate the electro-mechanical response of the NEMS. Modal analysis of the beam was first carried

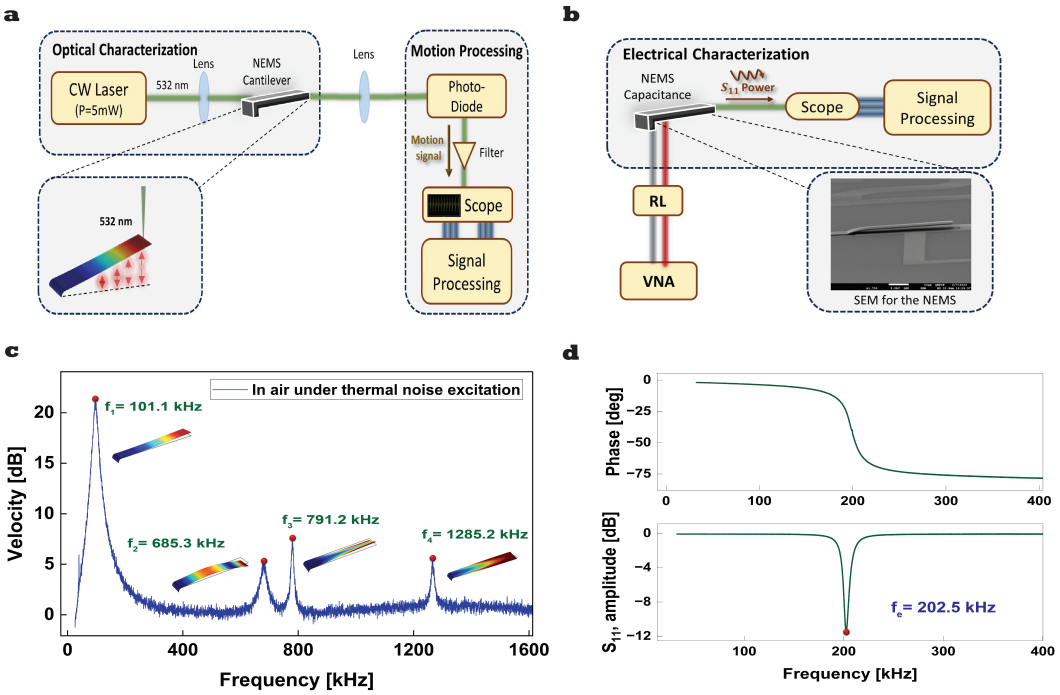



Figure 3.4: Schematics of the (a) optical and (b) electrical measurement systems used to characterize the DUT. (c) FFT of the cantilever tip velocity under thermal noise excitation. (d) The measured magnitude and phase of the returned electrical power $S_{11}$ of the DUT.

out via optical measurement of the tip velocity, a node-free region, under thermal noise excitation in ambient air. The Fast Fourier Transform (FFT) of the measured velocity unveiled two out-of-plane bending modes and two torsional modes, Figure 3.4(c). The bending modes were observed at $f_1 = 101.1\,\text{kHz}$ and $f_2 = 685.3\,\text{kH}$ and the torsional modes were observed at $f_3 = 791.2\,\text{kHz}$ and $f_4 = 1285.2\,\text{kHz}$. The quality factors of the modes in air were evaluated using the half-power bandwidth method as $Q_1 = 8.5$, $Q_2 = 18.5$, $Q_3 = 39.5$, and $Q_4 = 52.2$.

The electrical resonance frequency was set to $f_e = 202.5\,\text{kHz}$, which corresponds to 2:1 modal interaction ($f_e \approx 2f_m$), using a $L = 13\,\text{mH}$ inductor. The unactuated NEMS capacitance was measured as $C = 20\,\text{pF}$ and a resistor ($R = 1\,\text{k}\Omega$) were introduced to prevent current overloading. The electrically measured frequency response of the NEMS in the frequency range of $[10, 400]\,\text{kHz}$ is shown in Figure 3.4(d). The magnitude and phase plots reveal a significant drop in returned power and phase angle at $f_e$. The same setup

was used to drive the 1:1 modal interaction. In this case, the inductance of the electrical resonator was set to $L = 55\,\text{mH}$ which resulted in a measured electrical resonance of $f_e = 101.2\,\text{kHz}$, corresponding to a one-to-one ($f_e \approx f_m$) modal interaction, Figure 3.5.

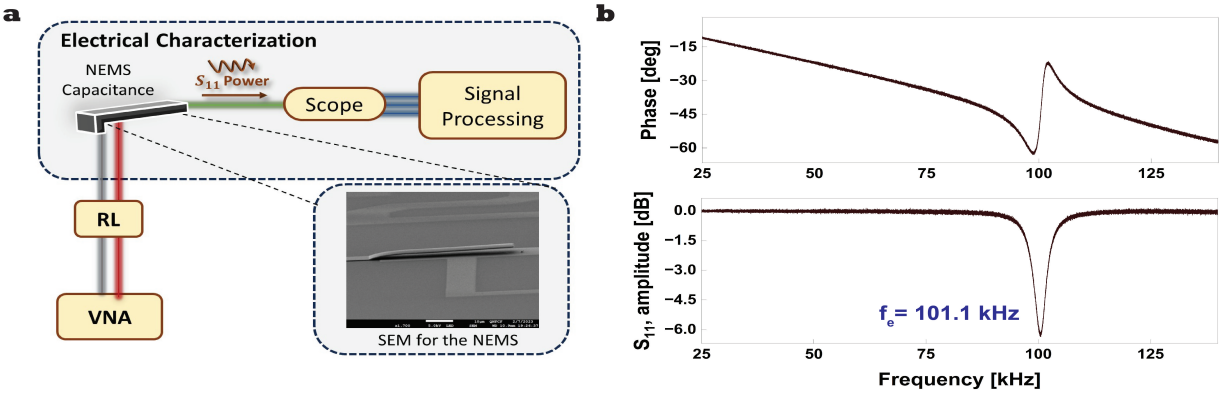



Figure 3.5: Schematic of the electrical measurement system used to characterize the DUT, (b) The measured magnitude and phase of the returned electrical power $S_{11}$ of the DUT for the 1:1 modal interaction case

### 3.4.2 Frequency Combs

#### Two-to-one electro-mechanical modal interaction

We obtained the frequency response of the NEMS by sweeping the frequency of a biased harmonic signal in the vicinity of electrical resonance $f_e$. This frequency range enables the direct excitation of the electrical mode. In the presence of quadratic coupling between the mechanical and electrical resonators, and a commensurate 2:1 ratio between $f_e$ and $f_m$, it also results in the indirect excitation of the mechanical mode once the excitation level crosses the threshold necessary to activate the energy channel between the modes. Figure 3.6(a) provides a schematic illustration of the frequency response before and after triggering this modal interaction.

Figure 3.6(b) depicts the frequency-response curves obtained in ambient air for an excitation force below the activation level (black line) with $V_{\text{dc}} = 0.6V$ and $V_{\text{ac}} = 0.7V$ and above the activation level (blue line) with $V_{\text{dc}} = V_{\text{ac}} = 0.9V$ as the excitation frequency is swept from $f = 194\,\text{kHz}$ to $211\,\text{kHz}$. The frequency response transitions from a single resonant peak, corresponding to electrical resonance, below activation to the characteristic

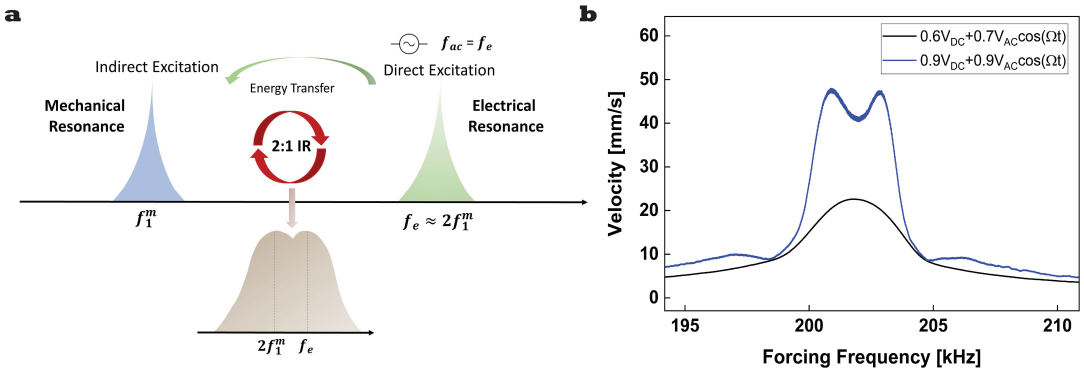



Figure 3.6: (a) A schematic illustrating the 2:1 electro-mechanical modal interaction employed in this study. (b) The optically measured DUT frequency-response curves below ($V_{\mathrm{DC}} = 0.6V$, $V_{\mathrm{AC}} = 0.7V$) and above ($V_{\mathrm{DC}} = V_{\mathrm{AC}} = 0.9V$) the activation level.

two resonant peaks above the activation level. The remarkable efficiency of this process can be seen by comparing the drive voltage used to achieve this resonance to the static pull-in voltage of the nanobeam (70 V). This highlights the FC generator's potential for low-power and resource-efficient utilization.

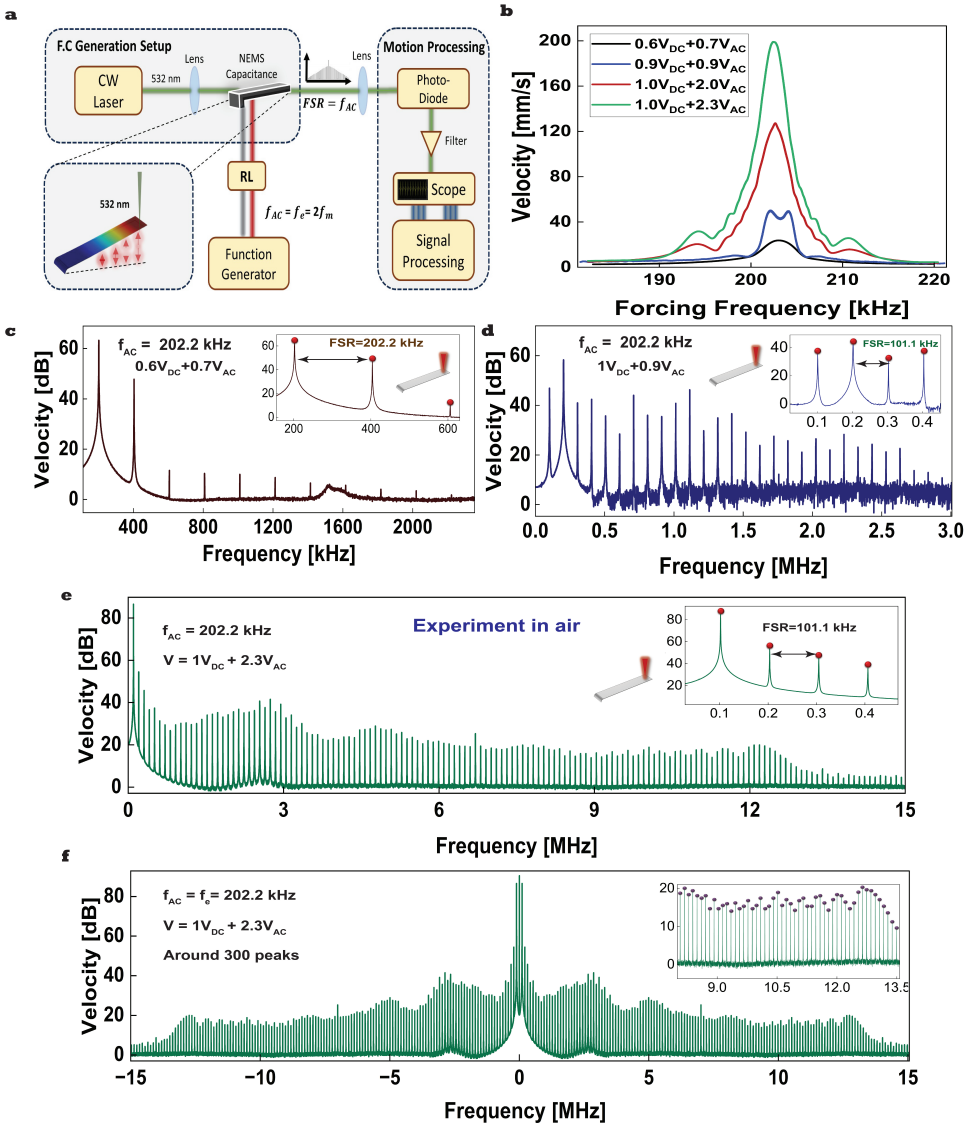



Figure 3.7: (a) A schematic of the experimental setup. (b) The measured frequency-response curves, for four levels of excitation. The measured FFT of the cantilever's tip velocity in air (c) below, (d) just above, and beyond activation level. (f) The complex FFT of the cantilever's tip velocity in air.

Increasing the excitation level with the voltage waveform $V_{DC} = 1V$ and $V_{AC} = 2V$, the two resonant peaks merge resulting in a wider half-power bandwidth. The frequency-

response curve, red line in Figure 3(b), shows a single resonant peak at $f = 202.4\,\text{kHz}$, positioned between the two previous local maxima observed at 201.4 kHz and 203.2 kHz. As the forcing level increases further with a voltage waveform of $V_{DC} = 1V$ and $V_{AC} = 2.3V$, the peak velocity experiences a significant increase, reaching tenfold of that observed below the activation level. The location of the resonant peak also shifts to lower frequencies $f = 202.2kHz$, as larger motions result in larger effective capacitance and a stronger effective electrostatic field.

We analyzed the frequency content of the NEMS response when excited close to resonance, at a frequency of $f = 202.2\,\text{kHz}$, with forcing levels below and above the activation level. The FFTs of the beam tip velocity were evaluated for the voltage waveforms ($V_{\text{DC}} = 0.6V$, $V_{\text{DC}} = 0.7V$), ($V_{\text{DC}} = V_{\text{AC}} = 0.9V$) and ($V_{\text{DC}} = 1V$, $V_{\text{AC}} = 2.3V$) and are presented in Figures 3.7(c), (d), and (e). Below the activation level ($V_{DC} = 0.6V$, $V_{AC} = 0.7V$), the NEMS response exhibits only a handful of uniformly spaced FCs in the spectrum up to 2 MHz corresponding to the harmonic of the excitation frequency, Free Spectral Range ($FSR$) $= f$. Just above the activation level ($V_{\text{ac}} = V_{\text{DC}} = 0.9V$), Figure 3.7(d), FCs appear at $f/2$ and its harmonics corresponding to the mechanical mode. The similarity in power levels across the peaks at $f_m \approx f/2$ and $f_e \approx f$ indicate the activation of a modal interaction energy channel between the electrical and mechanical modes. Energy exchange results in a wider distribution of power over the spectrum with 30 FCs appearing in the spectrum up to 3 MHz uniformly spaced at a distance of $FSR = f/2$ from each other. As the driving voltage increases to $V_{\text{DC}} = 1V$ and $V_{\text{AC}} = 2.3V$, Figure 3.7(e), the NEMS response evolves into a wide spectrum frequency comb with 150 electromechanical FCs, similar in power, equally spaced at $FSR = f/2$, and covering the frequency domain up to 15 MHz. Figure 3.7(f) shows the complex FFT of the response illustrating a soliton centered at $f = 0$.

We compare in Table 4.2 our FC to other phononic FCs realized recently. The comparison underscores the significance of modal interaction in terms of power efficiency, simplicity, and the number of realized teeth across the comb, one order of magnitude higher than all others reported in the literature to date. We note that operating our frequency comb generator in a vacuum, like those reported here, will result in even wider and more powerful frequency combs.

The strength of the generated FCs is dependent on the activation of the modal interaction and the resulting energy exchange between the electrical and mechanical modes. To illustrate this, we excited the electrostatic NEMS with the same voltage waveform ($V_{\text{dc}} = 1V$ and $V_{\text{ac}} = 2.3V$) at a frequency of $f = 206\,\text{kHz}$, outside the interaction window. The resulting spectrum, Figure 3.8, contained only 10 peaks up to 2 MHz spaced at $f$.

Table 3.1: Comparison of FCs in NEMS/MEMS

| Material | Pressure | Base Frequency | FSR | # of Combs |
|---|---|---|---|---|
| ZnO[ this work] | Ambient | 101.1kHz | 10kHz | 3000 |
| $Si_3$ $N_4$[64] | $< 10^{-5}$ mbar | 118kHz | 118kHz | 35 |
| SiN[114] | $< 10^{-4}$ mbar | 6.52MHz | 1.1kHz | 12 |
| Graphene [115] | $< 10^{-2}$ mbar | 2.87MHz | 28.7kHz | 16 |
| $MoS_2$[116] | $2 \times 10^{-2}$mbar | 24MHz | 26.45kHz | 15 |
| Si[117] | High vacuum | 26kHz | $0.8 - 2.6$kHz | 25 |
| Si[118] | 70 mbar | 417kHz | 0.103kHz | 27 |
| AIN/Si[113] | – | 3.86MHz | 2.6kHz | 9 |

**One-to-one electro-mechanical modal interaction**

In this section, we describe the generation of FCs based on 1:1 electro-mechanical modal interaction. First, the electrical resonator frequency is set to $f_e = 101.2\,\text{kHz}$, such that $f_e \approx f_m$, as described above. The cantilever beam is then driven by a voltage waveform with a constant bias of $V_{DC}$=1 V as the excitation frequency $f$ is swept from 90 kHz to 110 kHz. Similar to the 2:1 case, the peak corresponding to electrical resonance is observed for low excitation levels ($V_{AC}$=0.7 V), the black curve in Figure 3.9(a). Increasing the excitation level ($V_{AC}$=0.9 V), triggers 1:1 modal interaction and results in an M-shaped frequency-response curve, blue line in Figure 3.9(a), where the mechanical and electrical resonance peaks are observed. Increasing the voltage amplitude further to $V_{AC}$=2.3 V results in merger of the two resonant peaks into a single dominant peak between them located at $f = 101.95$kHz.

Exciting the NEMS resonator at a frequency close to that of the peak, $f = 101.95\,\text{kHz}$ results in the frequency comb shown in Figure 3.9(b) obtained from the FFT of the nano beam's velocity. The NEMS response reveals 60 evenly spaced peaks covering the frequency spectrum from 0 to 6 MHz. The spacing between the peaks corresponds to the excitation frequency $FSR = f_e$. Comparing these results with those obtained from the 2:1 modal interaction from the same excitation level, illustrates the weaker power interaction

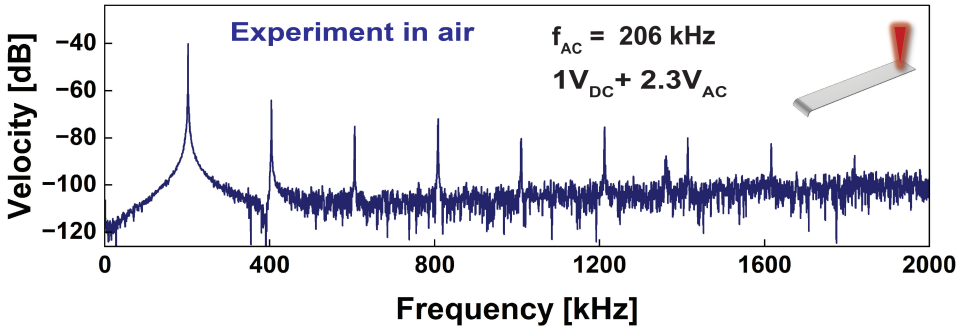



Figure 3.8: The measured FFT of the cantilever's tip velocity in air under an excitation of $V_{DC}$=1 V, $V_{AC}$=2.3 V, and $f$ = 206 kHz

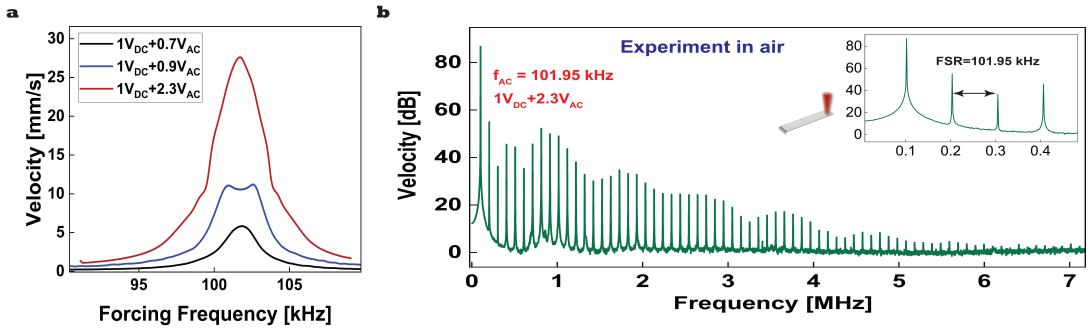



Figure 3.9: (a) The measured frequency-response curves, for three excitation levels as the frequency is swept from 90 kHz to 110 kHz. (b) The measured FFT of the cantilever's tip velocity in air demonstrating the frequency comb generated under an excitation of $V_{DC}$=1 V, $V_{AC}$=2.3 V, and $f$ = 101.95 kHz

and resulting peaks of the 1:1 modal interaction. It is worth noting that even when the excitation levels increases, the frequency comb generated by the 1:1 modal interaction does not expand over the frequency spectrum unlike that of the 2:1 modal interaction.

### 3.4.3 Stability of the frequency combs

#### Quality factor

In this section, we investigate frequency stability and phase coherence of the generated FCs. Frequency stability is indispensable in ensuring the precision and frequency refer-

ences of wave packet generators. The frequency stability of NEMS resonators is counter proportional to the quality factor $\delta f \propto 1/\sqrt{Q}$ [119]. The quality factor of the mechanical mode was measured in air at $Q_m = 8.5$. When excited within the NEMS resonator under the 1:1 modal interaction scheme, the quality factor we found to increase to $Q = 25$ which enhances the frequency stability of the NEMS generated FCs compared to the mechanical resonator. The lower impedance of the NEMS also enhances power transfer to the NEMS resulting in a 60-peak wide FC.

Under the 2:1 modal interaction excitation scheme, a substantial improvement in the quality factor, and therefore frequency stability, is realized with the measured quality factor increasing by an order-of-magnitude to $Q = 145$. This is a result of noise squeeze realized due to the principal parametric resonance excitation conditions in this case. The enhanced quality factor also expands the generated FC to cover 150 peaks. This in-depth understanding of the underlying mechanisms elucidates the pivotal role of the 2:1 and 1:1 modal interactions in enhancing the stability and range of the FCs.

**Phase coherence**

To investigate the frequency stability of the FCs, we evaluated their phase coherence. A comparison between phase coherent and phase incoherent frequency combs is shown in Figure S6. It can be seen that phase incoherence is revealed in the time-histories of the signal (displacement) and its time derivative (velocity) which cease to have distinct maxima and minima as phase incoherence result sin drift between the various frequency components in the signal. Similarly, phase incoherence results in a wandering phase portrait randomly visiting different areas withing reachable phase-space. Unlike the case for coherent FCs where the constituent harmonics result in a single closed orbit.

we considered an oscillatory signal composed of 150 harmonics to study the impact of the non-coherent phase on time-domain and frequency-domain responses and phase portrait.

$$x(t) = \sum_{n=1}^{150} X_n \cos\left(n\Omega t + \phi_n\right) \tag{ES.11}$$

Assuming $\Omega$=5. For the case in which $\phi_{\mathrm{i}}$=0 (i=1,2,...,150), the signal is phase-coherent. Figure S6(a) shows the short scope of the signal in frequency domain and figures S6(c and e) show the short scope of the signal in time domain, and phase portrait is shown in figure S6(g). Comparing phase portrait and time domain responses to the NEMS responses

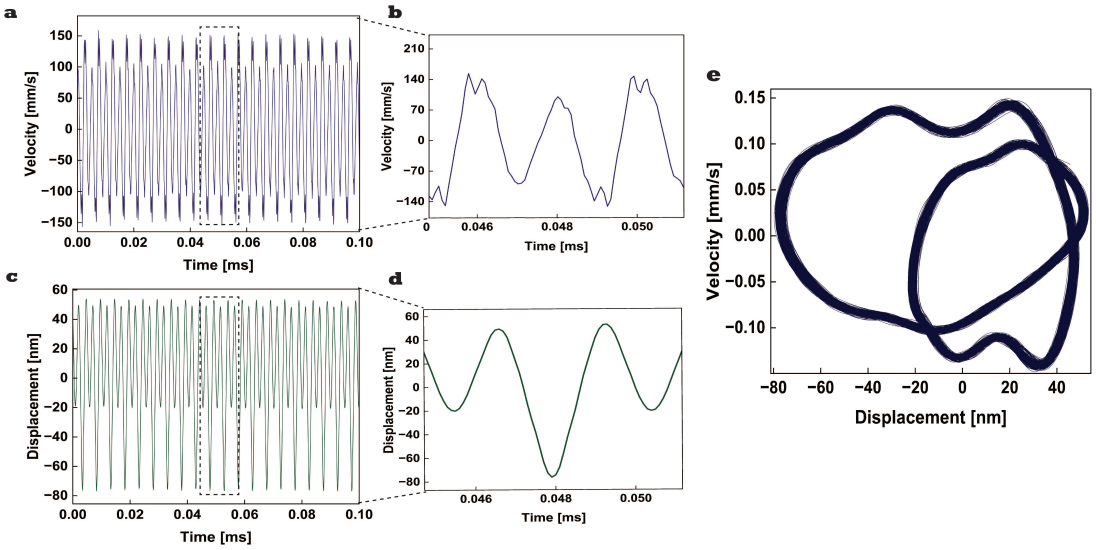



Figure 3.10: The measured time-histories of the beam tip displacement and velocity under electrical excitation with the waveform ($V_{DC} = 1\,\mathrm{V}$, $V_{AC} = 2.3\,\mathrm{V}$), and $f = 202.2\,\mathrm{kHz}$ and (e) the corresponding phase portrait.

shown in Figure 5, it can be concluded that the NEMS displacement and velocity responses obtained from experimental measurements are phase-coherent.

In this work, we measured the nanobeam tip displacement and velocity in time-domain under the excitation waveform ($V_{DC} = 1V$, $V_{AC} = 2.3V$) and a 2:1 modal interaction with $f = 202.2\,\mathrm{kHz}$, corresponding to the FC shown in Figure 3.7. The time-histories of the displacement and velocity, shown in Figure 3.10(a), reveals regular and distinct maxima and minima, inset of Figure 3.10(a), providing confirmation of the phase coherence of the FC. Likewise, the phase portrait of the orbit corresponding to the FC over thousands of forcing cycles, Figure 3.10(b), exhibit a distinct closed orbit consisting of two loops, a characteristic feature of the 2:1 modal interaction. No drift over time is observed in the phase portrait.

However, when different phase values are assumed for each harmonic, introducing non-coherency in phase, the oscillatory signal described in Eq. (Eq.11) takes on the shape depicted in Figure 3.11(d and f). This figure illustrates that the periodic time history of the signal includes primary peaks as well as smaller irregularly distributed peaks within a single period. Furthermore, the phase portrait of the non-coherent signal exhibits a random pattern. It's crucial to emphasize that discerning phase coherency cannot be determined

by examining the amplitude-frequency plot of a Fast Fourier Transform (FFT), as seen in Figures 3.11(a) and 3.11(b).

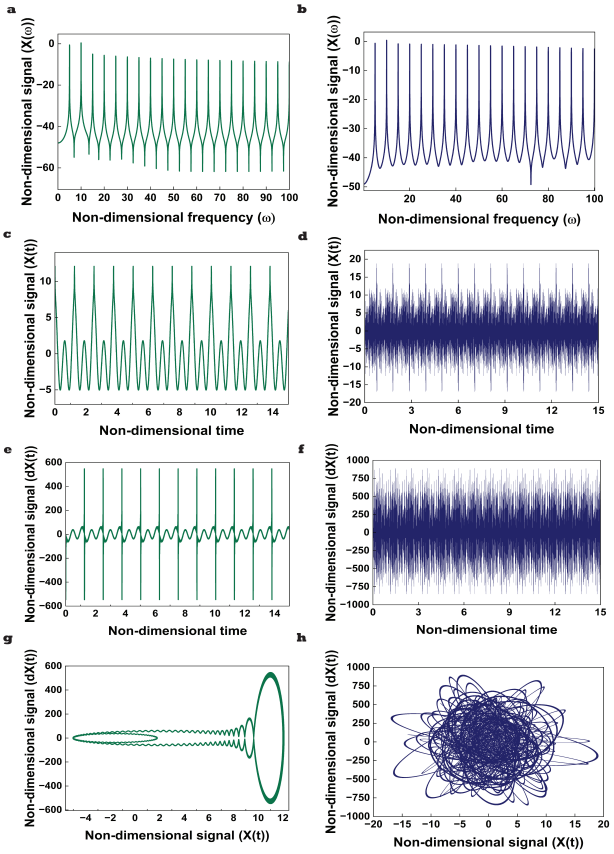



Figure 3.11: The frequency-domain, the time-domain, and the phase portrait of the analog signal presented in Eq. (S11) are demonstrated, respectively, for $\phi_i = 0$ in (a), (c), (e) and (g), and for $\phi_i \neq 0$ $(i = 1, 2, ..., 150)$ in (b), (d), (f) and (h).

## 3.5 Conclusion

In conclusion, this study has successfully demonstrated the development of an energy-efficient technique for the generation of electro-mechanical frequency comb via modal interactions between an electrical resonator and a mechanical resonator. An electrostatic

NEMS made of a resonant drive circuit and an nanobeam was deployed as a platform to demonstrate the technique. In one case, the electric circuit's inductance was tuned to match its resonant frequency to twice the resonant frequency of the beam's out-of-plane bending mode, thus enabling an energy efficient 2:1 modal interaction between the electrical and mechanical modes. The results show the generation of 150 evenly spaced peaks covering a 15 MHz-wide spectrum, confirming successful creation of low voltage ($< 5V$) FCs. In another case, we used the same NEMS to generate FCs via 1:1 modal interaction by tuning the electric circuit's inductance to match its resonant frequency to the resonant frequency of the beam's out-of-plane bending mode. The resulting FC had 60 evenly spaced peaks covering a 6 MHz-wide spectrum. This result highlights the advantages of the 2:1 modal interaction, in terms of FC width and stability, over 1:1 interaction while also illustrating the flexibility of the underlying technique to use various modal interactions.

# Chapter 4

# Generation of Soliton Frequency Combs in NEMS

In this chapter, we present an innovative approach leveraging combination internal resonances within a NEMS-phononic cavity to generate soliton FCs spanning a broad spectrum. In time-domain, the FCs take the form of a periodic train of narrow pulses—a highly coveted phenomenon within the realm of nonlinear wave-matter interactions. Our method relies on an intricate interaction among multiple vibration modes of a bracket-nanocantilever under excitation by a continuous-wave (CW) laser source and an electric wave source. Enabled by the strong nonlinearity of the electrostatic field, they orchestrate the formation of mechanical wave-packets. Through numerical simulation and experimental validation, we demonstrate that amplifying the thermally excited motions of the NEMS with the external electrostatic forcing tuned to excite the superharmonic resonance of order-n ($> 5$) of the fundamental mode and exploiting combination internal resonances, we can generate multiple stable localized mechanical wave packets with different lobe sizes embodying soliton states I and II. Encompassing over 3000 spectral lines, these wave packets effectively couple low-frequency to high-frequency modes of the NEMS, representing a significant breakthrough with profound implications for quantum computing and metrology. Notably, this soliton generator can seamlessly integrate into portable devices, aligning with contemporary miniaturized technology, Figure 4.1.

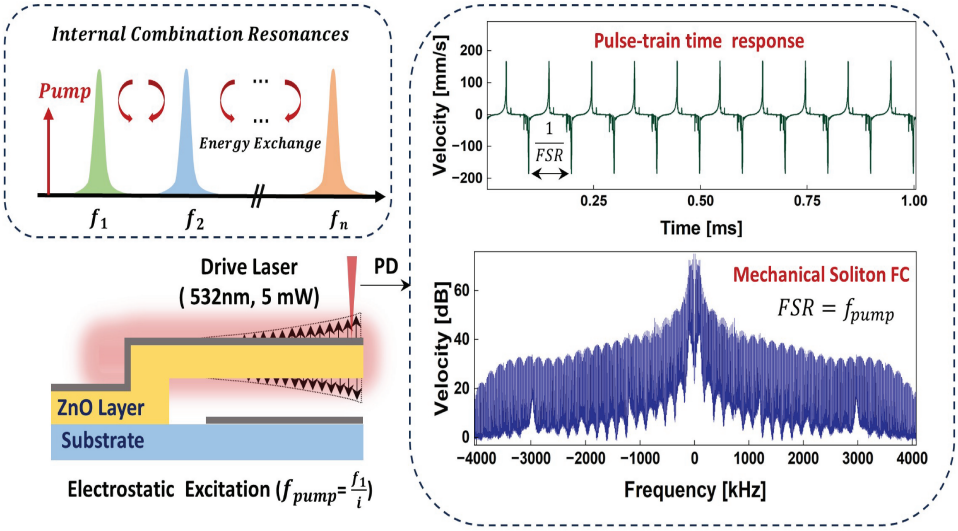



Figure 4.1: Graphical abstract

## 4.1 Introduction

Over the last 25 years, OFCs have made a resounding impact, shaping fields from metrology to astronomy [64, 65, 66, 67, 68, 69, 70]. Their frequency coherence established them as essential metrology tools in labs worldwide [67, 71, 72]. Recent strides in nonlinear optical resonators have harnessed the power of optical solitons, by balancing nonlinearity and dispersion to enhance the stability of the spectral lines and FCs. This advancement has far-reaching implications across disciplines, benefiting applications in timing, sensing, resonance stabilization, spectroscopy, and quantum information processing. Optical FCs realized within micro-scale nonlinear optical resonators show promise in reducing both footprint and power consumption compared to traditional FC generators. However, challenges persist, including the costs and complexities of fabrication and experimental setup. Further, the power threshold required to generate Kerr FCs is high leading to significant thermal losses that can impact their stability and phase coherence. Integrating a control component becomes crucial to address this limitation and maintain stability.

Recent advances in micro-scale fabrication techniques have driven a significant evolution in MEMS & NEMS. These advances enable the integration of sophisticated mechanical and electrical elements into compact devices with highly flexible materials and designs. The combination of high structural quality and reduced effective mass empowers these

mechanical resonators to operate at high resonant frequencies and achieve high quality (Q) factors at ultra-low power consumption. Electrostatic MEMS & NEMS hold particular promise as FC generators due to their strong nonlinearity. Diverse methods have been employed to generate mechanical FCs in MEMS & NEMS, including parametric excitation, modal interactions within one or more structures, and external excitation of self-excited systems. All-mechanical FC generators are a natural extension of optomechanical FC generators. They exploit higher frequency modes to play the role of a so-called phononic-cavity. But the realization of multimodal mechanical FCs, akin to optical FCs, remains a challenge that we address in this work.

We engineer the modal coupling mechanisms within NEMS resonators to unleashes a spectrum of rich nonlinear features that offer an innovative solution to fundamental problems, such as quantum transduction, as it expands the bandwidth of the generated FCs by fostering a stronger energy transfer between participating modes. Further, the energy exchange between modes involved in internal resonance, where natural frequencies are integer multiples of each other ($pf_1 = qf_2$), occur at rates orders of magnitude faster than exchanges with external sources offering further stabilization to the resulting FCs.

This study presents a novel approach for the generation of mechanical soliton FCs that exploits combination internal resonance within a NEMS resonator for energy transfer between low and high frequency modes. It investigates theoretically and experimentally the conditions for generation of mechanical soliton FCs in a NEMS resonator, similar to those generated by nonlinear optical microresonators conditions. The NEMS resonator is externally excited via electrostatic forcing tuned to a higher-order superharmonic resonance of the fundamental mode. We find that this scheme enhances phononic coupling of the modes, resulting in the emergence of multi-soliton mechanical FCs characterized by a narrow pulse time-domain response.

Modal interactions arising from combination resonances within a multi-degree-of-freedom system can manifest as parametric, external, or internal resonances. Specifically, combination internal resonances unfold in systems featuring quadratic nonlinearities, where a set of modes satisfy the condition:

$$f_k \approx f_i \pm f_j \tag{4.1}$$

among their natural frequencies $f_n$. For systems featuring cubic nonlinearities, combination internal resonances may occur where:

$$\begin{aligned} f_\ell &\approx f_k \pm f_j \pm f_i \\ \text{or } \; f_k &\approx 2f_j \pm f_i \end{aligned} \tag{4.2}$$

Modal interactions are triggered when one of the internally combined modes is excited and the threshold level for energy exchange is crossed.

## 4.2 Fabrication process for the NEMS

Two nanocantilevers were fabricated for this study, differing slightly in the support part. Figure 4.3 depicts the nanocantilever with the bracket support, exhibiting superior quality factors in air, with a static pull-in voltage of around 41.5 V, compared to the standard nanocantilever shown in Figure 4.4, with a pull-in voltage of around 7.2 V. This improvement underscore the effectiveness of the bracket in minimizing energy dissipation, leading to more prolonged and stable vibrational modes. However, this disparity arises from the enhances stiffness and the induced surface tangential stress caused by the bracket part, providing the first fabricated cantilever with the advantage of supporting high electrostatic force before pull-in. This, in turn, has the potential to induce a high nonlinear electrostatic component within the motion of the NEMS device.

The steps of the fabrication process for the bracket-supported nanocantilever are shown schematically in Figure 4.2. The process uses a 3-inch silicon wafer featuring a 300 nm thick thermal oxide layer. This wafer undergoes cleaning with acetone and isopropanol before fabrication. Employing a standard lift-off technique, we create the bottom electrode and bonding pads, Figure 4.2(a). This process entails negative-tone resist application, UV lithography, and deposition of a 50 nm-thick aluminum (Al) layer through sputter deposition. The electrode, including a top metal electrode in Figure 4.2(d), enables both electrical (capacitive) and optical readouts via laser Doppler vibrometer. The wafer is then spin-coated with a 1 µm-thick sacrificial positive-tone photoresist layer and patterned using UV lithography, Figure 4.2(b).

A specialized Atmospheric-Pressure Spatial Atomic Layer Deposition (AP-SALD) system is employed to deposit the ZnO layer. Diethylzinc and water are used as zinc and oxygen precursors, delivered by nitrogen as a carrier gas. The reactor head distributes these precursors via separate outlets, ensuring precise layer formation, Figure 4.2(c). The silicon wafer, heated to 200°C, oscillates in-plane to expose its full surface to the precursor flow channels, allowing for the deposition of a 150 nm thick ZnO film in 150 oscillations. The resulting film conforms to the substrate surface, including the sides of the sacrificial photoresist layer, ensuring secure attachment of the structural layer to the anchors. AP-SALD's rapid deposition rate makes it advantageous for high-volume fabrication. Similarly, using UV lithography allows for low-cost patterning of micron-scale features.

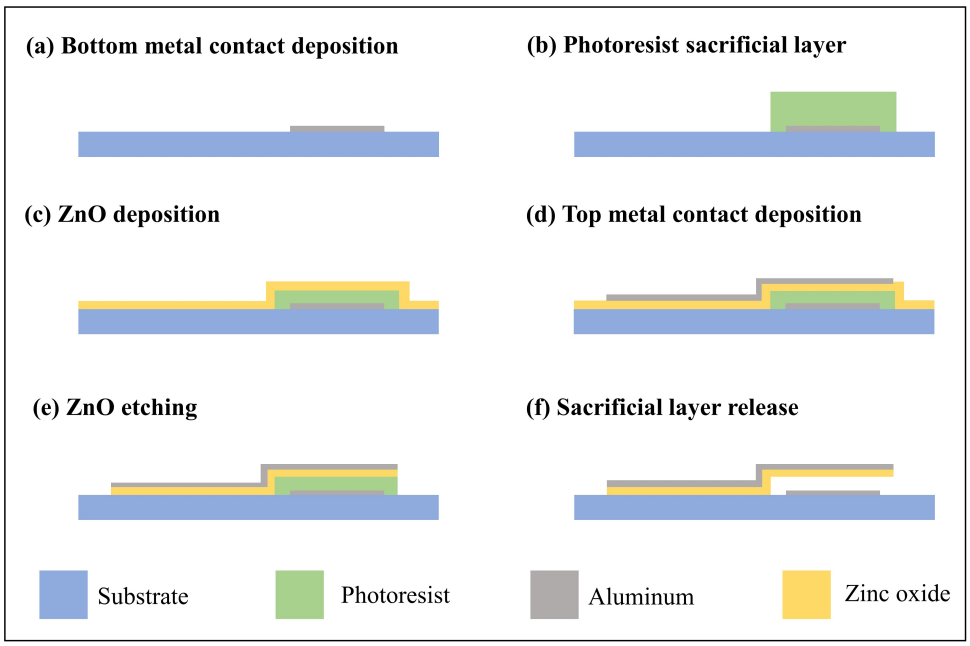



Figure 4.2: Fabrication process

A second lift-off process is employed, Figure 4.2(d), to deposit and pattern the top metal electrode. This 50 nm-thick Al layer, deposited via sputter deposition, defines the cantilever's length (50 µm) and width (10 µm). The aluminum top electrode also functions as an etch mask for reactive ion etching (RIE) of the ZnO layer, Figure 4.2(e). RIE of the ZnO layer defines the cantilever and reveals the sacrificial layer underneath it for subsequent release, Figure 4.2(f). We employ anisotropic oxygen plasma ashing to remove the sacrificial photoresist layer. The process continues until the photoresist is completely removed, as confirmed visually verified through scanning electron microscopy (SEM). The fabrication process results in the creation of a nano cantilever beam approximately 200 nm thick (composed of 150 nm ZnO and 50 nm Al layers) with a length of 50 µm and a width of 10 µm. A NEMS specimen is shown in Figure 4.3. Despite its substantial aspect ratio, the cantilever remains free-standing, a feat attributed to the conformal ZnO layer and covalent bonds generated during the AP-SALD process, ensuring robust adhesion to the substrate.

## 4.3 Comparison between the DUTs

The bracket support cantilever is shown by Figure 4.3 and the simply supported cantilever is shown by Figure 4.4.

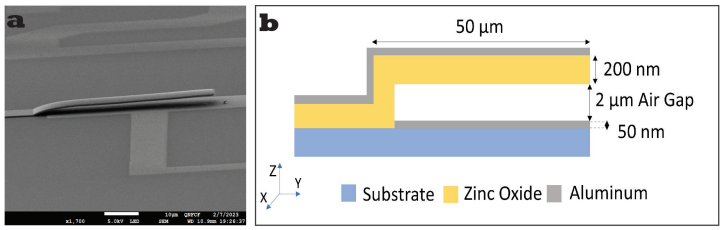



Figure 4.3: The NEMS bracket-supported cantilever; (a) an SEM image showing the beam and its anchor and (b) a schematic cross-section of the beam.

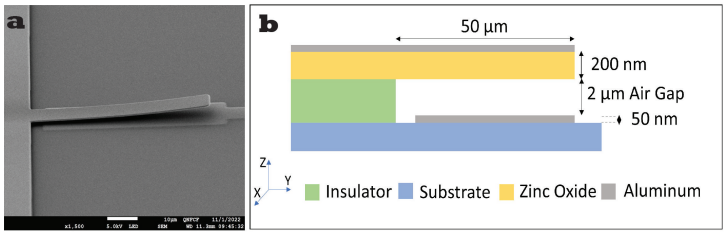



Figure 4.4: The NEMS simple-supported cantilever; (a) an SEM image showing the beam and its anchor and (b) a schematic cross-section of the beam.

The comparison of static pull in voltage between the two devices is shown by Table 4.1.

## 4.4 Optical Experimental Setup

The displacement and velocity of the beam were measured optically using a high-frequency laser Doppler vibrometer (Polytech UHF-120) via a Photo-Diode (PD) detector. The sensor was wire-bonded to a chip carrier connected to a Power Control Board and placed in custom-made test chamber equipped with an optical window, Figure 4.6. For NEMS characterization, the nanocantilever was thermally actuated using the vibrometer's laser. The laser beam was focused onto the corner of the cantilever tip through a 50x objective

Table 4.1: Comparison of pull in voltage between the two devices under test

| Natural Frequencies | Bracket Support | Simple Support |
|---|---|---|
| $f_1$ | 101 kHz | 55 kHzz |
| $f_2$ | 750 kHz | 355 kHz |
| $f_3$ | 830 kHz | 700 kHz |

lens to track oscillations of the first 5 mechanical modes (5 mW and 532 nm). The measured response was post-processed ,using a LabView software interface, in the time and frequency domains to obtain the FFT and frequency response of the NEMS. For the frequency combs generation, a drive electrical potential difference was supplied to the NEMS via a High-voltage source (High Voltage Function Generator) as a secondary external force. The laser spot was focused on the beam tip. This setup enables precise real-time analysis and visualization of the NEMS response. However, we have removed the noise floor for the FFT plots depicting mechanical frequency combs to provide a clearer view of the well-defined and discernible spectrum.

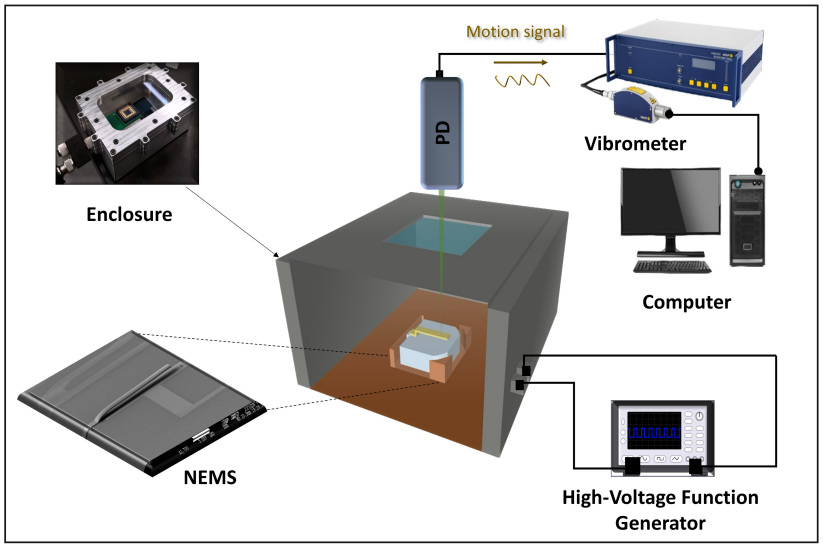



Figure 4.5: The experimental setups used for optical characterization of the DUT as well as observation of the generated frequency combs.

## 4.5 Results and discussion

The device-under-test (DUT), a nano cantilever beam, features a bracket support that allow for the application of higher electrostatic fields compared to typical nanocantilevers with a straight supported. The bracket support results in higher stiffness and a six-fold increase in pull-in voltage for the same nanocantilever dimensions. The DUT is made of a 150 nm-thick doped Zinc Oxide (ZnO) structural layer. Capacitive readout is provided by a 50 nm-thick Aluminum (Al) layer, on top of the ZnO layer, coupled to a substrate Al electrode, Figure 4.3(b). An SEM image of a 502$\mu$m-long and 10 µm-wide DUT is shown in Figure 4.3(a).

A biased harmonic potential difference:

$$v(t) = V_{\mathrm{DC}} + V_{\mathrm{AC}} \cos(2\pi f t) \tag{4.3}$$

is applied between the top and the substrate electrodes. It creates an electrostatic field within the air gap and results in an attractive force between the electrodes. The magnitude of this force is proportional to the voltage squared $v^2(t)$. It is composed of a DC component and two time-varying components $F_1$ and $F_2$ with frequencies corresponding to the first $f$ and second $2f$ harmonics of the voltage, respectively. This work exploits $F_1$ to drive the out-of-plane oscillations of the DUT.

We employ optical measurement techniques, Figure 4.10(a), to investigate the mechanical response of the NEMS. Modal analysis of the DUT was carried out via optical measurement of the tip velocity, a node-free region, in ambient air under thermomechanical noise excitation induced by the measurement laser beam (532 nm). The Fast Fourier Transform (FFT) of the measured velocity unveiled three out-of-plane bending modes and two torsional modes, Figure 4.10(b). The bending modes were observed at $f_1 = 100.02$ kHz, $f_2 = 704.19$ kH and $f_5 = 2002.02$ kHz, and the torsional modes were observed at $f_3 = 898.72$ kHz and $f_4 = 1387.06$ kHz. The quality factors of the modes in air were evaluated using the half-power bandwidth method as $Q_1 = 8.5$, $Q_2 = 18.5$, $Q_3 = 39.5$, $Q_4 = 52.2$ and $Q_5 = 73.2$. Comparing the natural frequencies of the DUT with those of a standard, straight support, nanocantilever, Figure 4.5, we found that the natural frequencies of the DUT's first two modes were double those of the standard nanocantilever confirming its higher stiffness.

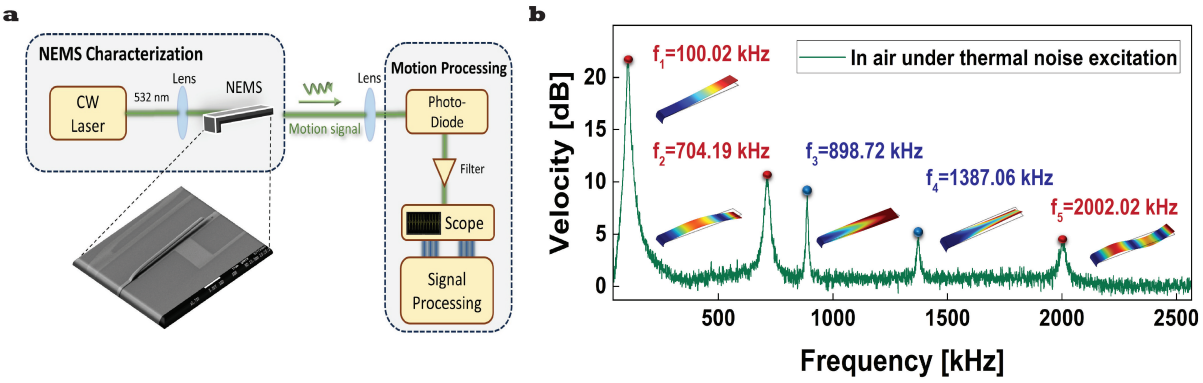



Figure 4.6: (a) Schematic of the optical measurement system used to characterize the DUT. (b) FFT of the cantilever tip velocity under thermal noise excitation.

Triggering internal resonances within the DUT requires identification of integer ratios among its modal frequencies. We found the following commensurate ratios among the first five mechanical modes:

$$f_3 \approx f_2 + 2\, f_1 \tag{4.4}$$

$$f_4 \approx 2\, f_2 \tag{4.5}$$

$$f_5 \approx f_4 + f_2 - f_1 \tag{4.6}$$

In this context, it is feasible to activate combination internal resonances involving the first five mechanical modes with the potential for higher modes to be subsequently involved. The direct excitation of one single mode triggers an indirect excitation of the mechanically coupled mode(s) when the excitation level surpasses the threshold required to initiate the energy channel between them. This principle holds true for all three internal interaction scenarios. The mere existence of a commensurable relation is insufficient to predict mode interaction through internal resonance conditions; an additional requirement is that the coupling coefficients, essential for mode interaction, must not vanish. Both criteria must be met for mode interaction to manifest within the system. The (DUT) featuring the bracket structure empowers us to apply a substantial electrostatic force, capable of inducing modal interaction in various cases, all before reaching the pull-in voltage threshold.

The dimensionless equation of motion describing the dynamics of the DUT's oscillation under transverse electrostatic forces reduces to

$$\ddot{w} + \alpha_1 \dot{w} + w'''' = F_e(w;t) + F_t(t) \tag{4.7}$$

where the overdot indicates a derivative with respect to time, the prime indicates a derivative with respect to space, $\alpha_1$ is the nondimensional viscous damping coefficient, $F_e(w;t)$ is the electrostatic force, and $F_t(t)$ is a stochastic force exerted by the thermal bath. We found that the coefficient of the geometric and inertial nonlinearities arising from the inextensibility condition $\delta_0 = (\frac{g_0}{L})^2 = 0.0016$ was negligible and, therefore, ignored them. The electrostatic force can be recast into one direct and multiple parametric excitation terms as:

$$F_e \approx \underbrace{\alpha_2 V(t)^2}_{F_e^{ext}(t)} + \underbrace{\alpha_2 V(t)^2 \left(\beta_1 w + \beta_2 w^2 + \beta_3 w^3 + \beta_4 w^4 + \text{ H.O.T }\right)}_{F_e^{par}(w;t)} \tag{4.8}$$

where $\beta_1$, $\beta 2$, and $\beta 3$ are constants describing the time invariant components of the electrostatic field.

Our actuation scheme aims to excite a large number of vibration modes. It achieves that by sequential energy transfer among a set of modes. Direct excitation actuates a low frequency (LF) mode. Internal combination resonance transfers energy from that mode to a set of intermediate frequency (IF) modes. In turn, parametric excitation transfers and amplifies energy passage from those modes to a set of high frequency (HF) modes. To observe the interaction among the lowest five out-of-plane bending modes we rewrite the transverse displacement as a linear combination of the lowest five eigenfunctions $\phi_i(s)$ of a straight undamped cantilever beam:

$$w(s;t) = \sum_{i=1}^{5} q_i(t)\phi_i(s)$$

where $q_i(t)$ is a modal coordinate. This Galerkin expansion is used in Eq. (4.7) to reduce it to a set of five nonlinearly coupled ordinary differential equations.

The experimental setup is shown in Figure 3(a) was used to obtain the frequency response of the NEMS in air under different excitation levels at the superharmonic resonance of order 10 of the lowest mode by setting the excitation frequency to $f = f_1/10 = 10.005\,\text{kHz}$. In each case, the response was obtained by evaluating the FFT of the measured beam tip velocity.

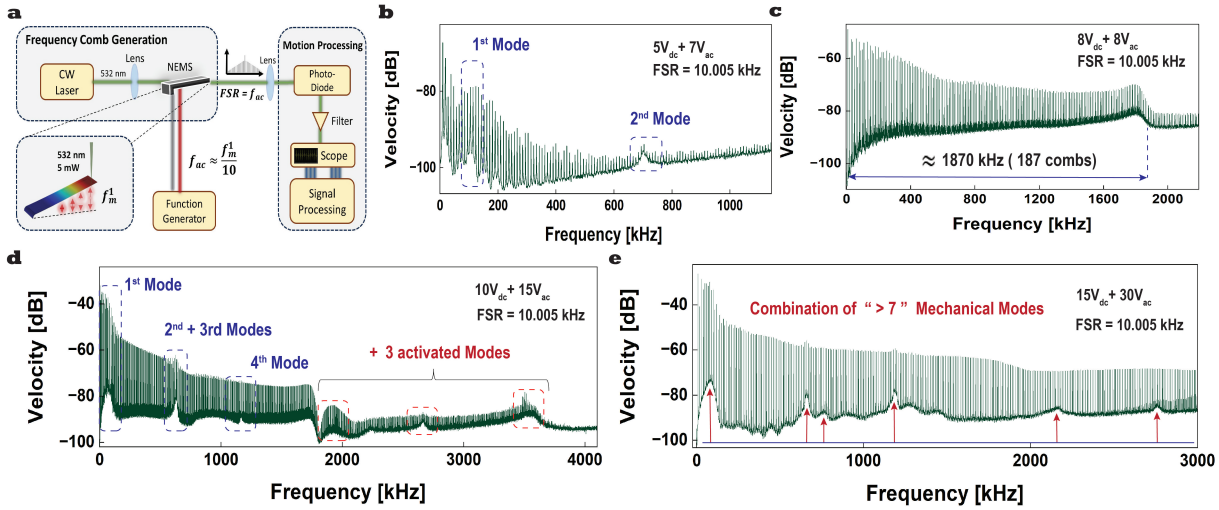



Figure 4.7: (a) Schematic of the used experimental setup and FFT response for difference waveform voltages (b) $V_{\mathrm{DC}} = 5V$, $V_{\mathrm{AC}} = 7V$ (c) $V_{\mathrm{DC}} = V_{\mathrm{AC}} = 8V$ (d) $V_{\mathrm{DC}} = 10V$ and $V_{\mathrm{AC}} = 15V$ and (e) $V_{\mathrm{DC}} = 15V$ and $V_{\mathrm{AC}} = 30V$

At the lowest excitation level of $V_{\mathrm{DC}} = 5V$, $V_{\mathrm{AC}} = 7V$, the NEMS response, Figure 4.11(b), exhibits a uniformly spaced Frequency Comb (FC) covering the spectrum up to 1 MHz. The spectral lines correspond to harmonics of the excitation frequency $f$ and a Free Spectral Range (FSR) of $f = f_1/10$. This power distribution is formed by the superharmonic resonance of order 10 of the first bending mode at $f_1$ and its higher harmonics. Higher harmonics of $f$ falling within the half-power bandwidth of the second mode are amplified by that mode, thereby allowing the FC to extend well beyond $f_1$.

Increasing the excitation level to $V_{\mathrm{DC}} = V_{\mathrm{AC}} = 8V$, results in a wider FC extending up to 1.87 MHz, Figure 4.11(c), with FSR $= f$. The amplitudes of the spectral lines forming the FC drop slowly and uniformly throughout a compact section of the spectrum (the FC) due to the activation of interactions among the first four vibration modes. Unlike the previous case, a higher level of direct excitation to the first mode activates the second and third modes trough modal interaction as per Eq. (4.4). In turn, the second mode activates the fourth mode through modal interaction as per Eq. (4.5). These interactions allow the FC to occupy a wider spectrum at higher amplitude. The energy exchange among the modes also underlay the order represented by the gradual and uniform drop in the power of those amplitudes.

Increasing of the excitation level further to $V_{\mathrm{DC}} = 10V$ and $V_{\mathrm{AC}} = 15V$, increases the amplitudes of the FC observed above and introduces a second FC comprised of compact

section of the spectrum extending from 1.87 MHz to 3.6 MHz, Figure 4.11(d). Both FCs share the same $FSR = f$. A vibration node separates their domains. The second FC appears due to the activation of the fifth mode at $f_5$ via interaction with the first, second, and fourth modes, as per Eq. (4.6). It encompasses two higher modes including a mode involved in an interaction with the second and fifth modes at $f_6 = f_2 + f_5 = 2.712$ MHz. The highest mode in the second FC appears to simply amplify the harmonics of $f$ rather than being involved in energy exchange of the other modes.

At the highest excitation level $V_{\text{DC}} = 15V$ and $V_{\text{AC}} = 30V$, the node disappears and the two FCs described above merge into a single FC, Figure 4.11(e), comprised of more than 300 combs with the same $FSR = f$ and covering a frequency spectrum in excess of 3 MHz. Conducting the same experiment on other DUTs with thicker aluminum electrodes, resulting in destruction of the modal interactions described above, produces FCs similar to that seen in Figure 4.11(b) that cover a limited range of the frequency spectrum and lack uniformity in power distribution due to the absence of the energy exchange facilitated by the internal combination resonances. This was true up to the highest excitation level of $V_{\text{DC}} = 15V$ and $V_{\text{AC}} = 30V$.

A soliton FC centered at 0 Hz was observed under a higher excitation level than those described above. We generated solitons with varying FSRs under an excitation of $V_{DC} = 20V$ and $V_{AC} = 35V$, Figure 4.12. A complex FFT of the NEMS response to a superharmonic resonance of order 10 ($f = 10.005$ kHz), Figure 4.12(d), reveals a soliton state-I spanning 8 MHz and comprised of more than over 800 combs with FSR= $f$. A slight reduction in the excitation frequency by 5 Hz to FSR= $f = 10.0$ kHz initiates the formation of lobes within the soliton, Figure 4.12(f). It also increases the soliton sizefrom 800 to 820 lines, indicating of increased energy exchange and enhanced modal interaction. A further another 5 Hzto FSR= $f = 10.005$ kHz yields a soliton state-II with discernible small lobes, Figure 4.12(a). Incrementally decreasing the excitation frequency by steps of 10 Hz generates state-II soliton FCs with larger lobe sizes, Figures 4.12(a)-(c).

Moreover, experimentation at $f = f_1/20 = 5$ kHz, employing the same waveform ($V_{DC} = 20V$ and $V_{AC} = 35V$) (Figure 4.12(d)), generates soliton state I covering a narrower frequency range compared to the former case. This underscores the significance of exciting with lower frequencies in facilitating internal modal interaction. Ensuring higher harmonics of the excitation fall within the half bandwidth of the targeted mechanical mode that will be as a result activated.

Expanding the frequency range, Figure 4.13(a) and (c) reveals a multi-soliton FC spectrum, covering 15 MHz and yielding around 3000 FCs. This expansion underscores the involvement of higher-order mechanical modes in multi-soliton formation. Numerical simu-

lation,Figure 4.13(b) and (d), validates the observed DUT response, validating the creation of multi-solitons in both states I and II with a reduced FC number due to the consideration of only 5 bending modes.

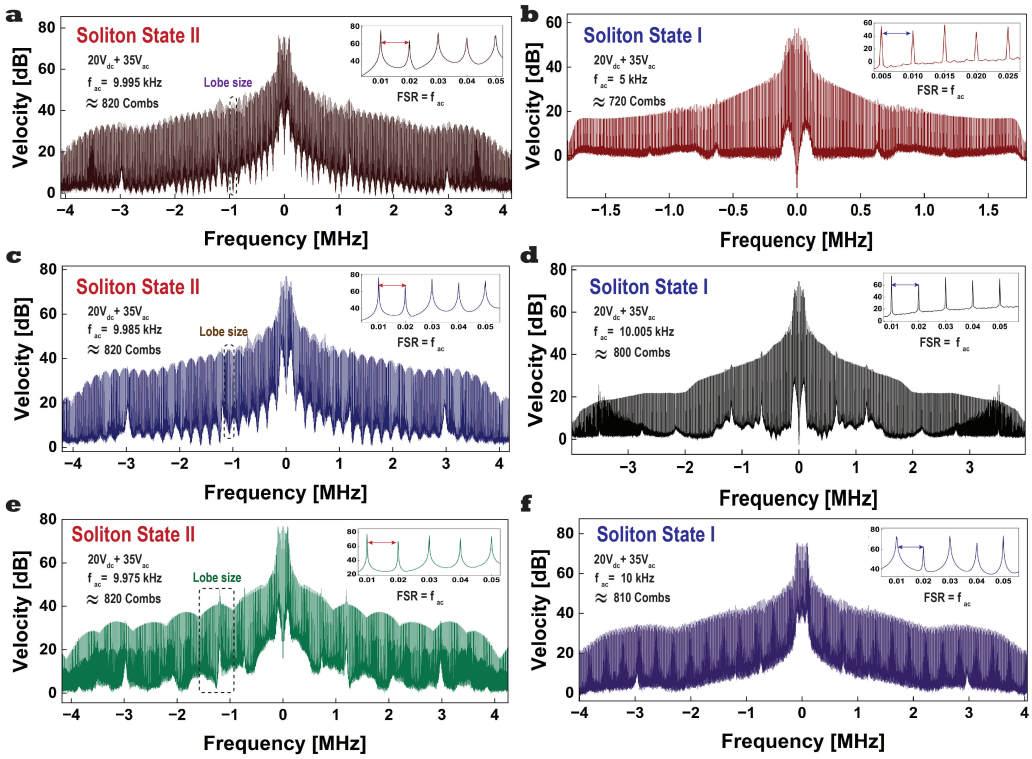



Figure 4.8: Complex FFT for the DUT velocity response for state II soliton (a), (c) and (e) and Soliton state I (b), (d) and (f)

We compare in Table 4.2 our FC to other phononic FCs realized recently. The comparison underscores the significance of internal combination resonance in terms of power efficiency, simplicity, and the number of realized teeth across the comb, two orders of magnitude higher than all others reported in the literature to date. We note that operating our frequency comb generator in a vacuum, like those reported here, will result in even wider and more powerful frequency combs. The strength of the generated FCs is dependent on the activation of the internal modal interaction and the resulting energy exchange between the mechanical modes.

Table 4.2: Comparison of FCs in NEMS/MEMS

| Material | Pressure | Base Frequency | FSR | # of Combs |
|---|---|---|---|---|
| ZnO[ this work] | Ambient | 101.1kHz | 10kHz | 3000 |
| $Si_3$ $N_4$[64] | $< 10^{-5}$ mbar | 118kHz | 118kHz | 35 |
| SiN[114] | $< 10^{-4}$ mbar | 6.52MHz | 1.1kHz | 12 |
| Graphene [115] | $< 10^{-2}$ mbar | 2.87MHz | 28.7kHz | 16 |
| $MoS_2$[116] | $2 \times 10^{-2}$mbar | 24MHz | 26.45kHz | 15 |
| Si[117] | High vacuum | 26kHz | $0.8 - 2.6$kHz | 25 |
| Si[118] | 70 mbar | 417kHz | 0.103kHz | 27 |
| AIN/Si[113] | – | 3.86MHz | 2.6kHz | 9 |

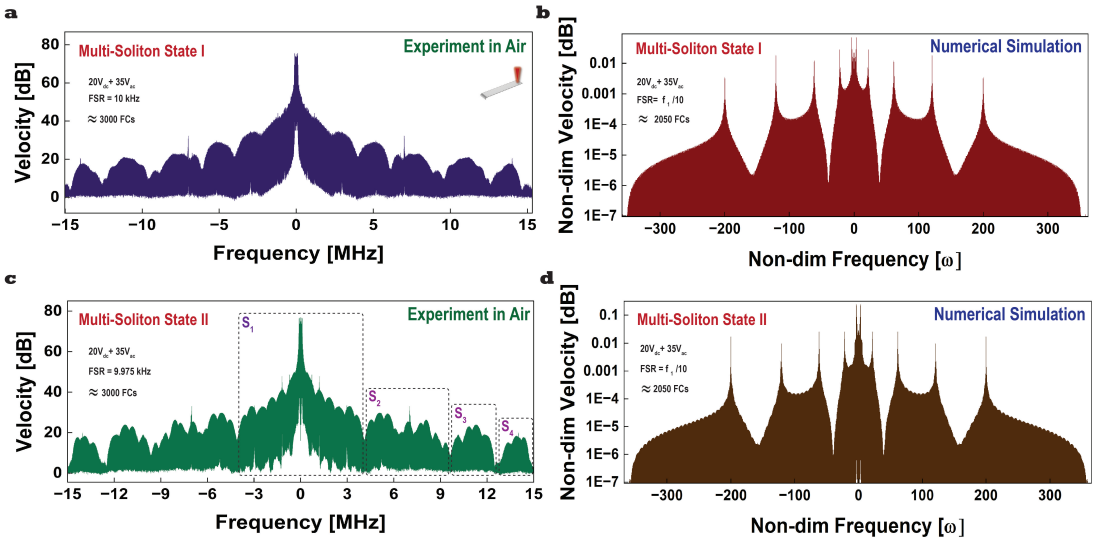



Figure 4.9: FFT showing multi soliton response for states I and II from (a) and (c) Experimental results and (b) and (d)Numerical simulation

We investigate the frequency stability and phase coherence of the generated FCs. The

precision of mechanical wave packet generators relies heavily on stable frequency references. Figure 4.14 showcases the time-domain response of the NEMS for various voltage waveforms while maintaining the same excitation frequency discussed earlier in Figure 3. Notably, the highest excitation level yields a pulse train representing the NEMS mechanical response, a result of internal modal interaction generating higher harmonics. As the force excitation level increases, a discernible evolution unfolds in the velocity amplitude and the temporal response shape, progressively transitioning into a more periodic pattern until it culminates in a distinctive pulse train shape. Notably, during the final excitation with the highest levels ($V_{\mathrm{DC}} = 15V$ and $V_{\mathrm{AC}} = 30V$), the time-domain response reveals a unique pulse train, representing the mechanical response of the NEMS, where the period (T) precisely equals 0.1 ms, corresponding to an FSR1 of 10 kHz. Upon closer examination of the last time-domain response, we identify a soliton-like shape, as depicted in Figure 4.14(d). This pulse train's emergence stems from the generation of an extensive array of higher harmonics of the excitation frequency, originating from internal modal interaction. Numerical simulation results in Figure 4.15(e) replicate the same time-domain response shape as Figure 4.14(c), albeit unable to reach the pulse train shape due to the imposed pull-in voltage.

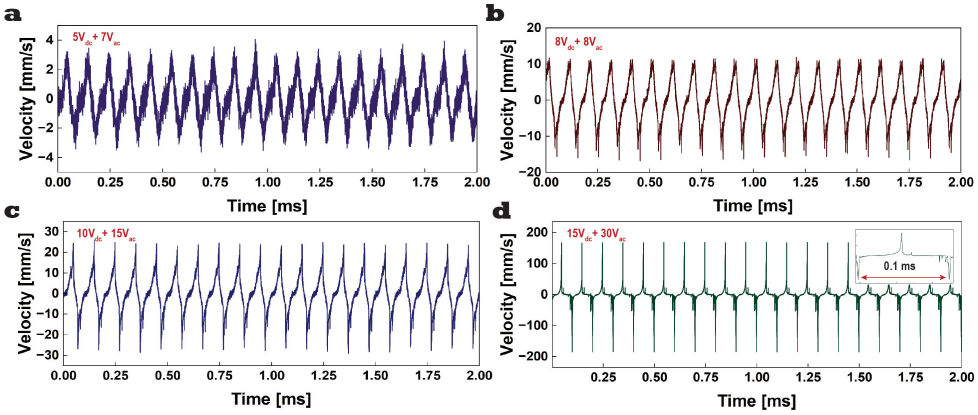



Figure 4.10: Time domain response for different waveforms and same excitation frequency.

Maintaining the highest excitation level, we further explore varying excitation frequencies to demonstrate the system's ability to sustain consistent time-domain responses across different cases, Figure 4.15. The escalating frequency, indicative of exciting higher-order super harmonics, amplifies the velocity amplitude significantly. This increase, ranging from 103 mm/s for the super harmonic of order 10 to 516 mm/s for the case of the super harmonic of order 2, signifies a more distributed energy as the system approaches the first mechanical mode.

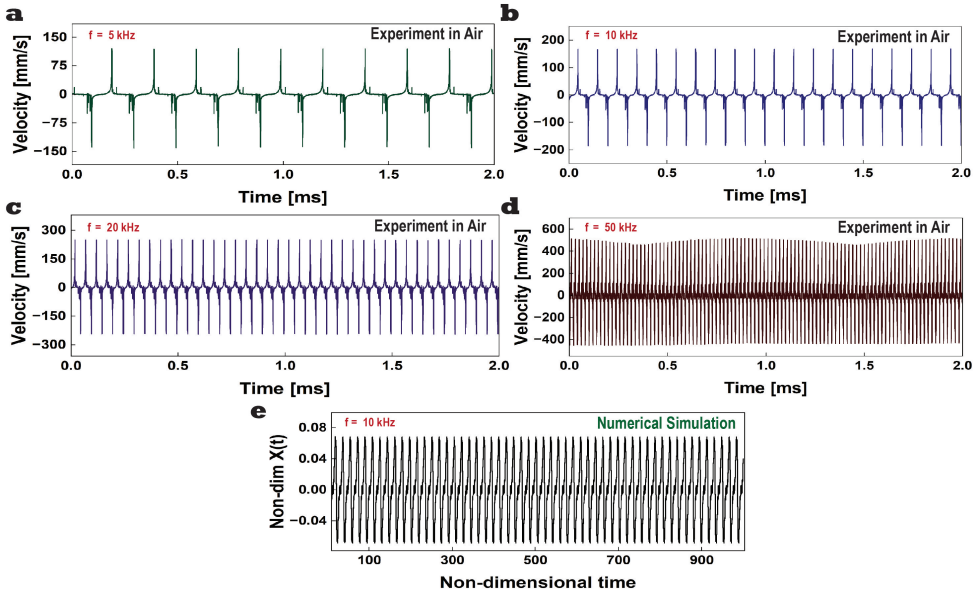



Figure 4.11: Time domain response for same voltage waveforms and different excitation frequency (a,b,c and d) Experimental results and (e) numerical simulation.

## 4.6 Conclusion

In conclusion, this study has successfully demonstrated a novel and effective technique for generating mechanical soliton FCs via internal modal interactions across a broad spectrum of mechanical modes, from low to high frequency ranges. Leveraging an electrostatic NEMS as a platform, we demonstrated the capability to produce multi-soliton FCs operating within the MHz frequency range, with kHz-level spacing facilitated by a highly nonlinear electrostatic system that enhances internal modal interaction. A nanobeam was subjected to electrostatic actuation to precisely excite the superharmonic of-order-ten of the first bending mode. High excitation levels result in the creation of stable and resilient multi-mechanical soliton frequency combs, perfectly aligned with the electric excitation frequency spacing. Moreover, by slightly adjusting the frequency, we can generate soliton states I and II with varying lobe sizes. This novel architecture of soliton frequency comb generators holds immense promise in the fields of metrology, quantum computing, and notably, sensing through spectroscopy by leveraging the concept of dual-frequency combs.

# Chapter 5

# Conclusions and Future Work

## 5.1 Summary of Contributions

Throughout this thesis, we harnessed the MOF-CVD approach to sensitize silicon cantilevers with a MOF as a sensing layer for VOC detection, comparing its performance with cantilevers coated with a ZnO thin film. Our investigation unveiled the superior sensitivity of the MOF-coated sensor to VOCs, achieving LODs in the ppb range, attributed to the high porosity and large surface area of MAF-6. Further sensitivity enhancements are attainable by reducing the microcantilever dimensions and optimizing the actuation and read-out scheme. Remarkably, this technique is solvent-free and compatible with conventional microfabrication processes, positioning it as a promising candidate for highly sensitive gas sensors.

In addition, we introduced novel noise-driven ZnO NEMS sensors capable of achieving sensitivity comparable to MOF-coated MEMS sensors due to their high inertial sensitivity. These sensors offer autonomy and low power consumption, setting the stage for leveraging these advantages by transforming a portion of the structural ZnO into MOFs via a similar CVD process.

Moreover, our research contributed to advancing microfabrication processes for free-standing metal oxide cantilevers, effectively mitigating associated challenges. By leveraging the oxide layer as both the structural and gas-sensitive receptor layer, we minimized interlayer damping effects. The reduction in cantilever mass through a thin oxide layer deposited via the AP-SALD technique significantly enhanced the cantilevers' quality factor under ambient conditions.

Furthermore, we successfully developed an energy-efficient technique for generating electro-mechanical frequency combs via modal interactions between electrical and mechanical resonators. Using an electrostatic NEMS platform, we demonstrated the generation of multi-soliton frequency combs across a broad frequency spectrum. This innovative technique holds potential applications in metrology, quantum computing, and sensing through spectroscopy by leveraging the concept of dual-frequency combs.

Finally, our thesis presents a novel and effective approach for generating mechanical soliton FCs across a broad spectrum of mechanical modes. Leveraging an electrostatic NEMS platform, we demonstrated the production of multi-soliton FCs operating within the MHz frequency range. This innovative soliton frequency comb architecture holds immense potential in various fields, including metrology, quantum computing, and sensing through spectroscopy.

## 5.2 Future Work

Our future research endeavors will focus on several key areas:

Firstly, we plan to transition the electrostatic ZnO NEMS sensors to MOF NEMS sensors to enhance sensitivity and selectivity for VOCs. This transition holds promise for improving the performance of our sensors in detecting volatile organic compounds.

Secondly, we aim to explore the potential applications of soliton frequency combs generated for gas sensing purposes. Leveraging the inherent sensitivity of the ZnO material in the sensor structure, we anticipate achieving highly efficient sensing mechanisms. By utilizing soliton frequency combs as a sensitive metric, we expect to enhance the detection capabilities of our gas sensors significantly.

Furthermore, we intend to investigate the optical response of the generated frequency combs. Modulation by mechanical responses can potentially yield dense optomechanical responses, opening up avenues for novel sensing applications. This exploration into optomechanical responses promises to provide valuable insights into the behavior and characteristics of our frequency combs, further enhancing their utility in gas sensing and beyond.

# Letter of Copyright Permission



4/18/24, 3:31 PM Rightslink® by Copyright Clearance Center

CCC RightsLink

Sign in/Register

Noise-Driven MOF-Coated NEMS Sensors

IEEE Requesting permission to reuse content from an IEEE publication

**Conference Proceedings:**
2023 IEEE 22nd International Conference on Micro and Nanotechnology for Power Generation and Energy Conversion Applications (PowerMEMS)

**Author:** Hamza Mouharrar

**Publisher:** IEEE

**Date:** 11 December 2023

*Copyright © 2023, IEEE*

Thesis / Dissertation Reuse

**The IEEE does not require individuals working on a thesis to obtain a formal reuse license, however, you may print out this statement to be used as a permission grant:**

*Requirements to be followed when using any portion (e.g., figure, graph, table, or textual material) of an IEEE copyrighted paper in a thesis:*

1) In the case of textual material (e.g., using short quotes or referring to the work within these papers) users must give full credit to the original source (author, paper, publication) followed by the IEEE copyright line © 2011 IEEE.
2) In the case of illustrations or tabular material, we require that the copyright line © [Year of original publication] IEEE appear prominently with each reprinted figure and/or table.
3) If a substantial portion of the original paper is to be used, and if you are not the senior author, also obtain the senior author's approval.

*Requirements to be followed when using an entire IEEE copyrighted paper in a thesis:*

1) The following IEEE copyright/ credit notice should be placed prominently in the references: © [year of original publication] IEEE. Reprinted, with permission, from [author names, paper title, IEEE publication title, and month/year of publication]
2) Only the accepted version of an IEEE copyrighted paper can be used when posting the paper or your thesis on-line.
3) In placing the thesis on the author's university website, please display the following message in a prominent place on the website: In reference to IEEE copyrighted material which is used with permission in this thesis, the IEEE does not endorse any of [university/educational entity's name goes here]'s products or services. Internal or personal use of this material is permitted. If interested in reprinting/republishing IEEE copyrighted material for advertising or promotional purposes or for creating new collective works for resale or redistribution, please go to http://www.ieee.org/publications_standards/publications/rights/rights_link.html to learn how to obtain a License from RightsLink.

If applicable, University Microfilms and/or ProQuest Library, or the Archives of Canada may supply single copies of the dissertation.

BACK CLOSE WINDOW

© 2024 Copyright - All Rights Reserved | Copyright Clearance Center, Inc. | Privacy statement | Data Security and Privacy | For California Residents | Terms and ConditionsComments? We would like to hear from you. E-mail us at customercare@copyright.com

# References


[1] S. D. Senturia, *Microsystem design*. Springer Science & Business Media, 2005.

[2] A. Cowen, G. Hames, D. Monk, S. Wilcenski, and B. Hardy, "Soimumps design handbook," *Memscap Inc*, pp. 2002–2011, 2011.

[3] D. Koester, A. Cowen, R. Mahadevan, M. Stonefield, and B. Hardy, "Polymumps design handbook," *MEMSCAP Inc*, 2003.

[4] D. C. Abeysinghe, S. Dasgupta, J. T. Boyd, and H. E. Jackson, "A novel mems pressure sensor fabricated on an optical fiber," *IEEE photonics technology letters*, vol. 13, no. 9, pp. 993–995, 2001.

[5] C. M. Jha, G. Bahl, R. Melamud, S. Chandorkar, M. Hopcroft, B. Kim, M. Agarwal, J. Salvia, H. Mehta, and T. Kenny, *CMOS-compatible dual-resonator MEMS temperature sensor with milli-degree accuracy*. IEEE, 2007.

[6] M. Al-Ghamdi, M. Khater, K. Stewart, A. Alneamy, E. M. Abdel-Rahman, and A. Penlidis, "Dynamic bifurcation mems gas sensors," *Journal of Micromechanics and Microengineering*, vol. 29, no. 1, p. 015005, 2018.

[7] M. I. A. Asri, M. N. Hasan, M. R. A. Fuaad, Y. M. Yunos, and M. S. M. Ali, "Mems gas sensors: A review," *IEEE Sensors Journal*, vol. 21, no. 17, pp. 18381–18397, 2021.

[8] J.-O. Dennis, A.-Y. Ahmed, and M.-H. Khir, "Fabrication and characterization of a cmos-mems humidity sensor," *Sensors*, vol. 15, no. 7, pp. 16674–16687, 2015.

[9] M. Haque and M. Saif, "Application of mems force sensors for in situ mechanical characterization of nano-scale thin films in sem and tem," *Sensors and Actuators A: Physical*, vol. 97, pp. 239–245, 2002.

[10] S. Luczak, W. Oleksiuk, and M. Bodnicki, "Sensing tilt with mems accelerometers," *IEEE Sensors Journal*, vol. 6, no. 6, pp. 1669–1675, 2006.

[11] Q. Zheng, L. Dong, D. H. Lee, and Z. Gao, "Active disturbance rejection control for mems gyroscopes," in *2008 American control conference*, pp. 4425–4430, IEEE, 2008.

[12] P. R. Patterson, D. Hah, M. Fujino, W. Piyawattanametha, and M. C. Wu, "Scanning micromirrors: An overview," *Optomechatronic Micro/Nano Components, Devices, and Systems*, vol. 5604, pp. 195–207, 2004.

[13] M. Ruan, J. Shen, and C. Wheeler, "Latching microelectromagnetic relays," *Sensors and Actuators A: Physical*, vol. 91, no. 3, pp. 346–350, 2001.

[14] S. Patton and J. Zabinski, "Fundamental studies of au contacts in mems rf switches," *Tribology Letters*, vol. 18, pp. 215–230, 2005.

[15] A. M. Alneamy, M. E. Khater, A. K. Abdel-Aziz, G. R. Heppler, and E. M. Abdel-Rahman, "Electrostatic arch micro-tweezers," *International Journal of Non-Linear Mechanics*, vol. 118, p. 103298, 2020.

[16] K. Frank, M. J. Vera-Nadales, P. Robertson, and M. Angermann, "Reliable real-time recognition of motion related human activities using mems inertial sensors," in *Proceedings of the 23rd international technical meeting of the satellite division of the institute of navigation (ION GNSS 2010)*, pp. 2919–2932, 2010.

[17] M. Khater, M. Al-Ghamdi, S. Park, K. Stewart, E. Abdel-Rahman, A. Penlidis, A. Nayfeh, A. Abdel-Aziz, and M. Basha, "Binary mems gas sensors," *Journal of Micromechanics and Microengineering*, vol. 24, no. 6, p. 065007, 2014.

[18] S.-E. Zhu, M. Krishna Ghatkesar, C. Zhang, and G. Janssen, "Graphene based piezoresistive pressure sensor," *Applied Physics Letters*, vol. 102, no. 16, 2013.

[19] S. Tadigadapa and K. Mateti, "Piezoelectric mems sensors: state-of-the-art and perspectives," *Measurement Science and technology*, vol. 20, no. 9, p. 092001, 2009.

[20] S. Kocer, L. Mukhangaliyeva, R. Saritas, A. Gulsaran, A. Elhady, K. Bell, A. Kamel, M. Basha, T. Das, M. Kayaharman, *et al.*, "Resonant varifocal mems mirror," in *2022 IEEE 35th International Conference on Micro Electro Mechanical Systems Conference (MEMS)*, pp. 963–966, IEEE, 2022.

[21] N. J. Conway, Z. J. Traina, and S.-G. Kim, "A strain amplifying piezoelectric mems actuator," *Journal of Micromechanics and Microengineering*, vol. 17, no. 4, p. 781, 2007.

[22] X. Lv, W. Wei, X. Mao, Y. Chen, J. Yang, and F. Yang, "A novel mems electromagnetic actuator with large displacement," *Sensors and Actuators A: Physical*, vol. 221, pp. 22–28, 2015.

[23] O. Ulkir, "Design and fabrication of an electrothermal mems micro-actuator with 3d printing technology," *Materials Research Express*, vol. 7, no. 7, p. 075015, 2020.

[24] R. Bogue, "Towards the trillion sensors market," *Sensor review*, vol. 34, no. 2, pp. 137–142, 2014.

[25] Y. Luo, M. R. Abidian, J.-H. Ahn, D. Akinwande, A. M. Andrews, M. Antonietti, Z. Bao, M. Berggren, C. A. Berkey, C. J. Bettinger, *et al.*, "Technology roadmap for flexible sensors," *ACS nano*, vol. 17, no. 6, pp. 5211–5295, 2023.

[26] J. B. Gomes, J. J. Rodrigues, R. A. Rabêlo, N. Kumar, and S. Kozlov, "Iot-enabled gas sensors: Technologies, applications, and opportunities," *Journal of Sensor and Actuator Networks*, vol. 8, no. 4, p. 57, 2019.

[27] M. V. Nikolic, V. Milovanovic, Z. Z. Vasiljevic, and Z. Stamenkovic, "Semiconductor gas sensors: Materials, technology, design, and application," *Sensors*, vol. 20, no. 22, p. 6694, 2020.

[28] B. Ilic, Y. Yang, and H. G. Craighead, "Virus detection using nanoelectromechanical devices," *Applied physics letters*, vol. 85, no. 13, pp. 2604–2606, 2004.

[29] A. Zribi, A. Knobloch, W.-C. Tian, and S. Goodwin, "Micromachined resonant multiple gas sensor," *Sensors and Actuators A: Physical*, vol. 122, no. 1, pp. 31–38, 2005.

[30] K. Park, N. Kim, D. T. Morisette, N. Aluru, and R. Bashir, "Resonant mems mass sensors for measurement of microdroplet evaporation," *Journal of Microelectromechanical Systems*, vol. 21, no. 3, pp. 702–711, 2012.

[31] J. H. Pikul, P. Graf, S. Mishra, K. Barton, Y.-K. Kim, J. A. Rogers, A. Alleyne, P. M. Ferreira, and W. P. King, "High precision electrohydrodynamic printing of polymer onto microcantilever sensors," *IEEE Sensors Journal*, vol. 11, no. 10, pp. 2246–2253, 2011.

[32] P. G. Datskos and I. Sauers, "Detection of 2-mercaptoethanol using gold-coated micromachined cantilevers," *Sensors and Actuators B: Chemical*, vol. 61, no. 1-3, pp. 75–82, 1999.

[33] S. Dohn, R. Sandberg, W. Svendsen, and A. Boisen, "Enhanced functionality of cantilever based mass sensors using higher modes," *Applied physics letters*, vol. 86, no. 23, 2005.

[34] N. Lobontiu, I. Lupea, R. Ilic, and H. G. Craighead, "Modeling, design, and characterization of multisegment cantilevers for resonant mass detection," *Journal of Applied Physics*, vol. 103, no. 6, 2008.

[35] H. Xie, J. Vitard, S. Haliyo, and S. Régnier, "Enhanced sensitivity of mass detection using the first torsional mode of microcantilevers," in *2007 International Conference on Mechatronics and Automation*, pp. 39–44, IEEE, 2007.

[36] S. Dohn, O. Hansen, and A. Boisen, "Cantilever based mass sensor with hard contact readout," *Applied Physics Letters*, vol. 88, no. 26, 2006.

[37] W.-T. S. Chen, K. M. Stewart, C. K. Yang, R. R. Mansour, J. Carroll, and A. Penlidis, "Wearable rf sensor array implementing coupling-matrix readout extraction technique," *IEEE Transactions on Microwave Theory and Techniques*, vol. 63, no. 12, pp. 4157–4168, 2015.

[38] W. Chen, K. Stewart, R. Mansour, and A. Penlidis, "Novel undercoupled radio-frequency (rf) resonant sensor for gaseous ethanol and interferents detection," *Sensors and Actuators A: Physical*, vol. 230, pp. 63–73, 2015.

[39] H. Jensenius, J. Thaysen, A. A. Rasmussen, L. H. Veje, O. Hansen, and A. Boisen, "A microcantilever-based alcohol vapor sensor-application and response model," *Applied Physics Letters*, vol. 76, no. 18, pp. 2615–2617, 2000.

[40] P. Li and X. Li, "A single-sided micromachined piezoresistive sio2 cantilever sensor for ultra-sensitive detection of gaseous chemicals," *Journal of Micromechanics and Microengineering*, vol. 16, no. 12, p. 2539, 2006.

[41] W. Zhu, J. S. Park, J. L. Sessler, and A. Gaitas, "A colorimetric receptor combined with a microcantilever sensor for explosive vapor detection," *Applied Physics Letters*, vol. 98, no. 12, 2011.

[42] D. Lange, C. Hagleitner, A. Hierlemann, O. Brand, and H. Baltes, "Complementary metal oxide semiconductor cantilever arrays on a single chip: mass-sensitive detection of volatile organic compounds," *Analytical Chemistry*, vol. 74, no. 13, pp. 3084–3095, 2002.

[43] U. Sampath, S. M. Heinrich, F. Josse, F. Lochon, I. Dufour, and D. Rebiere, "Study of viscoelastic effect on the frequency shift of microcantilever chemical sensors," *IEEE transactions on ultrasonics, ferroelectrics, and frequency control*, vol. 53, no. 11, pp. 2166–2173, 2006.

[44] I. Dufour, F. Josse, S. M. Heinrich, C. Lucat, C. Ayela, F. Ménil, and O. Brand, "Unconventional uses of microcantilevers as chemical sensors in gas and liquid media," *Sensors and Actuators B: Chemical*, vol. 170, pp. 115–121, 2012.

[45] L. Sharos, A. Raman, S. Crittenden, and R. Reifenberger, "Enhanced mass sensing using torsional and lateral resonances in microcantilevers," *Applied Physics Letters*, vol. 84, no. 23, pp. 4638–4640, 2004.

[46] I. Dufour, S. M. Heinrich, and F. Josse, "Strong-axis bending mode vibrations for resonant microcantilever (bio) chemical sensors in gas or liquid phase," in *Proceedings of the 2004 IEEE International Frequency Control Symposium and Exposition, 2004.*, pp. 193–199, IEEE, 2004.

[47] P. S. Waggoner and H. G. Craighead, "Micro-and nanomechanical sensors for environmental, chemical, and biological detection," *Lab on a Chip*, vol. 7, no. 10, pp. 1238–1255, 2007.

[48] H. Debéda, R. Lakhmi, C. Lucat, and I. Dufour, "Use of the longitudinal mode of screen-printed piezoelectric cantilevers coated with peut for toluene detection: Comparison with silicon cantilevers," *Sensors and Actuators B: Chemical*, vol. 187, pp. 198–203, 2013.

[49] A. M. Bouchaala and M. I. Younis, "A model of electrostatically actuated mems and carbon nanotubes resonators for biological mass detection," in *Design and Modeling of Mechanical Systems-II: Proceedings of the Sixth Conference on Design and Modeling of Mechanical Systems, CMSM'2015, March 23-25, Hammamet, Tunisia*, pp. 501–512, Springer, 2015.

[50] M. I. Younis and F. Alsaleem, "Exploration of new concepts for mass detection in electrostatically-actuated structures based on nonlinear phenomena," *J. Comput. Nonlinear Dynam.*, 2009.

[51] A. Bouchaala, A. H. Nayfeh, and M. I. Younis, "Frequency shifts of micro and nano cantilever beam resonators due to added masses," *Journal of Dynamic Systems, Measurement, and Control*, vol. 138, no. 9, p. 091002, 2016.

[52] L. L. Li, E. L. Holthoff, L. A. Shaw, C. B. Burgner, and K. L. Turner, "Noise squeezing controlled parametric bifurcation tracking of mip-coated microbeam mems sensor for tnt explosive gas sensing," *Journal of Microelectromechanical Systems*, vol. 23, no. 5, pp. 1228–1236, 2014.

[53] N. Goel, K. Kunal, A. Kushwaha, and M. Kumar, "Metal oxide semiconductors for gas sensing," *Engineering Reports*, vol. 5, no. 6, p. e12604, 2023.

[54] G. Neri, "First fifty years of chemoresistive gas sensors," *Chemosensors*, vol. 3, no. 1, pp. 1–20, 2015.

[55] D. Nunes, A. Pimentel, A. Gonçalves, S. Pereira, R. Branquinho, P. Barquinha, E. Fortunato, and R. Martins, "Metal oxide nanostructures for sensor applications," *Semiconductor Science and Technology*, vol. 34, no. 4, p. 043001, 2019.

[56] S.-Y. Jeong, J.-S. Kim, and J.-H. Lee, "Rational design of semiconductor-based chemiresistors and their libraries for next-generation artificial olfaction," *Advanced Materials*, vol. 32, no. 51, p. 2002075, 2020.

[57] A. Marikutsa, M. Rumyantseva, E. A. Konstantinova, and A. Gaskov, "The key role of active sites in the development of selective metal oxide sensor materials," *Sensors*, vol. 21, no. 7, p. 2554, 2021.

[58] C.-N. Wang, Y.-L. Li, F.-L. Gong, Y.-H. Zhang, S.-M. Fang, and H.-L. Zhang, "Advances in doped zno nanostructures for gas sensor," *The Chemical Record*, vol. 20, no. 12, pp. 1553–1567, 2020.

[59] N. Kilinc, O. Cakmak, A. Kosemen, E. Ermek, S. Ozturk, Y. Yerli, Z. Z. Ozturk, and H. Urey, "Fabrication of 1d zno nanostructures on mems cantilever for voc sensor application," *Sensors and Actuators B: Chemical*, vol. 202, pp. 357–364, 2014.

[60] J. Xu, M. Bertke, X. Li, H. Mu, H. Zhou, F. Yu, G. Hamdana, A. Schmidt, H. Bremers, and E. Peiner, "Fabrication of zno nanorods and chitosan@ zno nanorods on mems piezoresistive self-actuating silicon microcantilever for humidity sensing," *Sensors and Actuators B: Chemical*, vol. 273, pp. 276–287, 2018.

[61] K. Mistry, V. H. Nguyen, M. Arabi, K. H. Ibrahim, H. Asgarimoghaddam, M. Yavuz, D. Muñoz-Rojas, E. Abdel-Rahman, and K. P. Musselman, "Highly sensitive self-actuated zinc oxide resonant microcantilever humidity sensor," *Nano letters*, vol. 22, no. 8, pp. 3196–3203, 2022.

[62] P. Del'Haye, A. Schliesser, O. Arcizet, T. Wilken, R. Holzwarth, and T. J. Kippenberg, "Optical frequency comb generation from a monolithic microresonator," *Nature*, vol. 450, no. 7173, pp. 1214–1217, 2007.

[63] I. R. Salgado, *Frequency combs on chip for interferometry applications*. Chalmers Tekniska Hogskola (Sweden), 2022.

[64] M. H. De Jong, A. Ganesan, A. Cupertino, S. Gröblacher, and R. A. Norte, "Mechanical overtone frequency combs," *Nature Communications*, vol. 14, no. 1, pp. 1–7, 2023.

[65] T. Fortier and E. Baumann, "20 years of developments in optical frequency comb technology and applications," *Communications Physics*, vol. 2, p. 153, 2019.

[66] W. Xia and X. Chen, "Recent developments in fiber-based optical frequency comb and its applications," *Measurement Science and Technology*, vol. 27, p. 041001, February 2016.

[67] B. A. C. O. N. B. Collaboration*, "Frequency ratio measurements at 18-digit accuracy using an optical clock network," *Nature*, vol. 591, pp. 564–569, 2021.

[68] N. Picqué and T. Hänsch, "Frequency comb spectroscopy," *Nature Photon*, vol. 13, pp. 146–157, 2019.

[69] M.-A. Miri, G. D'Aguanno, and A. Alù, "Optomechanical frequency combs," *New Journal of Physics*, vol. 20, p. 043013, April 2018.

[70] S. Wu, Y. Liu, Q. Liu, S.-P. Wang, Z. Chen, and T. Li, "Hybridized frequency combs in multimode cavity electromechanical system," *Phys. Rev. Lett.*, vol. 128, p. 153901, Apr 2022.

[71] M. H. J. de Jong, M. A. ten Wolde, A. Cupertino, S. Gröblacher, P. G. Steeneken, and R. A. Norte, "Mechanical dissipation by substrate–mode coupling in sin resonators," *Appl. Phys. Lett.*, vol. 121, no. 3, p. 032201, 2022.

[72] T. Rosenband and et al., "Frequency ratio of al+ and hg+ single-ion optical clocks; metrology at the 17th decimal place," *Science*, vol. 319, no. 5871, pp. 1808–1812, 2008.

[73] T. Shi, S. Hussain, C. Ge, G. Liu, M. Wang, and G. Qiao, "Zif-x (8, 67) based nanostructures for gas-sensing applications," *Reviews in Chemical Engineering*, vol. 39, no. 6, pp. 911–939, 2023.

[74] X.-F. Wang, X.-Z. Song, K.-M. Sun, L. Cheng, and W. Ma, "Mofs-derived porous nanomaterials for gas sensing," *Polyhedron*, vol. 152, pp. 155–163, 2018.

[75] H. Yuan, N. Li, W. Fan, H. Cai, and D. Zhao, "Metal-organic framework based gas sensors," *Advanced Science*, vol. 9, no. 6, p. 2104374, 2022.

[76] P. Kumar, K.-H. Kim, P. K. Mehta, L. Ge, and G. Lisak, "Progress and challenges in electrochemical sensing of volatile organic compounds using metal-organic frameworks," *Critical reviews in environmental science and Technology*, vol. 49, no. 21, pp. 2016–2048, 2019.

[77] Y. Kang, F. Yu, L. Zhang, W. Wang, L. Chen, and Y. Li, "Review of zno-based nanomaterials in gas sensors," *Solid State Ionics*, vol. 360, p. 115544, 2021.

[78] Online, "Octosensis micro cantilever arrays," *Available: http://www.micromotive.de/en/Dokumente/DuoOctoDatasheet.pdf*, 2018.

[79] V. H. Nguyen, J. Resende, C. Jiménez, J.-L. Deschanvres, P. Carroy, D. Muñoz, D. Bellet, and D. Muñoz-Rojas, "Deposition of zno based thin films by atmospheric pressure spatial atomic layer deposition for application in solar cells," *Journal of Renewable and Sustainable Energy*, vol. 9, no. 2, 2017.

[80] R. L. Hoye, D. Muñoz-Rojas, K. P. Musselman, Y. Vaynzof, and J. L. MacManus-Driscoll, "Synthesis and modeling of uniform complex metal oxides by close-proximity atmospheric pressure chemical vapor deposition," *ACS Applied Materials & Interfaces*, vol. 7, no. 20, pp. 10684–10694, 2015.

[81] Z. Akimbekov, A. D. Katsenis, G. Nagabhushana, G. Ayoub, M. Arhangelskis, A. J. Morris, T. Friscic, and A. Navrotsky, "Experimental and theoretical evaluation of the stability of true mof polymorphs explains their mechanochemical interconversions," *Journal of the American Chemical Society*, vol. 139, no. 23, pp. 7952–7957, 2017.

[82] B. Mortada, G. Chaplais, H. Nouali, C. Marichal, and J. Patarin, "Phase transformations of metal–organic frameworks maf-6 and zif-71 during intrusion–extrusion experiments," *The Journal of Physical Chemistry C*, vol. 123, no. 7, pp. 4319–4328, 2019.

[83] M. Narducci, E. Figueras, M. J. Lopez, I. Gracia, J. Santander, P. Ivanov, L. Fonseca, and C. Cané, "Sensitivity improvement of a microcantilever based mass sensor," *Microelectronic Engineering*, vol. 86, no. 4-6, pp. 1187–1189, 2009.

[84] Y. Qiao, W. Wei, M. Arabi, W. Xu, and E. M. Abdel-Rahman, "Analysis of response to thermal noise in electrostatic mems bifurcation sensors," *Nonlinear Dynamics*, vol. 107, pp. 33–49, 2022.

[85] Y. Qiao, M. Arabi, W. Xu, H. Zhang, and E. M. Abdel-Rahman, "The impact of thermal-noise on bifurcation mems sensors," *Mechanical Systems and Signal Processing*, vol. 161, p. 107941, 2021.

[86] H. Mouharrar, M. Akbari, K. Musselman, D. Muñoz-Rojas, M. Yavuz, and E. Abdel-Rahman, "Noise-driven mof-coated nems sensors," in *2023 IEEE 22nd International Conference on Micro and Nanotechnology for Power Generation and Energy Conversion Applications (PowerMEMS)*, pp. 187–190, 2023.

[87] Y. Qiao, A. Elhady, M. Arabi, E. M. Abdel-Rahman, and W. Zhang, "Thermal noise-driven resonant sensors," *Microsystems & Nanoengineering*, 2024. Accepted.

[88] Y. Shama, S. Rahmanian, H. Mouharrar, R. Abdelrahman, A. Ahmed, and E. Abdel-Rahman, "Unraveling the nature of sensing in electrostatic mems gas sensors," *microsystems and nanoengineering*, 2023.

[89] L. S. Cao, D. X. Qi, R. W. Peng, M. Wang, and P. Schmelcher, "Phononic frequency combs through nonlinear resonances," *Phys. Rev. Lett.*, vol. 112, p. 075505, Feb 2014.

[90] D. J. Jones *et al.*, "Carrier-envelope phase control of femtosecond mode-locked lasers and direct optical frequency synthesis," *Science*, vol. 288, pp. 635–639, 2000.

[91] K. Minoshima and H. Matsumoto, "High-accuracy measurement of 240-m distance in an optical tunnel by use of a compact femtosecond laser," *Appl. Opt.*, vol. 39, no. 30, pp. 5512–5517, 2000.

[92] M. T. Murphy, T. Udem, R. Holzwarth, A. Sizmann, L. Pasquini, C. Araujo-Hauck, H. Dekker, S. D'Odorico, M. Fischer, T. W. Hänsch, and A. Manescau, "High-precision wavelength calibration of astronomical spectrographs with laser frequency combs," *Monthly Notices of the Royal Astronomical Society*, vol. 380, pp. 839–847, August 2007.

[93] S. Diddams, L. Hollberg, and V. Mbele, "Molecular fingerprinting with the resolved modes of a femtosecond laser frequency comb," *Nature*, vol. 445, pp. 627–630, 2007.

[94] S. T. Cundiff and J. Ye, "Colloquium: Femtosecond optical frequency combs," *Rev. Mod. Phys.*, vol. 75, pp. 325–342, Mar 2003.

[95] A. Rueda, F. Sedlmeir, M. Kumari, *et al.*, "Resonant electro-optic frequency comb," *Nature*, vol. 568, pp. 378–381, 2019.

[96] Z. Qi, G. D'Aguanno, and C. Menyuk, "Nonlinear frequency combs generated by cnoidal waves in microring resonators," *Journal of the Optical Society of America B*, vol. 34, pp. 785–794, 2017.

[97] P. Del'Haye, A. Schliesser, O. Arcizet, *et al.*, "Optical frequency comb generation from a monolithic microresonator," *Nature*, vol. 450, pp. 1214–1217, 2007.

[98] T. J. Kippenberg, R. Holzwarth, and S. A. Diddams, "Microresonator-based optical frequency combs," *Science*, vol. 332, no. 6029, pp. 555–559, 2011.

[99] B. Buscaino, M. Zhang, M. Loncar, and J. M. Kahn, "Design of efficient resonator-enhanced electro-optic frequency comb generators," *J. Lightwave Technol.*, vol. 38, pp. 1400–1413, Mar. 2020.

[100] M. Zhang, B. Buscaino, C. Wang, A. Shams-Ansari, C. Reimer, R. Zhu, J. M. Kahn, and M. Loncar, "Broadband electro-optic frequency comb generation in a lithium niobate microring resonator," *Nature*, vol. 568, no. 7752, pp. 373–377, 2019.

[101] Y. Hu, M. Yu, B. Buscaino, *et al.*, "High-efficiency and broadband on-chip electro-optic frequency comb generators," *Nat. Photon.*, vol. 16, pp. 679–685, 2022.

[102] L. Mercadé, L. L. Martín, A. Griol, D. Navarro-Urrios, and A. Martínez, "Microwave oscillator and frequency comb in a silicon optomechanical cavity with a full phononic bandgap," *Nanophotonics*, vol. 9, no. 11, pp. 3535–3544, 2020.

[103] M. Aspelmeyer, T. J. Kippenberg, and F. Marquardt, "Cavity optomechanics," *Rev. Mod. Phys.*, vol. 86, no. 4, pp. 1391–1452, 2014.

[104] A. Cingöz, D. Yost, T. Allison, *et al.*, "Direct frequency comb spectroscopy in the extreme ultraviolet," *Nature*, vol. 482, pp. 68–71, 2012.

[105] Y. K. Chembo and N. Yu, "Modal expansion approach to optical-frequency-comb generation with monolithic whispering-gallery-mode resonators," *Phys. Rev. A*, vol. 82, p. 033801, Sep 2010.

[106] I. Maksymov, B. H. Nguyen, A. Pototsky, and S. Suslov, "Acoustic, phononic, brillouin light scattering and faraday wave-based frequency combs: Physical foundations and applications," *Sensors*, vol. 22, p. 3921, 2022.

[107] M. Sumetsky, "Optical frequency combs generated mechanically," *Opt. Lett.*, vol. 42, p. 3197, Aug. 2017.

[108] G. Gobat, L. Guillot, A. Frangi, and et al., "Backbone curves, neimark-sacker boundaries and appearance of quasi-periodicity in nonlinear oscillators: application to 1:2 internal resonance and frequency combs in mems," *Meccanica*, vol. 56, p. 1937–1969, 2021.

[109] G. Gobat, V. Zega, P. Fedeli, and et al., "Frequency combs in a mems resonator featuring 1:2 internal resonance: ab initio reduced order modeling and experimental validation," *Nonlinear Dyn*, vol. 111, p. 2991–3017, 2023.

[110] S. Rahmanian, S. Hosseini-Hashemi, and M. Rezaei, "Out-of-plane motion detection in encapsulated electrostatic mems gyroscopes: Principal parametric resonance," *International Journal of Mechanical Sciences*, vol. 190, p. 106022, 2021.

[111] S. Rahmanian, S. Hosseini-Hashemi, and M. SoltanRezaee, "Efficient large amplitude primary resonance in in-extensional nanocapacitors: Nonlinear mean curvature component," *Sci Rep*, vol. 9, p. 20256, 2019.

[112] A. Elhady, M. S. Alghamdi, and E. Abdel-Rahman, "Experimental construction of force- and frequency-response curves of nonlinear resonators," *Chaos: An Interdisciplinary Journal of Nonlinear Science*, vol. 33, p. 063102, 06 2023.

[113] R. Abdelrahman, "Resonant drive techniques for mems: A comparative study," *UWSpace*, 2023.

[114] R. Singh, A. Sarkar, C. Guria, R. J. Nicholl, S. Chakraborty, K. I. Bolotin, and S. Ghosh, "Giant tunable mechanical nonlinearity in graphene–silicon nitride hybrid resonator," *Nano Letters*, vol. 20, no. 6, pp. 4659–4666, 2020.

[115] S. E. H. Yousuf, J. Lee, S. W. Shaw, and P. X.-L. Feng, "Phononic frequency combs in atomically thin nanoelectromechanical resonators via 1: 1 and 2: 1 internal resonances," *Journal of Microelectromechanical Systems*, 2023.

[116] R. Wei *et al.*, "A self-sustained frequency comb oscillator via tapping mode comb-drive resonator integrated with a feedback asic," in *2019 IEEE 32nd International Conference on Micro Electro Mechanical Systems (MEMS)*, pp. 165–168, 2019.

[117] G. Gobat, V. Zega, and P. e. a. Fedeli, "Frequency combs in a mems resonator featuring 1:2 internal resonance: ab initio reduced order modelling and experimental validation," *Nonlinear Dyn*, vol. 111, p. 2991–3017, 2023.

[118] A. Ganesan, C. Do, and A. Seshia, "Phononic frequency comb via intrinsic three-wave mixing," *Phys. Rev. Lett.*, vol. 118, p. 033903, Jan 2017.

[119] K. L. Ekinci, Y. T. Yang, and M. L. Roukes, "Ultimate limits to inertial mass sensing based upon nanoelectromechanical systems," *Journal of Applied Physics*, vol. 95, pp. 2682–2689, 02 2004.